

COMMUNAUTÉ FRANÇAISE DE BELGIQUE
UNIVERSITÉ DE LIÈGE - GEMBLoux AGRO BIO-TECH

DESIGN OF A HYDRAULIC NOZZLE WITH A NARROW DROPLET SIZE DISTRIBUTION

Nicolas DE COCK

A dissertation presented for the degree of Doctor of Philosophy in Agricultural Sciences and
Biological Engineering

Supervisors: Frédéric Lebeau
Benoit Mercatoris
Maria Rosaria Vetrano

2017

COMMUNAUTÉ FRANÇAISE DE BELGIQUE
UNIVERSITÉ DE LIÈGE - GEMBLoux AGRO BIO-TECH

DESIGN OF A HYDRAULIC NOZZLE WITH A NARROW DROPLET SIZE DISTRIBUTION

Nicolas DE COCK

A dissertation presented for the degree of Doctor of Philosophy in Agricultural Sciences and
Biological Engineering

Supervisors: Frédéric Lebeau
Benoit Mercatoris
Maria Rosaria Vetrano

Copyright. Aux termes de la loi belge du 30 juin 1994, sur le droit d'auteur et les droits voisins, seul l'auteur a le droit de reproduire partiellement ou complètement cet ouvrage de quelque façon et forme que ce soit ou d'en autoriser la reproduction partielle ou complète de quelque manière et sous quelque forme que ce soit. Toute photocopie ou reproduction sous autre forme est donc faite en violation de la dite loi et de des modifications ultérieures.

Acknowledgements

First of all, I would like to thank the F.R.N.S for the funding of my PhD with a FRIA grant.

I would like to thank Frédéric for his strong support during these years. You helped me to improve and challenge myself. Your ability to always see the bright side of things and your passion for research brought me the motivation to realize this PhD. I also thank the members of my thesis Jury for the comments and advice they provide to me during these four years: Denis Terwagne, Benoit Mercatoris, Maria Rosaria Vetrano, Pieter Verboven, Stéphane Dorbolo and Philippe Lejeune.

I have a thought for my PhD colleague and friends from VKI: Nuno, Giuseppe, Sara, Julien, Roberto, Aude,... Sharing this experience together helps me to stay motivated during these years !

Merci à Mathieu de m'avoir fait grandement progresser au ping pong et surtout pour ces super années à partager le bureau. Un remerciement particulier à Rudy Schartz pour son aide précieuse et surtout sa patience. Une pensée également pour mes autres collègues, Sofiene, Benjamin, Benoît, Vincent, Jean-François, Françoise, Arnaud, Alwin, Éric.

Je remercie également ma famille sans qui je n'en serais pas arrivé là. Merci à mes parents et beaux parents pour leur soutien et encouragement pendant ces années ! Merci à mes frères et sœurs.

Une pensée aussi pour mes amis qui ne pensaient pas qu'on pouvait vraiment faire un doctorat sur les gouttes... Pourtant les 4 années sont passées bien vite ! Merci pour votre support, Tanguy, Kacem, William, Hélène, Polé, Tony, Julien, ...

Il faut garder le meilleur pour la fin, merci à toi Anne-Sophie pour ton amour et ton support durant ces années. Une pensée particulière à ta patience pendant la période de rédaction !

Summary

Nowadays, pesticides use is necessary to satisfy the growing demand for agricultural products. During pesticide spray application, the agricultural mixture containing the active ingredient is fragmented to a cloud of droplets of various sizes and speeds. The droplet size distribution within the spray affects the efficiency of the treatment. According to the target, a specific droplet size should be used. However, hydraulic nozzles usually used in field application produce sprays with a wide droplet size distribution containing an important proportion of small or too large droplets. This results in non-optimal application and therefore losses of product into the environment. This statement conducted the research as early as in the 60's to create the rotary atomizer. This device is able to produce narrow droplet size distribution using Plateau-Rayleigh break up mechanism. The characteristics of the produced spray by the rotary atomizer can be tuned by adjusting the rotational speed and the volumetric flow rate. Although offering agronomic and environmental qualities this has not met success for the application of plant protection products in field crops because of their cost, size and complexity. The aim of the thesis was the design of a hydraulic nozzle with the rotary atomizer qualities and without the constraints of rotating parts. Unlike the rotary atomizer which has two control variables, the developed hydraulic nozzle will have a narrower operating range, thus a specific geometry has to be design for each kind of treatment. The new hydraulic nozzle design is composed by an inlet pipe ending perpendicularly on a plate. There is a thin opening at the junction between the pipe and the plate. The edge of the plate is constituted of channels formed by structures. These channels aim to divide the liquid sheet in multiple jets. The breakup of these jets into droplets generate a narrow droplet size distribution. The thesis can be seen as a road-map providing design tools at each step starting from the determination of an optimal droplet size according to the kind of treatment and ending with a nozzle geometry.

The optimization of both spray deposition and retention leads to a dilemma: should small droplets be used to increase retention or large droplets be preferred to avoid drift? An ideal droplet should have a short time of flight to minimize its distance traveled while impacting the target with a moderate kinetic energy. The prediction of the optimal droplet size according to the treatment was done using integrated modeling approach of the spray

transport and retention by the plant. The main parameters of spray deposition and retention models were systematically varied and the effects on drift potential and droplet impaction outcomes are discussed. The results of the numerical simulations showed that droplets with diameter ranging between $200\ \mu\text{m}$ and $250\ \mu\text{m}$ offer high control of deposition by combining a low drift potential and a moderate kinetic energy at top of the canopy. A fourfold reduction of the volume drifting further than 2 m from the nozzle was observed for a spray with a volume median diameter of $225\ \mu\text{m}$ when the relative span factor of the droplet spectrum was reduced from 1.0 to 0.6. In the latter scenario, an increase from 63 to 67% of the volumetric proportion of droplets adhering to the wheat leaf was observed. Therefore, strategies for controlling the droplet size distribution may offer promising solutions for reducing adverse impact of spray applications on environment.

The experimental characterization of agricultural sprays is usually performed using optical techniques. At present, the relevance of different characterization techniques remains controversial since discrepancies may be significant between measurements performed in different laboratories. A digital image acquisition technique and analysis algorithm has been developed for droplet size and velocimetry measurements as an alternative to well-established techniques such as the Phase Doppler Particle Analyzer (PDPA) or laser diffraction spectrometry (LDS). The algorithm requires double exposed shadow images acquired in a back-lighted arrangement with a Particle Image Velocimetry (PIV) camera and a pulsed light emitting diode (LED). Spatial illumination heterogeneities are corrected by subtracting from each image a mean background acquired on several images without any particle. The algorithm accuracy is ensured by the rejection of out-of-focus particles using a focus parameter depending on gradient intensity at the particle edges. Thresholds for focus particle selection were determined by studying the evolution of the focus parameter and the error on particle size measurements from images containing droplets with uniform size at various distance of the object plane. Selected droplets were identified on both pairs of images to determine their size and velocity. Droplet size distributions were corrected to account for the uneven sampling probability caused by the volumetric method. Droplet size distributions of a set of reference nozzle/pressure combinations defined in the ISO/DIS 25358 were measured. The image technique was able to distinguish each of the reference sprays well. Comparison with PDPA measurements showed that the imaging technique tends to measure an equivalent Dv_{50} , a lower Dv_{10} and a higher Dv_{90} leading therefore to a higher relative span factor. Velocity measurements showed good agreement between both techniques except for one nozzle/pressure combination.

The analytical description of the flow on the nozzle plate is based on an extension of the analytical solution of the radial spread of a liquid jet over a horizontal surface. When the

gap, H , between the jet nozzle and the plate is reduced the discharging area may be smaller than the inlet area leading to an increase of the main flow velocity downstream of the thin cylindrical opening. This increase of velocity, defined here as $\frac{1}{\alpha}$, can be related to the relative gap of the nozzle $\frac{H}{R}$ with R the nozzle pipe radius. The development of this analytical model is based on Computational Fluid Dynamics (CFD) simulations using a Volume of Fluid model (VoF). Numerical computations were realized with for $\frac{H}{R}$ ranging from 0.2 to 3 and with flow rates Q of 3 and 6 $\ell \text{ min}^{-1}$. The results of these computations allowed to express α in respect of $\frac{H}{R}$. Taking into account the flow acceleration allowed to extend the set of equation from the jet impacting flow to the thin cylindrical opening flow. The liquid layer thickness and the surface velocity differ with a maximum error of 4 % between the flow predicted by the model and computations. Main discrepancies appear in the region close to the inlet exit where the analytical model assumption of a constant velocity outside the boundary layer is not valid. However, further downstream the model and the computations are in good agreement. Other CFD simulations have been realized to investigate the sensitivity of a splash plate nozzle flow to the inlet geometry and the inlet flow rate. The sensitivity study of the nozzle geometry and the inlet flow rate on the downstream flow allowed us to see a strong effect of both parameters. The flow rate increase lead to a more homogeneous flow for most of the cases. The inlet shape affects significantly the downstream flow. The 140° circular segment inlet seems suitable for our objective of generating a homogeneous flow on the nozzle plate.

Finally, using the latter model, a theoretical nozzle design has been established in order to produce a spray with droplets with diameter of $225 \mu\text{m}$ (§ 6). The prototyping of this design couldn't be achieved because of its small dimension. However, the design methodology has been validated on a upscale nozzle model. The spray generated by the upscale nozzle has been characterized using high-speed imaging showing a narrow droplet size distribution.

Résumé

De nos jours, les pesticides sont largement utilisés pour satisfaire la demande croissante en produits agricoles. Lors de l'application de produits phytosanitaires, la bouillie agricole contenant la matière active est fragmentée en un nuage de gouttelettes de tailles et vitesses variées. La distribution granulométrique au sein de ce nuage ou pulvérisation agricole affecte significativement l'efficacité du traitement. Selon la cible traitée, une taille de gouttelette spécifique doit être privilégiée. L'application en champs est généralement réalisée en utilisant des buses à travers lequel la bouillie est éjectée sous pression. Ce type de buse appelé buse hydraulique génère des pulvérisation agricoles avec une large distribution de taille de gouttelettes. Par conséquent, cela entraîne une application non optimale et donc des pertes de produit dans l'environnement. Cette observation au développement de nouveau dispositif tel que l'atomiseur rotatif. Cet actionneur est capable de produire une distribution de taille de gouttelettes étroite en utilisant le mécanisme de rupture de Plateau-Rayleigh. Les caractéristiques de la pulvérisation produite par l'atomiseur rotatif peuvent être réglées en ajustant la vitesse de rotation et le débit volumétrique. Bien qu'offrant des qualités agronomiques et environnementales indéniables, ce dispositif n'a pas été un succès pour l'application de produits phytosanitaires en grandes cultures en raison de son coût, de sa taille et de sa complexité. Le but de cette thèse était la conception d'une buse hydraulique possédant les qualités de l'atomiseur rotatif et sans les contraintes des pièces en rotation. Contrairement à l'atomiseur rotatif qui a deux variables de contrôle (vitesse de rotation et débit), la nouvelle buse hydraulique développée n'aura une plage de fonctionnement plus étroite, une géométrie spécifique doit être conçue pour chaque type de traitement. Cette nouvelle buse hydraulique est composée d'une tuyère se terminant perpendiculairement sur une plaque. À la jonction entre le tuyau et la plaque, il y a une mince ouverture. Le bord de la plaque est constitué de canaux. Ces canaux visent à diviser la nappe liquide en plusieurs jets. La rupture de ces jets en gouttelettes génère une distribution de taille de gouttelettes étroite. La thèse se présente comme une feuille de route fournissant des outils de conception à chaque étape à débutant par la détermination d'une taille de gouttelette optimale en fonction du type de traitement et se terminant par une géométrie de buse.

L'optimisation du dépôt et de la rétention de la pulvérisation agricole conduit à un dilemme: faut-il utiliser de petites gouttelettes pour augmenter la rétention ou préférer de grosses gouttelettes pour éviter la dérive? Une gouttelette idéale devrait avoir une courte durée de vol pour minimiser sa distance parcourue tout en affectant la cible avec une énergie cinétique modérée. La prédiction de la taille optimale des gouttelettes en fonction du traitement a été faite en utilisant une approche de modélisation intégrée du transport par pulvérisation et de la rétention par la plante. Les principaux paramètres des modèles de dépôt et de rétention de pulvérisation ont été systématiquement modifiés et les effets sur le potentiel de dérive et les résultats de la rétention des gouttelettes ont été discutés. Les résultats des simulations numériques ont montré que les gouttelettes de diamètre compris entre $200\ \mu\text{m}$ et $250\ \mu\text{m}$ offrent un contrôle élevé des dépôts en combinant un faible potentiel de dérive et une énergie cinétique modérée lorsqu'elles atteignent la canopée. On a observé une division par quatre du volume de la dérive à plus de 2 m de la buse pour une pulvérisation ayant un diamètre médian en volume de $225\ \mu\text{m}$ lorsque le facteur relatif d'étendue du spectre de gouttelettes était réduit de 1,0 à 0,6. Dans ce dernier cas, une augmentation de 63 à 67% de la proportion volumétrique de gouttelettes adhérant à la feuille de blé a été observée. Par conséquent, les stratégies de contrôle de la distribution de la taille des gouttelettes peuvent offrir des solutions prometteuses pour réduire l'impact négatif des applications de produits phytosanitaires sur l'environnement.

La caractérisation expérimentale des pulvérisations agricoles est généralement réalisée à l'aide de techniques optiques. À l'heure actuelle, la pertinence des différentes techniques de caractérisation reste controversée puisque les écarts peuvent être importants entre les mesures effectuées dans différents laboratoires. Une technique d'acquisition d'images numériques et un algorithme d'analyse ont été développés pour mesurer la taille et la vitesse des gouttelettes comme alternative aux techniques bien établies tel que l'analyseur de particules à phase Doppler (PDPA) ou la spectrométrie de diffraction laser (LDS). Le suivi des gouttes est réalisé sur base de paire d'images acquises dans un court laps de temps. La pulvérisation étant rétro-éclairé, les gouttes apparaissent sous forme d'ombre au niveau de l'image. Ces images sont ensuite traitées et puis analysées. Dans un premier temps, les hétérogénéités d'illumination spatiale sont corrigées en soustrayant de chaque image un arrière fond moyen acquis sur plusieurs images sans aucune particule. La précision de l'algorithme est assurée par le rejet des particules défocalisées en utilisant un paramètre de focalisation dépendant de l'intensité du gradient aux bords des particules. Les seuils de sélection des particules nettes ont été déterminés en étudiant l'évolution du paramètre de focalisation et l'erreur sur les mesures de taille de particules à partir d'images contenant des gouttelettes de taille uniforme à différentes distances du plan focal. Les gouttelettes sélectionnées ont été identifiées sur

les deux paires d'images pour déterminer leur taille et leur vitesse. Les distributions de la taille des gouttelettes ont été corrigées pour tenir compte de la probabilité d'échantillonnage inégale causée par la méthode volumétrique. Les distributions de la taille des gouttelettes d'un ensemble de combinaisons buse / pression de référence définies dans l'ISO / DIS 25358 ont été mesurées. La technique de l'image a permis de bien distinguer chacune des pulvérisations de référence. La comparaison avec les mesures PDPA a montré que la technique d'imagerie tend à mesurer un Dv_{50} équivalent, un Dv_{10} inférieur et un Dv_{90} supérieur conduisant ainsi à un facteur de portée relative plus élevé. Les mesures de vitesse ont montré un bon accord entre les deux techniques, à l'exception d'une combinaison buse / pression.

La description analytique de l'écoulement sur la plaque de la buse est basée sur une extension de la solution analytique de la dispersion radiale d'un jet liquide sur une surface horizontale. Lorsque l'ouverture H à la jonction entre la plaque et la tuyère est réduite, la zone de décharge peut être plus petite que la zone d'entrée, ce qui conduit à une augmentation de la vitesse de l'écoulement en aval de l'ouverture. Cette augmentation de la vitesse, définie ici comme $\frac{1}{\alpha}$, peut être liée à l'écart relatif de la buse $\frac{H}{R}$ avec R le rayon du tuyau de buse. Le développement de ce modèle analytique a été basé sur des simulations de mécanique des fluides numérique (MFN) utilisant un modèle de volume de fluide (VoF). Les calculs numériques ont été réalisés pour $\frac{H}{R}$ allant de 0.2 à 3 et pour des débits Q de 3 et 6 $\ell \text{ min}^{-1}$. Les résultats de ces calculs ont permis d'exprimer α par rapport à $\frac{H}{R}$. L'épaisseur de la couche liquide et de la vitesse de surface diffèrent avec une erreur maximale de 4 % entre le modèle et les calculs numériques. Les principales divergences apparaissent dans la région proche de la sortie d'entrée où l'hypothèse du modèle analytique d'une vitesse constante en dehors de la couche limite n'est pas valide. Cependant, plus en aval, le modèle et les calculs fournissent des résultats similaires. D'autres simulations MFN ont été réalisées pour étudier la sensibilité d'un écoulement au niveau de la plaque à la géométrie de la tuyère et au débit d'entrée. L'étude de sensibilité de la géométrie de la buse et du débit d'entrée sur l'écoulement aval a permis de constater un fort effet de ces deux paramètres. L'augmentation du débit conduit à un écoulement plus homogène pour la plupart des cas. La forme de l'entrée affecte significativement l'écoulement en aval. L'entrée du segment circulaire de 140° semble convenir à notre objectif de générer un écoulement homogène sur la plaque de buse.

Finalement, en utilisant ce dernier modèle, un design de buse théorique a été établie afin de produire une pulvérisation avec des gouttelettes de diamètre 225 μm . Le prototypage de cette géométrie n'a pas pu être réalisé en raison de sa petite dimension. Cependant, la méthodologie de conception a été validée sur un modèle de buse haut de gamme. La

pulvérisation générée par la buse haut de gamme a été caractérisée en utilisant une imagerie à haute vitesse montrant une distribution de taille de gouttelettes étroite.

Table of contents

List of figures	xxi
List of tables	xxv
1 General introduction	1
1.1 Crop protection	1
1.2 Droplet size distribution of agricultural sprays	4
1.3 Rayleigh-Plateau breakup	5
1.4 Thesis goals	7
1.5 Thesis organization	8
2 Investigation on optimal spray properties using modeling approach	9
2.1 Preamble	9
2.2 Introduction	9
2.3 Materials and methods	12
2.3.1 Droplet deposition model	12
2.3.2 Droplet retention model	15
2.3.3 Numerical procedure	16
2.3.4 Parameter sensitivity study	17
2.4 Results	19
2.4.1 Sensitivity analysis of a population of monodisperse droplets	19
2.4.2 Polydisperse sprays	26
2.5 Discussion	26
2.6 Conclusion	29
3 Characterization of droplet size and speed using high-speed imaging	33
3.1 Preamble	33
3.2 Introduction	34
3.3 Materials and methods	36

3.3.1	Experimental set-up	36
3.3.2	Image processing	37
3.3.3	Particle tracking velocimetry (PTV)	40
3.3.4	Droplet size distribution	41
3.3.5	Image processing implementation	42
3.3.6	Reference nozzles-pressure combinations	42
3.3.7	Measuring protocol	43
3.4	Results and discussion	45
3.4.1	Droplet measurement	45
3.4.2	Effect of the correcting factor	46
3.4.3	Droplet size distribution	46
3.4.4	Droplet velocity distribution	50
3.5	Conclusion	52
3.6	Aknowledgments	53
4	Numerical modelling of the effect of a splash plate nozzle inlet shape	55
4.1	Preamble	55
4.2	Introduction	56
4.3	Materials and methods	57
4.3.1	Numerical model	57
4.3.2	Validation case	58
4.3.3	Splash plate nozzle	59
4.4	Results	61
4.4.1	Validation case	61
4.4.2	Splash plate nozzle	62
4.5	Conclusion	62
5	Dynamics of a thin radial liquid flow	67
5.1	Preamble	67
5.2	Introduction	67
5.3	Theoretical developments	70
5.3.1	Flow created by a round liquid jet impacting on a horizontal plate	70
5.3.2	Radial flow of a thin liquid film	72
5.4	Numerical modelling	74
5.4.1	Computational domain	74
5.4.2	Computational parameters	74
5.4.3	Boundary conditions	75

5.4.4	Numerical method	75
5.4.5	Post processing	75
5.4.6	Model quality	76
5.5	Results and discussion	76
5.6	Conclusion	78
6	Nozzle with narrow droplet size distribution	81
6.1	Introduction	81
6.2	Nozzle geometry	81
6.3	Design methodology	82
6.4	Theoretical design	84
6.5	Proof of concept	84
6.6	Conclusion	85
7	Conclusions and perspectives	89
	References	91

List of figures

1.1	Sketch of the application of a systemic herbicide, from the droplet formation to the plant vascular system.	3
1.2	Possible impact outcomes of a droplet hitting a superhydrophobic surface, depending on leaf hydrophobicity and droplet impact velocity (adapted from Boukhalfa et al. (2014)).	3
1.3	Illustration of the two breakup modes occurring at the exit of a rotary atomizer (a) and a hydraulic nozzle (b).	5
1.4	Breakup regimes of a cylindrical water jet in still air at atmospheric pressure.	6
1.5	Illustration of the nozzle with the three main regions: the nozzle pipe (1), the disk (2), the disk structures (3).	7
2.1	Flow chart of the droplet transport model.	13
2.2	Initial configuration of the deposition model.	16
2.3	Cumulative droplet size distribution of the virtual sprays for the six Dv_{50} and the two RSF	18
2.4	Median vertical and horizontal velocity with respect to the droplet vertical location.	19
2.5	Droplet trajectories under a wind of 2 m s^{-1} according to their sizes.	20
2.6	Effect of the release height, wind speed, release velocity and release angle on the average of the log-normal fit arithmetic mean $E.x$	21
2.7	Effect of the release height, wind speed, release velocity and release angle on the distance above which 95 % of the droplets have reach the top canopy level X_{95}	23
2.8	Droplet velocity and angle at top canopy level	24
2.9	Evolution of the relative volume evaporate in respect to the relative humidity and the wind speed.	25
2.10	Volume of airborne spray in respect with distance.	27
2.11	Droplet impact outcome predictions at top canopy level.	28

3.1	Shadowgraphy set-up used for the image acquisitions.	37
3.2	Main steps of the droplet sizing algorithm illustrated with the example of the selection of droplets starting from a raw image.	38
3.3	Oblique shoot of 111, 351 and 516 μm droplet streams (a). Focus parameter (b) and relative error on the diameter measurement (c) in respect to the distance from the focal plane.	40
3.4	Depth of field for the different droplet diameters according to the focus parameter. The dashed lines correspond to linear regressions.	41
3.5	Droplet tracking principle using a search area based on the size conservation of the droplet and a priori knowledge of the flow direction in order to retrieve the same droplet on two successive frames.	42
3.6	Illustration of the corrected field of view (FOV_{cor}) in dashed line which is defined as the area on the first image wherein the droplet center must be located in order to be measured. To be measured a droplet cannot be cropped by the image edge and has to fully appear on the second image.	43
3.7	Scanning pattern used for the characterization of the sprays.	44
3.8	Spatial distribution of the rejected and the accepted droplets on the field of view. The droplets from all the imaging measurements have been used to build this spatial distribution.	47
3.9	Relative number of droplet and relative cumulative volume in respect to the droplet diameter for PDPA and imaging techniques.	47
3.10	Relative value of the different correcting factors in respect to the droplet diameter for the F/M case.	48
3.11	Cumulative volumetric droplet size distribution for the 6 spray class boundaries	49
3.12	Dv_{10} , Dv_{50} and Dv_{90} [μm] for the 6 reference sprays. Imaging technique and PDPA are represent by full lines with circles and the dashed lines with squares respectively.	50
3.13	Average velocity measured per diameter class of 50 μm with both techniques. The error bars indicate the standard error on the mean.	51
3.14	Cumulative volumetric droplet velocity distribution for the 6 different nozzle-pressure combinations. Imaging technique and PDPA are represented by the circle with full lines and the square with the dashed lines respectively. . . .	52
4.1	Example of C field, the blue shape indicates the real liquid contour.	57
4.2	Illustration of the flow created by a round jet impacting a flat surface	58
4.3	Numerical domain of the test case with the associated boundary conditions.	60
4.4	Numerical domain of the geometry 1 with the associated boundary conditions.	61

4.5	Flow on the plate after 0, 2 and 4 ms respectively for the 140° pipe with an inlet flow of 2 ℓ min ⁻¹	61
4.6	Analytical and numerical solutions of the water thickness h and the interface velocity U in respect with the radial distance to the jet center r	62
4.7	Spatial distribution over the plate of the normalized flow rate.	63
4.8	Error on the estimation of the flow rate in respect with cell number.	65
5.1	Half radial cut of the radial flow created by a impact of a round jet on a horizontal plate and thin cylindrical opening.	68
5.2	Computational domain used to simulate the flow generated by a thin cylindrical opening with the associated boundary conditions.	73
5.3	Example of mesh for a nozzle with a radius of 1 mm and a height of 1 mm. The dimensions are given in meters.	74
5.4	Comparison of the value of α retrieved from the post processing or found in the literature in respect with the relative gap.	77
5.5	Comparison between between the numerical data from all the cases and the model prediction for the surface velocity and liquid thickness in respect with the radial distance.	78
5.6	NRMSD on the interface velocity (top) and the liquid sheet thickness (bottom) predictions in respect with the relative opening ratio.	79
6.1	Summary of the nozzle design procedure.	82
6.2	Geometry of the design nozzle	83
6.3	Average liquid sheet velocity in respect to the radial distance from the nozzle center for three nozzle configurations.	84
6.4	Iso contour of the average liquid sheet velocity. a) constant $R = 1$ mm was considered. b) constant $r = 15.25$ mm was considered.	85
6.5	Dimensions of the upscale nozzle model.	86
6.6	High-speed imaging measurements at the exit of the nozzle	86
6.7	Cumulative droplet size distribution measured at 50 mm downstream of the disk edge.	87

List of tables

2.2	Simulation constants. The air and water temperature properties were taken both for 15 °C. Subscript <i>g</i> and <i>l</i> refer to gaseous and liquid phases respectively.	17
2.3	Range of variation of the simulation parameters. The standard values are highlighted in bold.	18
2.4	Airborne spray reduction [%] induced by a <i>RSF</i> reduction from 1.0 to 0.6. The airborne spray reduction is given for each Dv_{50} at 5 distances from the release point.	27
3.2	Combination of nozzle and pressure defining the different spray class boundaries with the respective nominal flow rate.	43
3.3	Number of droplets measured and rejected with both technique for each nozzle-pressure combinations.	45
3.4	Average, standard deviation and coefficient of variation of the difference between following spray class boundary.	49
3.5	Relative span factor measured for each spray class boundaries for PDPA and imaging technique.	50
4.2	Mesh characteristics for the three cases studied.	59
4.3	Summary of the numerical simulations parameters.	60
6.1	Reduced parameters of the droplet size distribution measured at 50 mm downstream of the disk edge for the three flow rates.	85

Chapter 1

General introduction

1.1 Crop protection

Modern agriculture has to ensure high yield in order to satisfy the growing demand for agricultural goods. One cornerstone of modern agriculture is the protection of crops against plant diseases, weeds and animals (insects, mites, nematodes, birds, snails, etc.) which are called pest. Oerke (2006) estimates that crop protection prevents a loss of 45% of the world food production. The control of pests can be realized using physical (mechanical weeding, etc.), biological (cultivar choice, crop rotation, etc.) and chemical treatment (pesticides). The use of pesticides is an integral part of modern agriculture and contributes to the productivity and the quality of the cultivated crop. During the pesticide application, the agricultural mixture containing the active ingredient flows through a nozzle, generating a cloud of droplets of various sizes and speeds. The droplets can be airborne outside the targeted area by airflow or penetrate in the soil. The downwind movement of airborne spray outside the targeted area is defined as spray drift (Stephenson et al., 2006). Pesticide exposure caused by drift leads to potential pesticides contamination in air, water and soil (Reichenberger et al., 2007). The public is increasingly concerned about the hazards of being exposed to pesticide as bystanders or residents. European legal framework (2009/128/CE) becomes increasingly constraining about available products, application techniques and environmental safety. To meet these requirements, the spray application technique should be chosen for maximizing the dose delivered at action site while limiting environmental contamination and operator exposure.

The application of a pesticide can be divided into four successive stages: deposition, retention, uptake and translocation (Zabkiewicz, 2007) as illustrated on Figure 1.1. Deposition corresponds to droplet transport from the nozzle to the target (weeds, insects, plant pathogens, etc.) or the amount of pesticide directed within the target area. Deposition efficiency is

then defined as the ratio between the volume of droplet that reaches the target and the total volume sprayed. Deposition is optimized when the probability of a droplet to collide with the target is maximal considering the whole droplet size and velocity distributions. Retention is the part of the deposited volume effectively retained by the plant. Its efficiency is determined by the outcome of each spray droplet at impaction on the target (Massinon et al., 2015). Droplet behaviour at impaction is mainly governed by the droplet kinetic energy, the liquid surface tension and the surface wettability (Josserand and Thoroddsen, 2016; Yarin, 2006). Flying insect control, such as mosquitoes, requires small droplets ($\leq 50 \mu m$) for maximizing retention but are, however, airborne for a longer time than large droplets. For systemic pesticides, the product has to be transported through the plant vascular system. The uptake is the amount of pesticide taken up into the plant foliage. This process is affected by environmental factors (rain, wind, relative humidity) as well as the leaf surface properties. Specific spray adjuvants are generally used in the formulation to overcome the effect of leaf waxes and the cuticle. Finally, the translocation is the transport of the active ingredient from the absorption site, e.g. the leaf, to the plant vascular system. The efficiency of the whole application process results from the efficiency of each step. Regardless environmental conditions, the retention and the deposition efficiencies are mostly determined by the droplets characteristics (size, velocity) whilst the uptake and translocation stages are affected by the chemical interactions between the agricultural mixture and the plant cells. The present work focuses on the retention and deposition stages.

The environmental contamination by spray drift has been extensively studied during the past decades. It appears clearly that the main parameters governing the drift are droplet size, release height and meteorological conditions (Baetens et al., 2007; Hobson et al., 1993; Nuyttens et al., 2007b). Longer a droplet remains airborne, higher it may be carried away by the wind (de Ruiter et al., 2003). The amount of spray drift is usually related to the percentage of fine spray droplets within the spray. The smaller a droplet, the longer it remains airborne and the higher the possibility for it to be carried away by crosswind from the target area. Droplets with diameter $\leq 100 \mu m$ contribute significantly to drift losses (Hobson et al., 1993; Holterman, 2003). Al Heidary et al. (2014) showed that spray drift decreases with the droplet kinetic energy following a power law.

The amount of spray remaining on a plant after impact is determined by the sum of each droplet impact outcomes (adhesion, bounce or shatter). Massinon and Lebeau (2012) studied retention on a synthetic superhydrophobic surface of droplets from a moving agricultural spray. Their experiments showed that the droplet Weber number can be used as a threshold between the droplet outcomes. Slow and small droplets were adhering on the surface. Then droplets with intermediate kinetic energy were bouncing. Finally, fast and large droplets

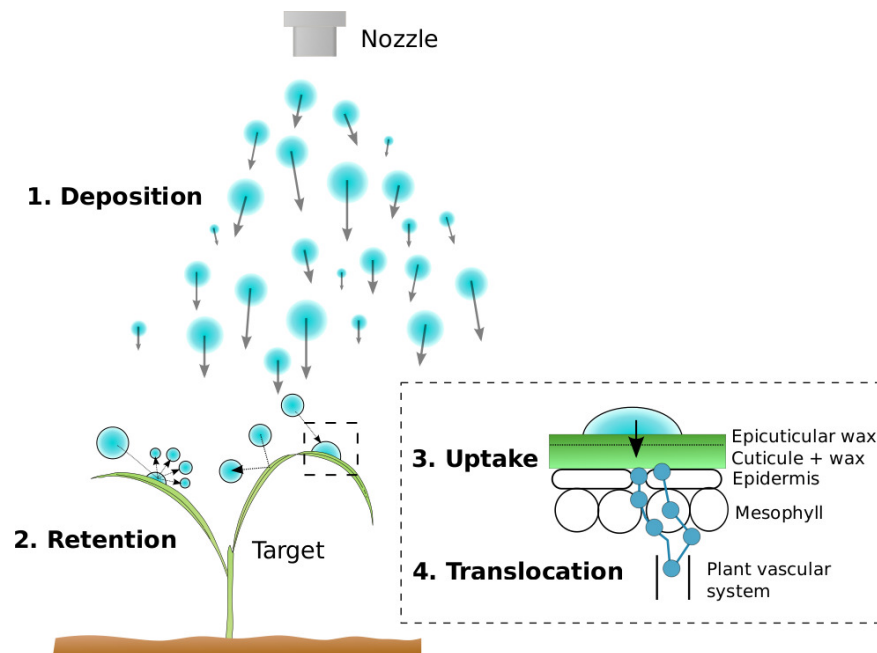


Fig. 1.1 Sketch of the application of a systemic herbicide, from the droplet formation to the plant vascular system.

were shattering. The figure 1.2 summarizes the transition between each droplet outcomes in a phase diagram.

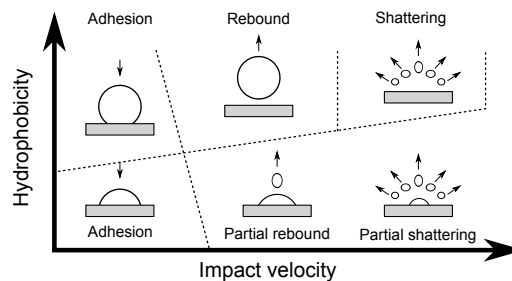


Fig. 1.2 Possible impact outcomes of a droplet hitting a superhydrophobic surface, depending on leaf hydrophobicity and droplet impact velocity (adapted from Boukhalfa et al. (2014)).

1.2 Droplet size distribution of agricultural sprays

An agricultural spray is often characterized by its volume mean droplet diameter (*VMD* or Dv_{50}). The *VMD* is the midpoint droplet size, where half of the volume of spray is constituted of smaller droplets, and half of the volume is constituted of larger droplets. American Society of Agricultural Engineers classified agricultural spray according to the *VMD* as: very fine ($\leq 100 \mu m$), fine (100-175 μm), medium (175-250 μm), coarse (250-375 μm), very coarse (375-450 μm), or extremely coarse ($\geq 450 \mu m$). Additional statistical description of the droplet size distribution is provided by the relative span factor (*RSF*) defined as $RSF = \frac{Dv_{90} - Dv_{10}}{Dv_{50}}$ with Dv_{10} , Dv_{50} and Dv_{90} corresponding to the maximum droplet diameter below which 10 %, 50 % and 90 % of the volume of the sample exists, respectively. Agricultural sprays produced by hydraulic nozzles have a *RSF* around 1. Then, a spray with a Dv_{50} of 200 μm has a Dv_{10} of 100 μm and a Dv_{90} of 300 μm .

One common approach to reduce drift is to shift the droplet spectrum towards coarser droplets using low-drift nozzle or by adding spray additives. However, coarse droplets present a relatively low degree of surface coverage and may bounce or shatter on the target (Hilz and Vermeer, 2013; Massinon et al., 2017). An other solution is to narrow the droplet size distribution towards an intermediate range of droplet size. This idea stimulated the development of alternative devices for spray generation using centrifugal forces such as the rotary atomizers (Bals, 1970). Liquid is fed near the center of a rotating surface so that centrifugal force spreads the liquid to the edge of the disk. At low flow rates, large single droplets are emitted from the disk. As the flow rate increases ligaments are formed which in turn break into smaller droplets. The increase of the disk rotational speed decreases the size of the droplets. These atomizers deliver a spray with a significantly narrower drop size distribution than the hydraulic nozzles usually used in field treatment (Hewitt, 2005; Qi et al., 2008). Measurements of the droplet size distribution of rotary atomizers shows a *RSF* around 0.6. Field experiments showed that rotary atomizers could substantially reduce the potential for exposure to fine droplets in comparison with conventional hydraulic nozzles, 50 m downwind of the spray line (Gilbert and Bell, 1988). Despite the quality of the produced sprays, the rotary atomizers are not hardly used for field spray application because of their bulkiness. However, they remain an interesting study case as a way to produce sprays with narrow drop size distribution. The contrast in term of droplet size distribution between the hydraulic nozzles and the rotary atomizers derives from the different breakup modes occurring with the two atomizers types. Rotary atomizers produce round liquid jets of uniform sizes at the exit of the rotating part, then these jets break in droplets by the Rayleigh-Plateau mode (Fig. 1.3 a). Whilst, the hydraulic nozzles produce a liquid sheet that breakup in ligaments which, in turn, breakup in to droplets of various sizes (Fig. 1.3 b).

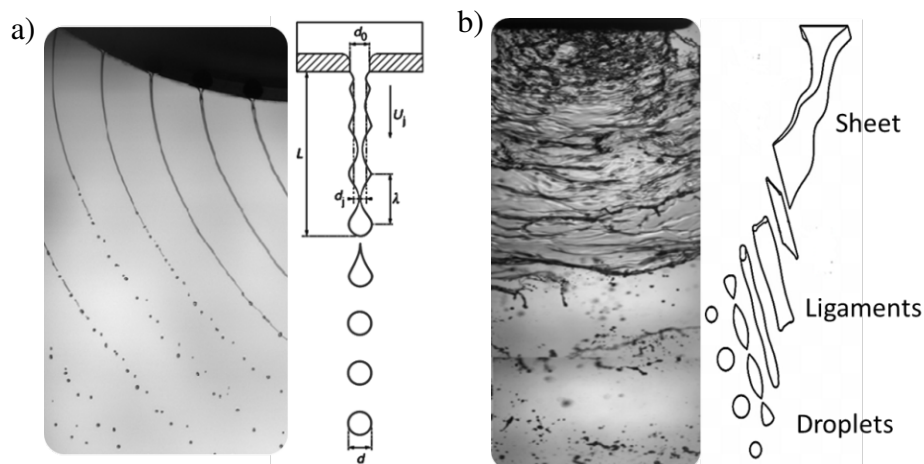


Fig. 1.3 Illustration of the two breakup modes occurring at the exit of a rotary atomizer (a) and a hydraulic nozzle (b).

1.3 Rayleigh-Plateau breakup

When a liquid jet flows in the air, deformations appear on the gas-liquid interface. These deformations grow in space and time leading to the formation of droplets. The figure 1.4 shows the 5 possible breakup regimes of a liquid round jet exiting a nozzle for an increasing jet velocity. At low jet velocity, the liquid gathers at the tip of the nozzle until a droplet drips, it's the dripping regime. In the Rayleigh-Plateau regime, a liquid column is formed at the exit of the nozzle. In this regime, axi-symmetrical perturbations are amplified by capillarity. Theoretical developments realized by Rayleigh (1878) showed that the growth of the most unstable perturbation breaks the jet in droplets with a diameter in average equal to 1.89 times the jet diameter. When the velocity of the jet increases, the shear forces between the liquid and the surrounding gas becomes significant, it's the 1st wind induced regime. The jet breakup is controlled by the growth of an axi-symmetric capillary perturbation and an axi-asymmetric aerodynamic perturbation. The droplet size distribution is wider than in the Rayleigh-Plateau due to the presence of satellite droplets. In the 2nd air induced mode, the aerodynamic interactions are dominating. Near the nozzle, some droplets can be peeled off at the air-gas interface. Further, the jet is breaking in ligaments which in turn break in to droplets of various sizes. This regime is rather chaotic and produces droplet of various sizes. Finally in the atomization regime, the droplets are formed directly at the nozzle exit. The droplets diameter are much less than the jet diameter.

The transitions between each regime can be described using liquid and gaseous Weber numbers which express the ratio of the inertia forces on the surface tension forces

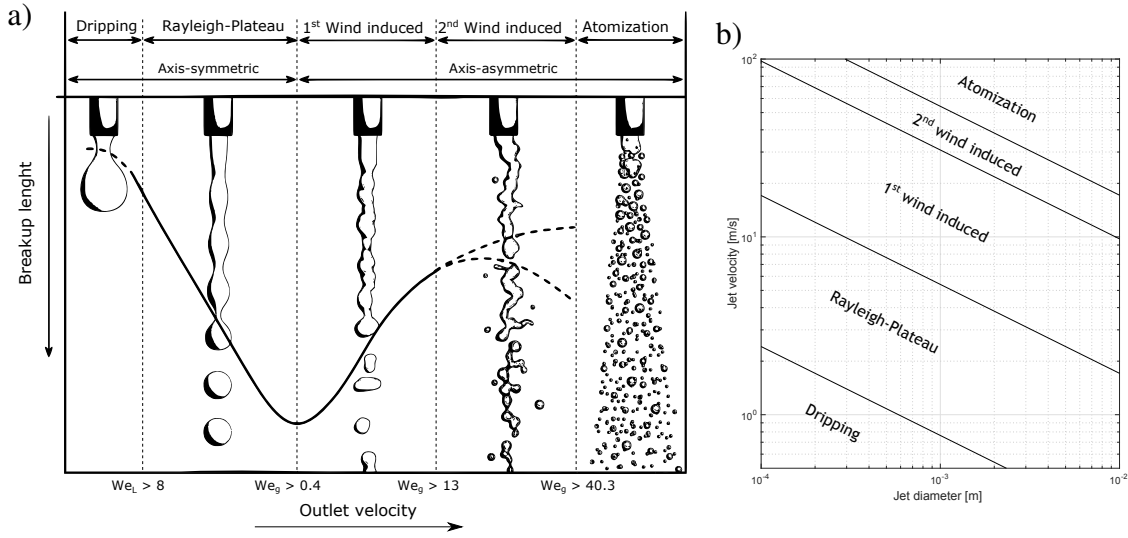


Fig. 1.4 Breakup regimes of a cylindrical water jet in still air at atmospheric pressure. a) Illustration of the breakup regime according to the jet velocity. Figure adapted from Bonhoeffer et al. (2017). b) Breakup regime limits for a water jet in still air. The limits have been computed using the equations 1.1 and 1.2.

(Dumouchel, 2008):

$$We_L = \frac{\rho_L U^2 d_{jet}}{\sigma} \quad (1.1)$$

$$We_G = \frac{\rho_G U^2 d_{jet}}{\sigma} \quad (1.2)$$

with ρ_L and ρ_g the liquid and the gas density respectively [kg m^{-3}], U the jet velocity [m s^{-1}], d_{jet} the jet diameter [m] and σ the liquid surface tension [N m^{-1}]. The critical Weber numbers between each regime are indicated on the Figure 1.4 a. For the Rayleigh-Plateau regime (Dumouchel, 2008), the We_L has to be higher than 8 and the gaseous Weber number We_G has to be lower than 0.4. Using the equations 1.1 1.2, the domain of existence of each breakup regime can be described in respect to the jet diameter and velocity as shown on the Figure 1.4 b.

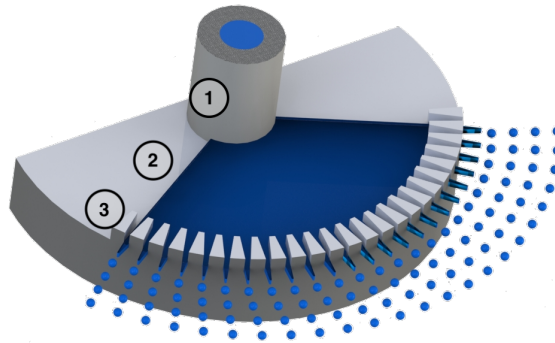


Fig. 1.5 Illustration of the nozzle with the three main regions: the nozzle pipe (1), the disk (2), the disk structures (3).

1.4 Thesis goals

The present PhD thesis aimed to design a hydraulic nozzle producing a spray with a narrow droplet size distribution. The nozzle design was similar to a splash plate nozzle for which the plate will be modified in order to split the liquid sheet formed on the plate into multiple jets at its end as shown on Figure 1.5. Three main regions of the nozzle can be distinguished: the nozzle pipe end, the disk, the disk border. In the two first regions the objective will be to generate a homogeneous flow in term of speed and thickness. Then at the disk border channels will be used in order to separate the liquid sheet in to multiple jets. In order to achieve a narrow droplet size distribution, the jets should breakup in the Rayleigh-Plateau regime. Unlike the rotary atomizer, the hydraulic nozzle will not have any rotating part. The droplet size distribution of the spray will be determined by the jet speed and size emitted at the edge of the plate. Therefore, according the targeted diameter and flow rate, a specific geometry has to be designed. The design procedure ends by the experimental characterization of the droplet size distribution generated by a prototype. The thesis has three main goals:

- Determination of an optimum range of droplet sizes for drift tolerant herbicide application.
- The analytical description of the flow on the nozzle plate according to the inlet geometry.
- The development of an experimental technique for the characterization of agricultural sprays.

1.5 Thesis organization

Chapter 2 aims to determine an optimum range of droplet sizes for boom-sprayer applying herbicide using a modeling approach. The main parameters of spray deposition and retention models are systematically varied and the effects on drift potential and droplet impaction outcomes are discussed. In chapter 3, an optical technique developed to characterize agricultural sprays is presented. The droplet size and speed are measured using high speed imaging set-up. This technique has been used to assess a nozzle prototype. Chapters 4 and 5 aim to describe analytically the flow on the nozzle plate. The Chapter 4 presents and assess the numerical method which will be used in Chapter 5 to build the analytical model. This analytical model provides the liquid sheet thickness and velocity according the radial distance from the nozzle center. Finally, using the latter model and the droplet size objective a nozzle design is established in the chapter 6. An upscale nozzle prototype, is assessed experimentally using the high speed imaging technique developed earlier.

The chapters 2, 5 and 3 are constituted of publish peer-reviewed paper. The chapter 4 is a conference paper and the chapter 6 is an original contribution.

Chapter 2

Investigation on optimal spray properties for ground based agricultural applications using deposition and retention models

2.1 Preamble

The optimal droplet size distribution for weed control has to be a balance between the droplet drift by the wind and the droplet kinetic energy when it reaches the target. Let's consider a droplet falling from a given height with an initial velocity through a horizontal air flow. During its flight, the droplet velocity is evolving toward an equilibrium with the surrounding air flow. The equilibrium state corresponds to the settling velocity in the vertical axis and the wind velocity in the horizontal axis. The droplet time of flight is linked to the initial droplet properties, i.e. its size, velocity and release height. The work presented in the present chapter assess the sensitivity of the initial droplet properties on the drift and retention potentials. This work has been published in a peer reviewed journal. The details of the publication are presented in the Table 2.1.

2.2 Introduction

Spray application is a key process in crop protection to ensure high yields whilst minimizing the adverse environmental and health impact of plant protection products. During this process, the agricultural mixture is usually atomized by passage through a nozzle generating

Table 2.1 Summary of the appended publication.

Authors:	De Cock, Nicolas & Massinon, Mathieu & Ouled Taleb Salah, Sofiene & Lebeau, Frédéric
Year:	2017
Title:	Investigation on optimal spray properties for ground based agricultural applications using deposition and retention models
Status:	In press
Peer reviewed:	Yes
Journal:	Biosystem engineering
URL:	Not available yet

a liquid sheet that further breaks up in a cloud of droplets. A herbicide application can be divided in four successive stages: deposition (initial spray amount minus off-target losses), retention (amount remaining on the plant after impaction), uptake (amount of active ingredient taken into the plant foliage) and translocation (amount of absorbed material translocated) (Zabkiewicz, 2007). This paper focuses on deposition and retention stages.

It has been shown that the droplet size distribution of the spray significantly affects the deposition (Hilz and Vermeer, 2013; Nuyttens et al., 2007b; Stainier et al., 2006; Taylor et al., 2004). Al Heidary et al. (2014) showed that spray drift decreases with the droplet kinetic energy following a power law. Indeed, finer droplets are more prone to drift leading to potential product losses in the air, water and soil (Reichenberger et al., 2007). Modeling of deposition under field conditions has been realized using several approaches: Gaussian plume model (Baetens et al., 2009; Lebeau et al., 2011; Raupach et al., 2001), Lagrangian models (Butler Ellis and Miller, 2010; Holterman et al., 1997; Mokeba et al., 1997; Teske et al., 2002; Walklate, 1987), computational fluid dynamics (CFD) (Baetens et al., 2007; Weiner and Parkin, 1993). Here a Lagrangian stochastic model will be used. Lagrangian stochastic models compute the droplet movement through an airflow using discrete time steps. The airflow turbulence is taken into account by superposing a time correlated fluctuating component onto a mean component. Dispersal statistics can be retrieved by tracking a large number of droplets.

The amount of spray remaining on a plant after impact is determined by the sum of each droplet impact outcomes (adhesion, bounce or shatter). Droplet behavior after impact is mainly governed by droplet kinetic energy, liquid surface tension and the surface wettability (Josserand and Thoroddsen, 2016; Yarin, 2006). When a droplet hits a solid surface, it spreads radially producing a thin liquid layer. If the droplet kinetic energy at impact overcomes capillary forces, the droplet shatters in smaller droplets. Otherwise, the spreading driven by the initial kinetic energy of the droplet is decelerated by viscous forces and surface tension,

Nomenclature

Greek Symbols

β	Droplet release angle [°]
Δt	Time step [s]
η, ε	Random value from a standard normal distribution [-]
γ	Surface tension [Nm^{-1}]
κ	von Karman constant [-]
λ, K	Weibull distribution parameter [-]
μ	Dynamic viscosity [$N s m^{-2}$]
ν	Kinematic viscosity [$m s^{-2}$]
ρ	Volumetric mass [$kg m^{-3}$]
$\sigma_{x,z}$	Velocity RMS [$m s^{-1}$]
τ_L	Lagrangian time scale of turbulence [s]
τ_L^*	Modified Lagrangian timescale [s]
θ	Static contact angle [°]

Roman Symbols

\dot{m}	Mass flux [$kg s^{-1}$]
C_D	Drag coefficient [-]
CDF	Cumulative density function [-]
d	Droplet diameter [m]
d_0	Zero plane displacement [m]
d_m	Maximum spread diameter [m]
E	Arithmetic mean of droplet traveled distance [m]

g	Gravity acceleration [$m s^{-2}$]
h_c	Crop height [m]
h_r	Release height [m]
k	Liquid to gas dynamic viscosity ratio [-]
L	Monin-Obukhov length [m]
m	Droplet mass [kg]
Re	Reynolds number [-]
RSF	Relative span factor [-]
ToF	Time of flight [s]
U	Air flow velocity [$m s^{-1}$]
u	Droplet velocity [$m s^{-1}$]
U^*	Friction velocity [$m s^{-1}$]
u_0	Release velocity [$m s^{-1}$]
V_r	Relative droplet velocity [$m s^{-1}$]
We	Weber number [-]
x	Horizontal position [m]
z	Vertical position [m]
z_0	Surface roughness [m]

Subscripts

g	Gaseous
l	Liquid

until radial dispersion stops. Thereafter, the liquid layer can remain pinned on the surface or retract. If the droplet surface energy is sufficient, the droplet may detach itself from the surface leading to a bounce (Attané et al., 2007). Otherwise, the droplet adheres on the surface. Massinon et al. (2015) proposed an empirical probabilistic model using droplet Weber number to model droplet outcomes on plant leaves. Deterministic models of impact outcomes based on energy balance of the impacting droplet are also available (Dorr et al., 2015; Mao et al., 1997; Mundo et al., 1995).

One common approach to reduce drift is to shift the droplet spectrum towards coarser droplets using low-drift nozzle or by adding spray additives. However, coarse droplets present a relatively low degree of surface coverage and may bounce or shatter on the target (Hilz and Vermeer, 2013; Massinon et al., 2017). An other solution, is to narrow the droplet size distribution towards an intermediate range of droplet size.

The goal of the present paper is to determine an optimum range of droplet size for boom-sprayer based herbicide applications using a modelling approach. A deposition model based on a stochastic Lagrangian approach is presented in the section 2.3.1. The mathematical models determining the droplet outcomes at canopy level are presented in the section 2.3.2. Deposition and retention models are used to realize a sensitivity analysis on initial droplet parameters (diameter, release height, release velocity) and environmental characteristics (wind speed, relative humidity) in the agricultural range detailed in section 2.3.4. Finally, the aerial transport and the retention of sprays with different volumetric median diameter and relative span factor are assessed in section 2.3.4.

2.3 Materials and methods

2.3.1 Droplet deposition model

General overview of the droplet transport model

Figure 2.1 shows the flow chart of the model. The simulation starts by initializing the droplet characteristics, e.g. its initial location, velocity and size. The acceleration and the evaporation of the droplet is then computed at each time step. In order to solve the aerodynamic balance of the droplet, the air flow characteristics are computed as well at each droplet location taking into account atmospheric turbulence. The simulation ends when the droplet either loses all its mass or reaches the crop level canopy where the droplet is stated to be captured. Air entrainment from the spray nozzle is not taken in account in the present model because of a low drop/air mass ratio is assumed which is typical of low application volume/high speed applications (Lebeau, 2004).

Droplet motion

Equations of droplet motion are taken from the saltation model of Kok and Renno (2009), which takes into account the particle inertia. The droplet transport model uses a Lagrangian description of the droplet motion. The displacement of the droplet after a time t is given by the numerical integration of the droplet velocity over time:

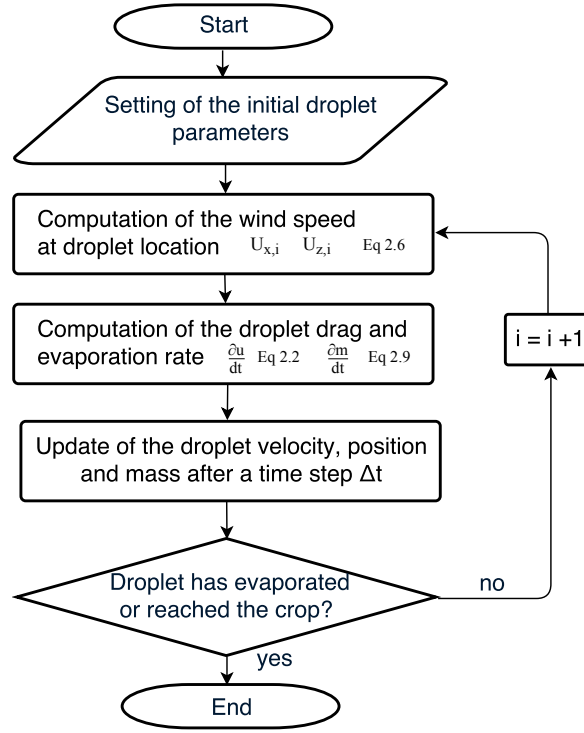


Fig. 2.1 Flow chart of the droplet transport model.

$$\Delta x_i = \sum_i^n u_{x,i} \Delta t_i \quad \& \quad \Delta z_i = \sum_i^n u_{z,i} \Delta t_i \quad (2.1)$$

The variation of the droplet velocity is retrieved using Newton's second law of motion taking in account the effects of drag and gravity while neglecting the buoyancy.

$$\begin{aligned} \frac{\partial u_x}{\partial t} &= \frac{3C_D \rho_g V_r (U_x - u_x)}{4\rho_l d} \\ \frac{\partial u_z}{\partial t} &= \frac{3C_D \rho_g V_r (U_z - u_z)}{4\rho_l d} - g \end{aligned} \quad (2.2)$$

with m the droplet mass [kg], u the droplet velocity [m s^{-1}], t the time [s], C_D the drag coefficient [-], ρ_l and ρ_g the density of the liquid and gaseous phases respectively [kg m^{-3}], A the droplet cross section area [m^2], d the droplet diameter [m], U and u are the air and the droplet velocity respectively [m s^{-1}], V_r is the relative velocity between the droplet and the airflow defined as $V_r = |u - U|$ [m s^{-1}], and g is the gravitational acceleration rounded to 9.81 [m s^{-2}].

For $Re \leq 400$ the drag coefficient of a sphere in a gas flow can be expressed using the following expression (Saboni et al., 2004):

$$C_d = \frac{\left(k \left(\frac{24}{Re} + \frac{4}{Re^{0.36}}\right) + \frac{15}{Re^{0.82}} - 0.02 \frac{kRe^{0.5}}{1+k}\right) Re^2 + 40 \frac{3k+2}{Re} + 15k + 10}{(1+k)(5 + 0.95Re^2)} \quad (2.3)$$

with k equal to the ratio of the liquid to the gas viscosity, $k = \frac{\mu_l}{\mu_g}$, and Re the droplet Reynolds number defined as: $Re = \frac{V_r d}{\nu_g}$. Other C_d expressions for a sphere can be found in the literature (Barati et al., 2014; Langmuir and Blodgett, 1949).

Description of the air flow

The velocity profile generated by a wind above crop is made up of a random part sum onto a mean component. Assuming the vertical mean flow equal to zero, the general formulation is reduced to:

$$U_x = \bar{U}_x + U'_x; \quad U_z = U'_z \quad (2.4)$$

The average part of the horizontal velocity $\bar{U}(z_i)$ is described by a logarithmic velocity profile:

$$\bar{U}(z_i) = \frac{U^*}{\kappa} \log \left(\frac{z - d_0}{z_0} \right) \quad (2.5)$$

with κ the von Karman constant equals to 0.41 [-], U^* the friction velocity [m s^{-1}], z the distance above the ground [m], d_0 the zero plane displacement [m] and z_0 the surface roughness [m]. The values d_0 and z_0 can be related to crop height using $z_0 = 0.1 h_c$ and $d_0 = 0.63 h_c$ with h_c the crop height (Butler Ellis and Miller, 2010).

For homogeneous isotropic turbulence, the velocity fluctuations U' of an air particle moving with the flow can be statically described by the following set of equations (Kok and Renno, 2009) (Wilson and Sawford, 1996):

$$\begin{aligned} U'_{x,i+1} &= U'_{x,i} e^{-\frac{\Delta t}{\tau_{Lx}^*}} + \varepsilon \sigma_x \sqrt{2} \left(1 - e^{-\sqrt{\frac{\Delta t}{\tau_{Lx}^*}}} \right) \\ U'_{z,i+1} &= U'_{z,i} e^{-\frac{\Delta t}{\tau_{Lz}^*}} + \eta \sigma_z \sqrt{2} \left(1 - e^{-\sqrt{\frac{\Delta t}{\tau_{Lz}^*}}} \right) \end{aligned} \quad (2.6)$$

with τ_L^* the modified Lagrangian time scale [s], Δt is the time step [s], η and ε are random variables from a standard normal distribution [-], σ_x and σ_z are the horizontal and the vertical

velocity fluctuations [m s^{-1}]. For near neutral atmospheric conditions: $\sigma_x = 2.3 U^*$ and $\sigma_z = 1.3 U^*$ (Panofsky et al., 1977).

The Lagrangian timescale represents the approximate timescale over which the velocities experienced by an air particle are statically related. Since the droplets move through the air eddies, the Lagrangian timescale perceived by the droplets is shorter. A modified formulation of the Lagrangian timescale for the horizontal and the vertical directions was proposed by (Sawford and Guest, 1991):

$$\begin{aligned}\tau_{Lx}^* &= \frac{\tau_{Lx}}{\sqrt{1 + \left(2 \frac{V_x}{\sigma_x}\right)^2}} \\ \tau_{Lz}^* &= \frac{\tau_{Lz}}{\sqrt{1 + \left(\frac{V_z}{\sigma_z}\right)^2}}\end{aligned}\quad (2.7)$$

with τ_L defined as (Butler Ellis and Miller, 2010):

$$\tau_L = \kappa U^* \frac{(z - d_0)}{\sigma_z^2} \sqrt{1 - \left(\frac{16(z - d_0)}{L}\right)} \quad (2.8)$$

with L the Monin-Obukhov length [m], which characterises atmospheric stability.

Droplet evaporation

Droplet evaporation in the model was based on Guella et al. (2008). The set of equations used are described in the Appendix A. In this model, the air has a constant vapor fraction and temperature. The loss of droplet volume is computed after each time step as:

$$\Delta V = \frac{\dot{m}}{\rho_l} \Delta t \quad (2.9)$$

2.3.2 Droplet retention model

Mathematical models have been developed to predict the outcome of impacting droplets based on an energy balance approach (Dorr et al., 2015; Mao et al., 1997; Mundo et al., 1995). In these models, three impact outcomes are considered: adhesion, bounce or shatter. Shatter occurs when the inertial forces at impacting overcome the capillary forces. The droplet shatter threshold may be predicted based on droplet Reynolds number and Weber number (Mundo et al., 1995):

$$K = We^{0.5} Re_I^{0.25} \quad (2.10)$$

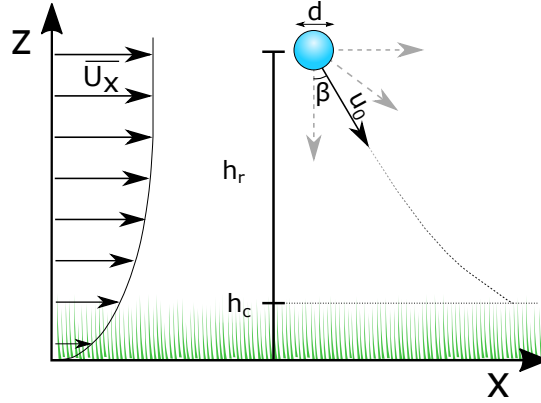


Fig. 2.2 Initial configuration of the deposition model.

Unlike for the drag coefficient, the Reynolds number of the droplet at impaction Re_I is computed using the liquid kinematic viscosity: $Re_I = \frac{u_z d}{\nu_l}$. The Weber number is expressed as: $We = \frac{u_z^2 \rho_l d}{\gamma}$ with γ the liquid surface tension [N m^{-1}]. Experimental measurements have shown that the droplets shatter when $We^{0.5} Re_I^{0.25} \geq K_{crit}$ (Mundo et al., 1995). If the droplet does not shatter, the model assesses the bounce criteria. Mao et al. (1997) proposed a semi-empirical model based on energy conservation providing a rebound criteria. Bounce occurs if the excess rebound energy E_{ERE}^* is positive otherwise the droplet is predicted to adhere to the leaf. The excess rebound energy is defined as:

$$E_{ERE}^* = \frac{1}{4} \left(\frac{d_m}{d} \right)^2 (1 - \cos \theta) + \frac{2}{3} \left(\frac{d}{d_m} \right) - 0.12 \left(\frac{d_m}{d} \right)^{2.3} (1 - \cos \theta)^{0.63} - 1 \quad (2.11)$$

with d_m the maximum spread diameter [m] and θ the static contact angle [$^\circ$].

The value of d_m in the Eq. 2.11 was, in turn, derived as an implicit function of We , Re and θ :

$$\left[0.25 (1 - \cos \theta) + 0.2 \frac{We^{0.83}}{Re_I^{0.33}} \right] \left(\frac{d_m}{d} \right)^3 - \left(\frac{We}{12} + 1 \right) \left(\frac{d_m}{d} \right) + \frac{2}{3} = 0 \quad (2.12)$$

If there is no real solution for d_m in the Eq. 2.12 or if the computed d_m is $\leq d$, the value of d_m is set as equal to d .

2.3.3 Numerical procedure

Figure 2.2 illustrates the initial state of the simulation. The initial droplet location is set as $x = 0$ and $z = h_r + h_c$ with z_r the release droplet height [m]. The initial droplet velocity in both directions are: $u_x = |u_0| \cos(\beta)$; $u_z = |u_0| \sin(\beta)$, with β the angle between the initial

Table 2.2 Simulation constants. The air and water temperature properties were taken both for 15 °C. Subscript *g* and *l* refer to gaseous and liquid phases respectively.

Parameter	Value	Units
μ_g	1.85e-5	Pa s
μ_l	1.15e-3	Pa s
ρ_g	1.2	kg m ⁻³
ρ_l	1000	kg m ⁻³
h_c	0.1	m
L	-1000	m

droplet direction and the vertical direction [°] and u_0 the release velocity [m s⁻¹]. Liquid and air properties used for the computations are shown in the Table 2.2. The time step Δt was computed as: $\min\left(\frac{0.1h}{V_r}, \frac{\tau_L}{10}\right)$ [s].

2.3.4 Parameter sensitivity study

Monosized droplets

A sensitivity analysis was performed to highlight the effect of the droplet diameter d , wind speed at a height of 2 m $\bar{U}(2)$, droplet release velocity u_0 , release angle β , the release height above crop h_r and relative humidity HR may have on the deposition and retention steps. The variation of these parameters are shown in the Table 2.3. For each instance, the trajectories of 15 000 droplets with the same initial conditions were computed. Random wind fluctuations experienced by the droplets during their flights lead to a variety of trajectories that were characterized by statistical parameters such as mean, 5th, 50th (median) and 95th percentiles. Later in the paper, if the value of one parameter is not specified, the standard values indicated in bold in Table 2.3 were used.

The impact outcomes were evaluated on a wheat leaf with water which has a static contact angle of 132 ° and a K_{crit} of 69 (Forster et al., 2010). Water has a surface tension γ of 0.072 N m⁻¹.

Polydisperse sprays

The aerial transport of polydisperse sprays of droplets are simulated in order to predict the effect of the droplet size distribution on the overall deposition and retention. Each spray cloud was simulated by 100 000 droplets randomly drawn from a Weibull distribution in volumetric cumulative distribution (CDF) defined as: $CDF = 1 - e^{-\left(\frac{x}{\lambda}\right)^K}$ (Babinsky and Sojka, 2002; Rosin and Rammler, 1933). The two Weibull distribution parameters were set to

Table 2.3 Range of variation of the simulation parameters. The standard values are highlighted in bold.

Variable	Tested values	Units
d	100;125;150;175;200;250;300;350;400	μm
$\bar{U}(2)$	0;2;4;6;8	$m s^{-1}$
$ u_0 $	5; 10 ;15	$m s^{-1}$
β	0 ;15;30;45;60;75;90	$^\circ$
h_r	0.25; 0.5 ;0.75;1	m
Hr	40;60; 80	%

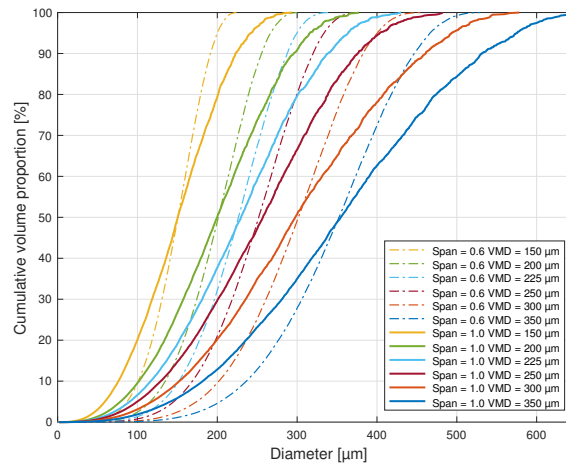


Fig. 2.3 Cumulative droplet size distribution of the virtual sprays for the six Dv_{50} and the two RSF .

achieve a specific relative span factor RSF and volumetric mean diameter Dv_{50} . The relative span factor is defined as $RSF = \frac{Dv_{90} - Dv_{10}}{Dv_{50}}$ with Dv_{10} , Dv_{50} and Dv_{90} corresponding to the maximum droplet diameter below which 10%, 50% and 90% of the volume of the sample exists, respectively. Six different values of Dv_{50} (150, 200, 225, 250, 300, 350 μm) and two RSF (0.6, 1) were simulated resulting in twelve different simulations. The twelve simulated droplet size distributions are shown in Fig.2.3.

Sprays characterized with a RSF of 0.6 and 1 are representative of the narrow spray droplet size distributions produced by rotary atomizers (Qi et al., 2008) and flat fan nozzles respectively (De Cock et al., 2016; Nuyttens et al., 2007a). A Dv_{50} of 250 μm with a RSF of 1 is similar to a spray generated by a flat fan nozzle 110-03 operating at at 300 kPa. For all these cases, simulation parameters were set to standard values (Table 2.3).

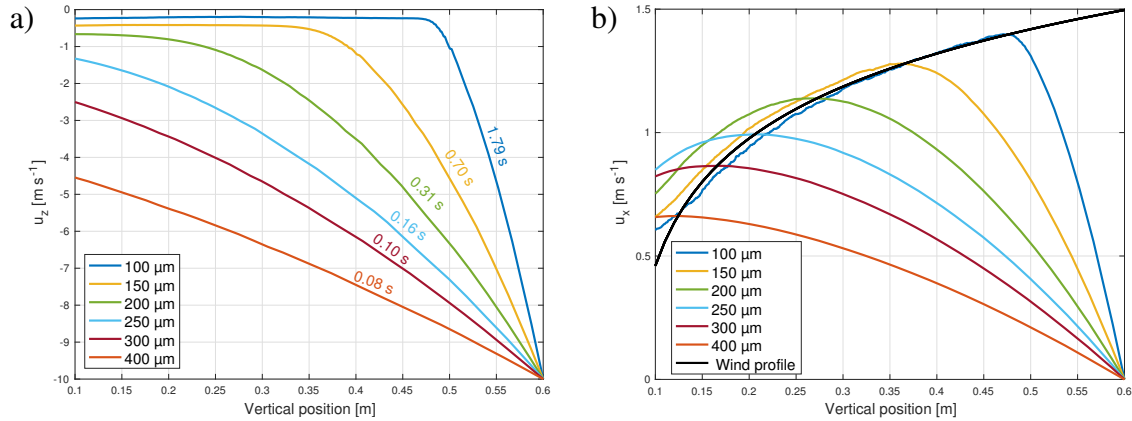


Fig. 2.4 Dynamics of droplet velocity during its flight. a) Median vertical velocity with respect to the droplet vertical location. The median time of flight to travel from the release point to the crop top canopy for each droplet size is indicated above each corresponding line. b) Median horizontal velocity with respect to the droplet vertical location. The average wind velocity profile defined by the Eq.2.5 for a reference wind of 2 m s^{-1} at 2 m is illustrated by the black curve.

2.4 Results

2.4.1 Sensitivity analysis of a population of monodisperse droplets

Effect of droplet size on velocity dynamics

Figure 2.4 a shows the evolution of the vertical median droplet velocity with respect to the droplet vertical position. The droplets are released 0.6 m above a crop of 0.1 m high with an initial horizontal velocity u_x of 0 m s^{-1} and an initial vertical velocity u_z of -10 m s^{-1} . The droplets were decelerating in the vertical direction approaching their settling velocity whilst, in the horizontal direction, the droplets were accelerating towards the wind velocity. The droplets with a diameter $\geq 250 \mu\text{m}$ reached the crop canopy with a vertical velocity above their settling velocity. The median time of flight (ToF) for each droplet size is shown next to each line. The ToF is the time between the droplet release and its deposit on the canopy. Droplet ToF is shown decreasing with increasing droplet size. The 100 μm diameter droplets had, on average, 20 times longer ToF than 400 μm diameter droplets. The ToF ratio between the 250 μm and the 400 μm diameter droplets was around 2.

Figure 2.4 b shows the evolution of the horizontal median droplet velocity with respect to the droplet vertical position. All droplet sizes reached the top canopy level at a horizontal velocity approximately equal to the average wind velocity. An overshoot of the wind velocity was observed for larger droplets due to their inertia, e.g. 250 μm droplets are faster than the wind at $z \leq 0.2 \text{ m}$.

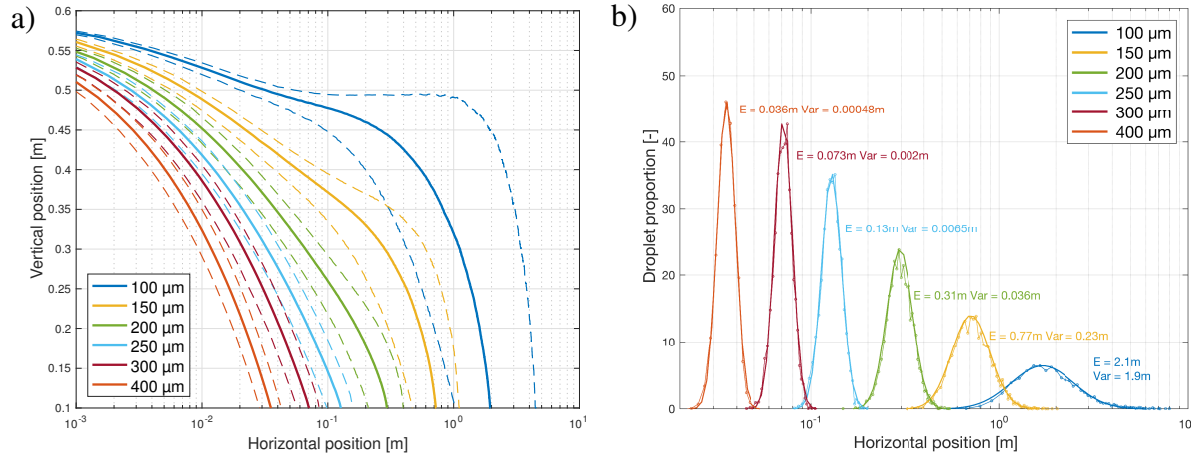


Fig. 2.5 Droplet deposition trajectories under a wind of 2 m s^{-1} . a) 5^{th} percentile, median and 95^{th} percentile trajectories for 6 different droplet sizes under standard conditions. b) Deposition pattern of 15 000 droplets with the same size under standard conditions. The line with the bullets represents the simulated data and the full lines represents the log-normal fit. The log-normal distribution arithmetic mean and the arithmetic variance are displayed above each curves. Details on these parameters are available in the Appendix B.

Droplet trajectories

The random wind fluctuations experienced by the droplets lead to a variability of trajectories among the simulations. Figure 2.5 a shows the 5^{th} , 50^{th} (median) and 95^{th} percentile of the trajectories of 15 000 droplets under reference conditions (cf Table 2.3). The median is represented by the solid line. The 5^{th} and 95^{th} percentile are represented by the left and the right dashed line respectively. The coarser the droplet, the shorter the horizontal distance travelled and the dispersion of the traveled distance. The droplets with diameter larger than $200 \mu\text{m}$ reached the canopy within 1 m from the release position with a dispersion shorter than 0.1 m.

The 95^{th} percentile curve for the $100 \mu\text{m}$ droplet features a plateau between 0.1 m and 1 m. This plateau arises from a succession of random velocity fluctuations directed upwards. At a wind speed of 2 m s^{-1} at 2 m height, the vertical velocity fluctuations are equal to $u'_z = 0.284 \varepsilon$ with ε a random standard Gaussian value which is in the same range than the settling velocity of droplet of $100 \mu\text{m}$ (i.e. 0.29 m s^{-1}). Computations (not displayed here for brevity) showed that with a higher wind speeds, the plateau forms a bell shape due to the increase in the strength of the vertical velocity fluctuations.

The simulated relative deposition patterns over distance is shown in Figure 2.5 b by dashed with bullets. The full line represents the log-normal fit on the simulated data. The fitted and simulated data are in good agreement. The next subsection assess the effect of the

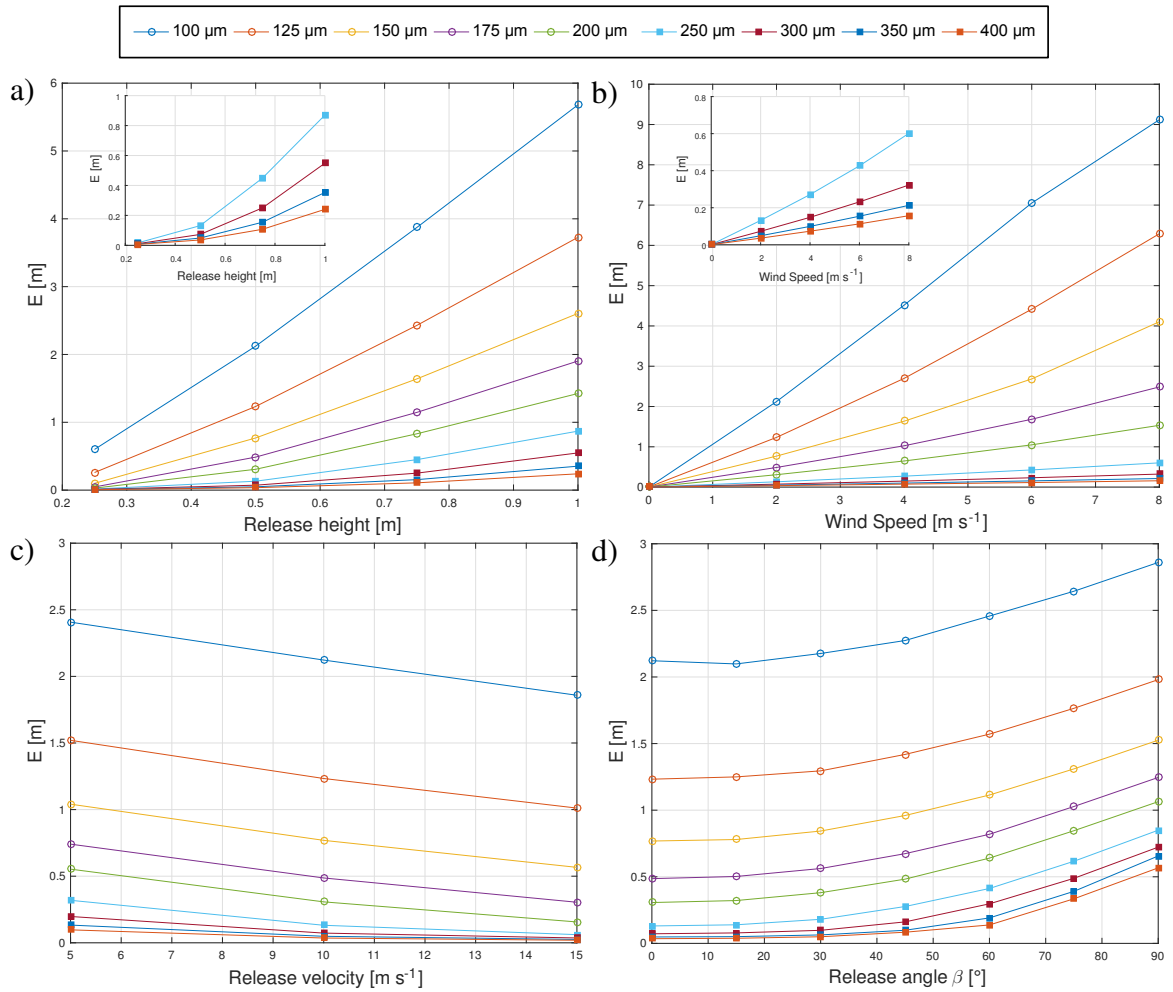


Fig. 2.6 Effect of the release height, wind speed, release velocity and release angle on the average of the log-normal fit arithmetic mean E .

wind speed and the release parameters on the arithmetic mean of the log-normal distribution. The value of the arithmetic mean has been retrieved with a least square fitting of the log-normal parameters on the numerical data using Matlab (MATLAB 9.0, The MathWorks Inc., Natick, MA, USA). More details about the log-normal distribution and the reduced parameters are furnished in the Appendix B.

Average droplet transport

The results of the arithmetic mean E [m] with respect to variation of the ejection height, ejection angle, wind speed and ejection velocity are presented in Fig.2.6. The horizontal distance traveled by a droplet was correlated with droplet ToF and wind speed. ToF decreased with decreasing release velocity and increasing droplet settling velocity. The release height

increased the average displacement, mainly for droplet smaller than $250 \mu m$. For fine droplets, the release height was roughly proportional to the ToF since the droplets quickly reached their settling velocities, leading to a linear relationship between traveled distance and release height. For droplets coarser than $200 \mu m$, the latter relationship was not linear because larger droplets decelerate during their fall. The traveled distance linearly increased with increasing wind speed. Finer droplets were more sensitive to wind speed, resulting in steeper slopes in the graph of Fig.2.6 b. Increase in the release velocity slightly decreased the traveled distance for the finer droplets (- 20% for $100 \mu m$ $5-15 \text{ m s}^{-1}$) whilst the decrease was substantial for coarse droplets (- 80% for $400 \mu m$ $5-15 \text{ m s}^{-1}$) which relates to droplet inertia. The effect of the release angle β is shown in Fig.2.6 d. For each angle, the average displacement without wind was subtracted to consider the effect of these angles. The increase of β leads to a decrease in initial vertical velocity and an increase of the initial horizontal velocity, increasing the averaged traveled distance. Droplets with diameter $\geq 200 \mu m$ had an average horizontal displacement shorter than 0.5 m for release angle $\leq 60^\circ$.

Droplet transport of 95th percentile

X_{95} represents the downwind distance by which 95 % of the spray volume has reached the ground. It corresponds to the final position of the 95th percentile trajectories shown in Fig.2.5 a. This parameter was responsive to the average transport of the droplet spray and deposition dispersion. The effect of the main parameters on the X_{95} is shown in Fig.2.7. The increase of release height was linear with increasing X_{95} , similarly to Fig.2.6 a. However, the decrease of the slope with increasing droplet size was stronger than for the average displacement since the increase of height also enhanced the deposition variability. The increase of wind speed generated a quadratic increase of the X_{95} . This can be explained by an increase in the random wind fluctuations which in turn enhanced the variability of the droplet trajectories. Therefore, the log-normal curves representing the volume distribution over distance were strongly flattened. At wind speeds of 8 m s^{-1} , more than 5 % of the droplets of $100 \mu m$ traveled further than 100 m. This distance dropped below 1 m for droplets with diameter $\geq 250 \mu m$. The increase of the release velocity led to a moderate decrease of X_{95} . Thus, acting solely on the release velocity does not significantly affect drift. The increase of β led to an increase of X_{95} , especially for coarser droplets at release angles from 60° to 90° . At an angle of 60° , less than 5 % of the droplets with diameter $\geq 200 \mu m$ were airborne further than 1 m. X_{95} was strongly influence by droplet size due to the higher deposition variability and higher average displacement for finer droplets. This means that droplets diameter $\leq 150 \mu m$ should be minimized within the spray since a significant proportion will travel several metres. E and X_{95} were close to each other for droplets with diameter

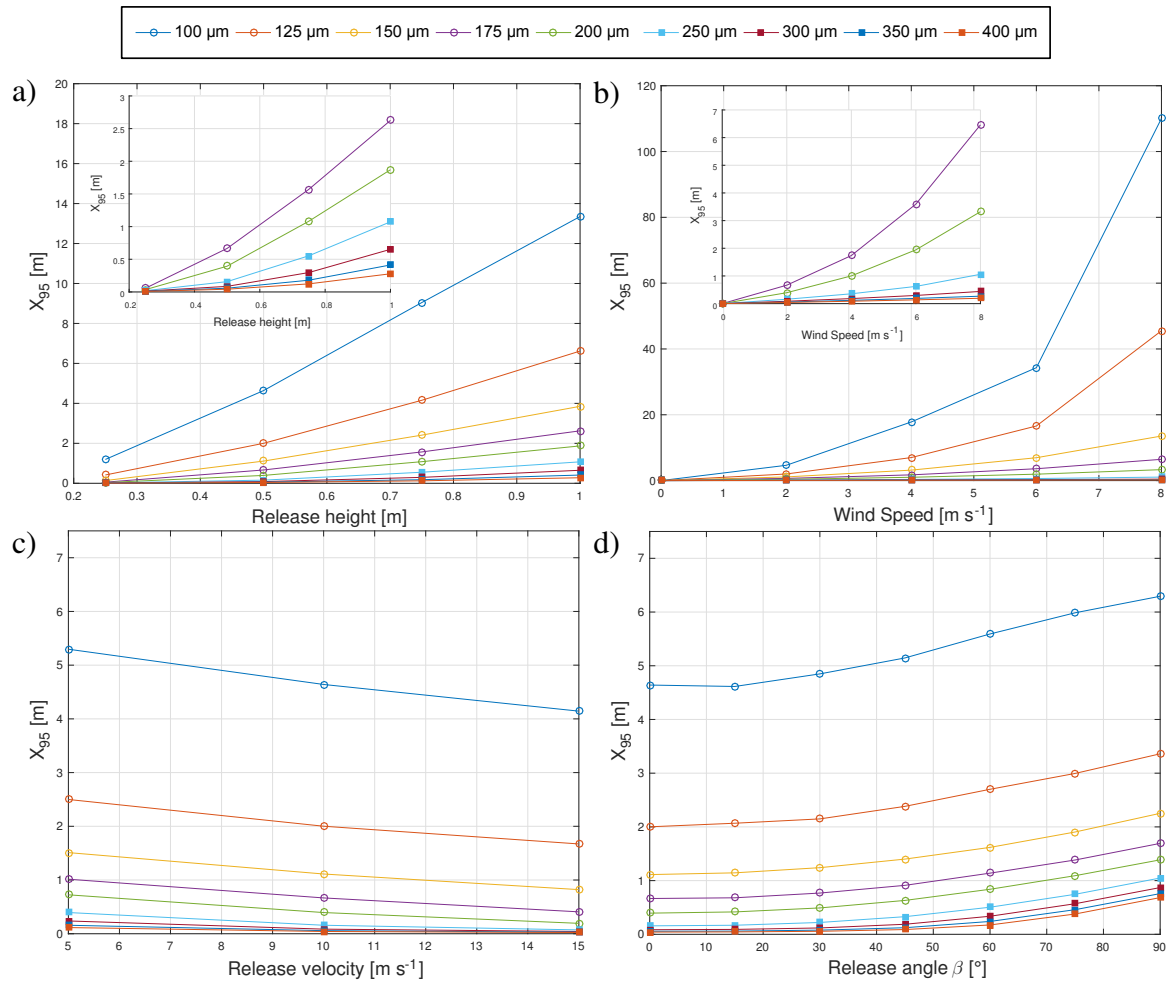


Fig. 2.7 Effect of the release height, wind speed, release velocity and release angle on the distance above which 95 % of the droplets have reach the top canopy level X_{95} .

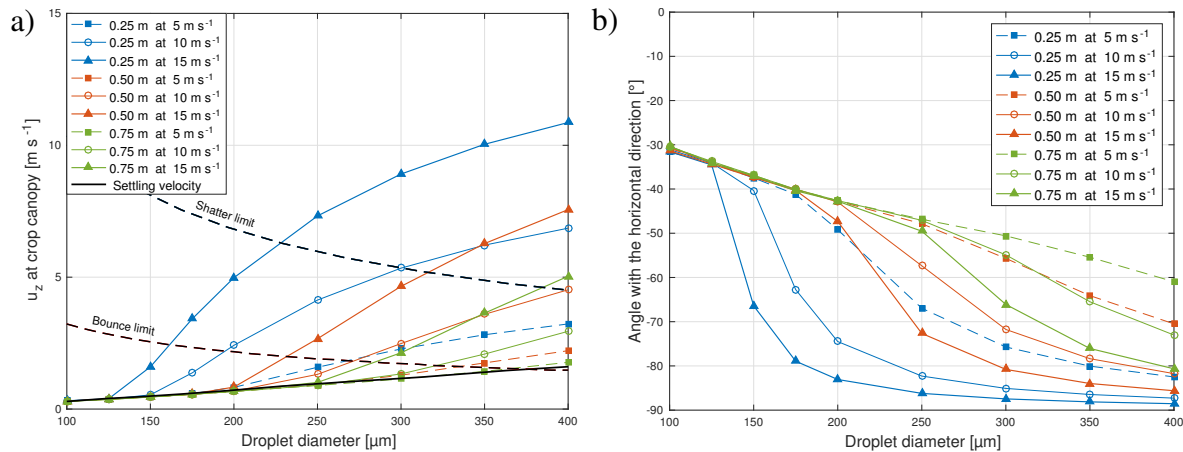


Fig. 2.8 Droplet velocity and angle at top canopy level. a) Average impact velocity in respect to the droplet diameter for three release heights and three release velocities. The dashed line shows the velocity above which a droplet would shatter or bounce while impact a wheat leaf using the adhesion model described in section 2.3.2. b) Average droplet trajectory angle at the crop top canopy level with the horizontal direction. The other simulation parameters were set at standard values (cf Table 2.3).

$\geq 250 \mu\text{m}$ showing a low dispersion of droplet trajectories. This low dispersion can be explained by their shorter ToF relatively to finer droplets.

Droplet velocity at top canopy level

Figure 2.8 a shows the average droplet vertical velocity at crop height for three release heights and three release velocities. The coarser the droplet, the shorter is the traveled distance and the faster it may impact on the target. The black line shows experimental measurements of settling velocities (Gunn and Kinzer, 1949). At a release height of 0.5 m, droplets smaller with diameter $\leq 200 \mu\text{m}$ reached their settling velocity. At $350 \mu\text{m}$ diameter, the 0.25 m and 10 m s^{-1} line crosses the 0.5 m 15 m s^{-1} line showing that the increase of release velocity overcomes the increase in flight distance for droplets with higher inertia. The black dashed line shows the thresholds for droplet bounce and shatter on a wheat leaf predicted for water (Dorr et al., 2015). For the whole range of droplet size studied, shatter occurs when the droplets move faster than their settling velocity. For standard simulation conditions (i.e. 0.5 m and 10 m s^{-1}) droplets larger than $400 \mu\text{m}$ shattered and droplets between 270 and $400 \mu\text{m}$ bounced. The mitigation of bounce and shatter can be done by increasing the release height or by decreasing the release velocity. Nevertheless, decreasing the release velocity was predicted as being less detrimental for the spray drift as shown in Fig.2.6 a,c.

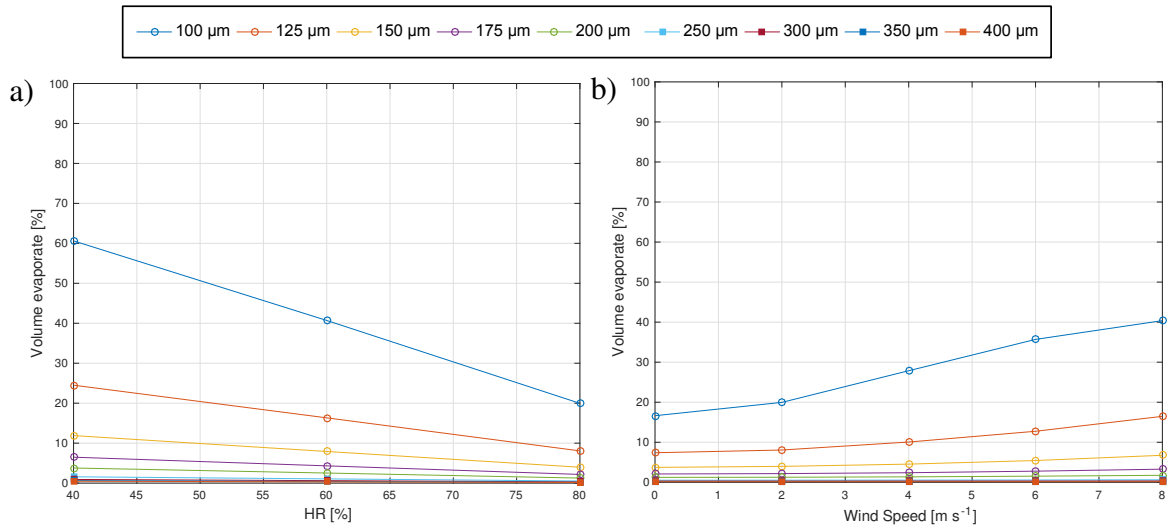


Fig. 2.9 Evolution of the relative volume evaporate in respect to the relative humidity and the wind speed.

Droplet trajectory at the top canopy affects the potential droplet retention. For graminicide application, vertical trajectories reduce the droplet capture probability by the target (Jensen, 2012; Spillman, 1984). Figure 2.8 b shows the average trajectory angles in respect with the horizontal direction under a wind of 2 m s^{-1} at 2 m above the crop. The droplet ToF and the droplet size will affect the final horizontal velocity whilst the droplet size, release height and the release velocity will determine the final vertical velocity. The fine and therefore slow droplets reach the canopy more horizontally than the coarse ones. For a release height of 0.5 m, the droplets reached the top of the canopy with roughly the same horizontal velocity as shown in Fig.2.4 b. Therefore, the difference in angle between droplet size may be mainly related to the vertical velocity component.

Droplet evaporation

The effect of the relative humidity HR , wind speed and droplet size on the evaporated fraction is shown in Fig.2.9. The evaporated fraction was computed by subtracting the volume of liquid reaching the top canopy from the initial volume released. Evaporation mainly affects droplets with diameter $\leq 150 \mu\text{m}$. Droplets with diameter $\geq 250 \mu\text{m}$ had moderate evaporation, i.e. $\leq 3\%$ for the worst scenario. Therefore, for droplet $\geq 250 \mu\text{m}$ diameter, the evaporation may not be a concern. The evaporation model does not take into account the small increase in vapour pressure in the surrounding air due to the droplet evaporation. Therefore the evaporation rate observed in real conditions could be lower.

2.4.2 Polydisperse sprays

Deposition

Figure 2.10 a shows the volume of spray airborne with respect to the distance from the nozzle for twelve simulations with different Dv_{50} and RSF . As expected, increasing Dv_{50} reduces the volume of airborne spray. Increasing Dv_{50} from $150 \mu m$ to $350 \mu m$ reduces the airborne spray at 2 m from 20 % to 2 %. Comparison of sprays with the same Dv_{50} shows that lower the RSF can reduce drift. For a Dv_{50} of $150 \mu m$, decreasing of RSF from 1 to 0.6 produces a reduction from 20 % to 12 % of the airborne spray at 2 m. Table 2.4 summarizes the airborne spray reduction at several distances induced by reducing the RSF from 1.0 to 0.6 computed as: $100 \frac{Drift_{0.6}}{Drift_{1.0}}$. The drift reduction produced by the RSF reduction increased with the Dv_{50} because the coarser the spray, the greater the relative reduction of the fine droplets. For the spray with a Dv_{50} of $250 \mu m$, drift reduction was around 80 % which corresponds to a three star rating in the LERAP scheme (Butler Ellis et al., 2017). For each Dv_{50} the drift reduction appeared to be roughly constant over distance.

Retention

Figure 2.11 shows the relative volume of each droplet impact for the twelve simulated sprays on a wheat leaf. For a given RSF , the increase of Dv_{50} leads to a monotonic decrease of adhesion and the emergence of bounce and shatter due to a progressive increase of larger droplet proportion. Reduction of RSF enhanced one outcome according to the Dv_{50} , for $Dv_{50} \leq 250 \mu m$ there was an increase of the adhesion whilst bounce increased for $Dv_{50} \geq 300 \mu m$. For standard conditions, the diameter threshold between adhesion and bounce is around $270 \mu m$ as shown in Fig.2.8 a. Therefore, a RSF reduction may be detrimental if the Dv_{50} is not in the adequate range as has already been noted in previous theoretical work (Massinon et al., 2016).

2.5 Discussion

The study of the droplet transport dynamic has shown that the size of a droplet affects its trajectory. The finer the droplet longer its time in the air making it more sensitive to evaporation and drift. The droplet ToF can be shortened by decreasing the release height or by increasing the release velocity. Release angle and release velocity have moderate effects on fine droplets. However for coarse droplets, increasing the release velocity increases the droplet velocity at the canopy and thus its outcome during impaction. The change of the release angle from vertical to horizontal direction leads to an increase in the traveled distance

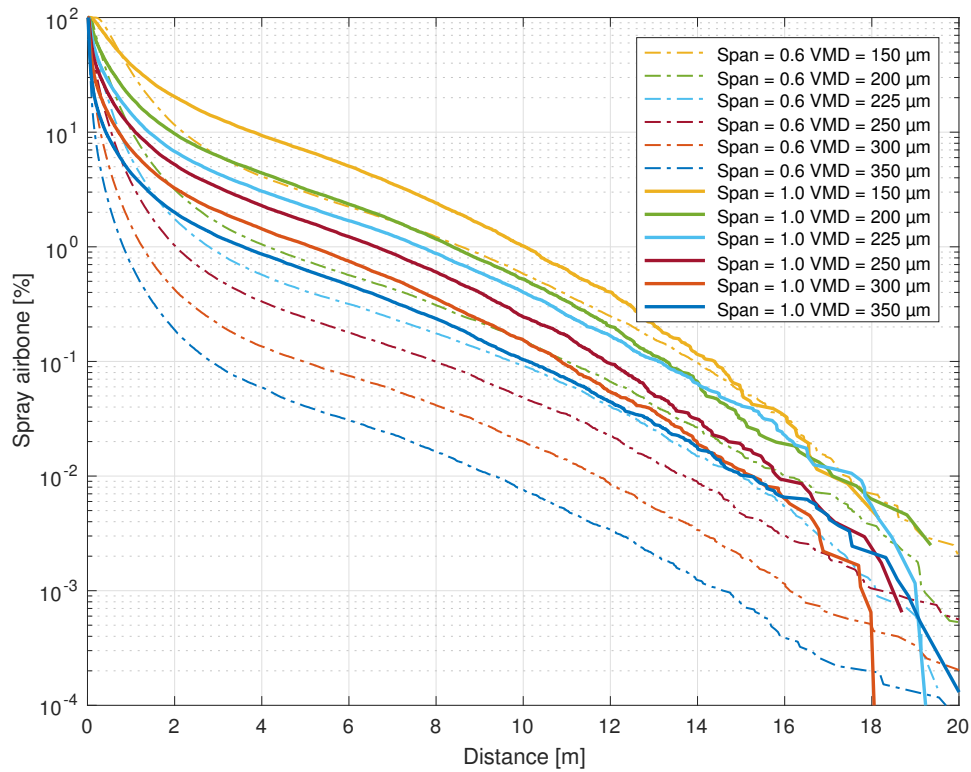


Fig. 2.10 Volume of airborne spray in respect with the distance. Twelve sprays were simulated with different D_{V50} and RSF values. The outcomes have been determined at the top canopy level using the models described in the section 2.3.2 for a release height of 0.5 m, a release speed of 10 m s^{-1} and 2 m s^{-1} wind speed.

Table 2.4 Airborne spray reduction [%] induced by a RSF reduction from 1.0 to 0.6. The airborne spray reduction is given for each D_{V50} at 5 distances from the release point.

	Distance [m]				
	2	4	6	8	10
150	43.4	56.0	55.7	49.2	42.9
200	67.3	76.1	76.0	73.5	70.8
225	74.2	81.3	81.2	79.9	77.2
250	80.3	85.4	85.4	83.5	80.4
300	87.0	90.6	90.0	88.3	87.0
350	90.6	93.1	93.4	93.1	92.7

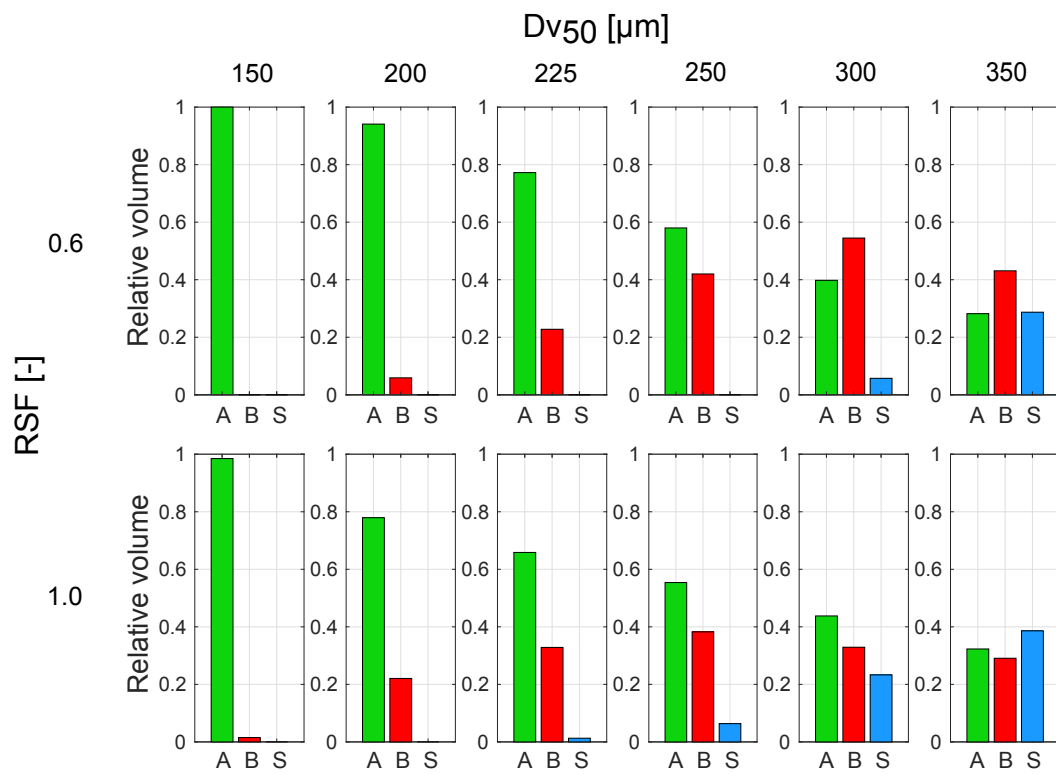


Fig. 2.11 Droplet impact outcome predictions at top canopy level expressed in relative volume. *A*, *B* and *S* correspond to adhesion, bounce and shatter respectively.

arising from both the initial horizontal velocity and the increase in ToF. An optimum value may be around 60° . The wind speed enhances the average droplet traveled distance linearly and the maximum distance quadratically. However, with droplets of $250 \mu\text{m}$, and 8 m s^{-1} wind speed 95 % of the spray reached canopy top level below 1 m from the release point. The shatter threshold on a wheat leaf was reached by droplets larger than $400 \mu\text{m}$ when the release height is at 0.5 m and the release speed at 10 m s^{-1} . With these initial conditions, bounce occurs for droplet between 270 and $400 \mu\text{m}$. Therefore, droplets with a diameter from 200 to $270 \mu\text{m}$ have a low drift potential and may not shatter or bounce on a wheat leaf.

For a polydisperse sprays, the overall behavior can be seen as the combination of drop size distribution and the properties of each droplet size. Drift and the volume of droplet adhesion decrease with increasing Dv_{50} . Narrowing the *RSF* of the spray may solve this problem. A spray with a Dv_{50} of $225 \mu\text{m}$ and a *RSF* of 0.6 released at 0.5 m at 10 m s^{-1} above the crop produces low drift with moderate kinetic energy at the crop canopy level. Using a Weibull distribution, this spray would have a Dv_{10} of $152 \mu\text{m}$, Dv_{90} of $288 \mu\text{m}$ with 1.4 % of the droplet volume $\leq 100 \mu\text{m}$ diameter and 9.5 % $\leq 150 \mu\text{m}$ diameter. The narrowing of the spray drift may be detrimental when the Dv_{50} is too small or too large which would enhanced drift or decreases retention.

2.6 Conclusion

A combined Lagrangian droplet transport and retention models has been presented. The deposition over distance had a log-normal distribution with a dispersion and average distance larger for finer droplets. The results of numerical simulations showed that droplets with diameters ranging between $200 \mu\text{m}$ and $250 \mu\text{m}$ offered high control of deposition by combining a low drift potential and moderate kinetic energy at the top of the canopy. The reduction of the *RSF* from 1.0 to 0.6 is an effective way to mitigate deposition and retention losses. A fourfold reduction of the drift volume at a distance of 2 m from the nozzle was observed for a spray with a $Dv_{50} = 225 \mu\text{m}$ when the *RSF* was reduced from 1.0 to 0.6. Under this scenario, an increase in the volumetric proportion of adhering droplets on a wheat leaf from 63 to 78% was shown. Therefore, strategies to control the droplet size distribution in terms of Dv_{50} and *RSF* may offer promising solutions for reducing adverse impacts on environment of spray applications.

Further work should be carried out on the experimental assessment of the performance of such sprays in term of drift reduction and retention on target. Sprays with a *RSF* around 0.6 and a Dv_{50} of $225 \mu\text{m}$ appear to feasible using rotary atomizers (Qi et al., 2008).

Acknowledgments

This work was supported by the Fonds De La Recherche Scientifique - FNRS, under the FRIA grant n° 97 364.

Appendix A

The mass flux is given by:

$$\dot{m} = A \frac{Sh_g D_g}{d} \rho_g (Y_{v,s} - Y_{s,\infty}) \quad (2.13)$$

with A the droplet area [m²], d the droplet diameter, Sh_g the gaseous Sherwood number [-], D_g the molecular diffusion [m s⁻²], $Y_{v,s}$ and $Y_{v,\infty}$ are the vapor mass fractions at the droplet interface and far from the droplet respectively [-]. For a diameters less than 5 mm, Sh_g can be computed as:

$$Sh_g = 1.61 + 0.718 Re^{0.5} Sc_g^{0.33} \quad (2.14)$$

with Sc_g the Schmidt number for the gaseous phase [-] expressed by: $Sc_g = \frac{\nu}{D_g}$.

The molar fraction at the droplet surface $Y_{v,s}$ is computed as:

$$Y_{v,s} = y_l^v \frac{M_l}{M_t} \quad (2.15)$$

with $y_l^v = \frac{P_{sat}}{P_{tot}}$ and $M_t = y_l^v M_l + (1 - y_l^v) M_g$. M_l and M_g are the molar mass of the liquid and the gaseous phase respectively [g mol⁻¹]. Therefore, at atmospheric pressure the vapor mass fraction at the droplet interface neighborhood, $Y_{v,s}$, reads:

$$Y_{v,s} = \frac{P_{sat}}{P_{sat} + (P_{tot} - P_{sat}) \frac{M_g}{M_l}} \quad (2.16)$$

The mass fraction in the far field is computed using the relative humidity Hr :

$$Y_{v,\infty} = Hr \frac{P_{sat}}{Hr P_{sat} + (P_{tot} - Hr P_{sat}) \left(\frac{M_g}{M_l} \right)} \quad (2.17)$$

The droplet exchanges heat with the air by convection. The heat flux between the droplet surface and the surrounding air \dot{Q}_d [J s⁻¹] reads:

$$\dot{Q}_d = S_l \frac{Nu_g \lambda_g}{d} (T_{inf} - T_l) \quad (2.18)$$

with T_l , T_{inf} the temperature of the droplet and far from the droplet interface respectively [K], λ_g the thermal conductivity of the gaseous phase [$\text{W m}^{-1} \text{K}^{-1}$]. The gaseous Nusselt number Nu_g [-] is a function of the gaseous Reynolds and the gaseous Prandlt number Pr_g [-]:

$$Nu_g = 1.61 + 0.718\sqrt{Re}^3\sqrt{Pr_g} \quad (2.19)$$

with $Pr_g = \frac{c_p \mu_g}{\lambda_g}$

The thermal balance is given by difference between the convection heat flux and the latent heat flux:

$$\dot{Q}_l = \dot{Q}_d - \dot{m}L_v \quad (2.20)$$

with L_v the vaporisation latent heat of water [J kg^{-1}] can be expressed as a function of the reduced temperature T_r :

$$L_v = 52.05310e^6 (1 - T_r)^{0.3199 - 0.212T_r + 0.25795T_r^2} \quad (2.21)$$

with $T_r = \frac{T_l + 273}{T_c}$ for water $T_c = 647.13 \text{ K}$.

The temperature at each time step is retrieved by integrate:

$$V_l \rho_l C_p \frac{\partial d T_l}{dt} = S_l \frac{Nu_g \lambda_g}{d} (T_{inf} - T_l) - L_v \dot{m} \quad (2.22)$$

C_p the heat capacity [J K^{-1}]. For water, the heat capacity is given by:

$$C_p = 276730 - 2090.1T + 8.125T^2 - 0.014116T^3 + 9.3701e^{-6}T^4 \quad (2.23)$$

Appendix B

The cumulative distribution function (CDF) of a log-normal distribution is defined as:

$$CDF = \frac{1}{x\sigma_n\sqrt{2\pi}} e^{-\frac{(\ln(x) - \mu_n)^2}{2\sigma_n^2}} \quad (2.24)$$

with σ_n and μ_n the two log-normal distribution parameters. From these parameters reduced variables can be extracted: the arithmetic mean $E = e^{\mu_n + 0.5\sigma_n^2}$ and the arithmetic variance $\text{Var} = e^{2\mu_n + 2\sigma_n^2} (e^{\sigma_n^2} - 1)$.

Chapter 3

Characterization of droplet size and speed using high-speed imaging

3.1 Preamble

In the previous chapter, the modeling of deposition and retention highlights the importance of the droplet size distribution in agricultural sprays. The experimental characterization of the droplet distribution is generally performed with optical techniques. At present, the relevance of different characterization techniques remains controversial since discrepancies may be significant between measurements performed in different laboratories. Therefore, a digital image acquisition technique and analysis algorithm has been developed for droplet size and velocimetry measurements. This chapter presents the technique and a comparison with another method the Phase Doppler Particle Analyzer (PDPA). This work has been published in a peer reviewed journal, the publication details can be found in the Table 3.1).

Table 3.1 Summary of the appended publication.

Authors:	De Cock, Nicolas and Massinon, Mathieu and Nuyttens, David and Dekeyser, Donald and Lebeau, Frédéric
Year:	2016
Title:	Measurements of reference ISO nozzles by high-speed imaging
Status:	Published
Peer reviewed:	Yes
Journal:	Crop protection
URL:	http://hdl.handle.net/2268/200879

3.2 Introduction

Droplet size and velocity distributions determine the overall treatment efficiency as they influence two specific steps of the pesticide application process, namely deposition and retention (Zabkiewicz, 2007). Deposition corresponds to the droplet transport from the nozzle to the target (weeds, insects, plant pathogens, etc.) or the amount of pesticide directed within the target area. Deposition efficiency is then defined as the ratio between the volume of droplet that reaches the target and the total volume sprayed. Deposition is optimized when the probability of a droplet to collide with the target is maximal considering the whole droplet size and velocity distributions. Physical transport of droplets (Walklate, 1987; Wang et al., 1995) and spray drift potential (Holterman et al., 1997; Lebeau et al., 2011; Teske et al., 2002) have been investigated and modeled intensively based on spray characteristics (droplet size and velocity distributions) and environmental conditions (release height, meteorological conditions, etc.) to improve deposition. Retention is the part of the deposited volume effectively retained by the plant. Its efficiency is determined by the contribution of each spray droplet during impact on the target (Massinon et al., 2015). The impact behavior depends on droplet and surface properties (Rein, 1993). Flying insect control, such as mosquitoes, requires small droplets ($\leq 50 \mu\text{m}$) for maximizing retention but are, however, airborne for a longer time than large droplets. Herbicide treatment usually involves larger droplets (200-300 μm) which are less sensitive to drift than small droplets but leading to droplet rebound and fragmentation during impact on the target. Nozzle classification according to droplet spectrum is an indicator for the most appropriated treatment for a given product and target.

The first nozzle classification was developed by the British Crop Protection Council (BCPC) in 1985. Droplet size distributions of test nozzles are compared to those of a set of reference nozzles which delimit the midpoint between five size classes, from very fine to very coarse. The classification was improved to include spray drift potential and reference classification curves were changed from midpoints to thresholds (Southcombe et al., 1998). The American Society of Agricultural Engineers (ASAE) further expanded this classification with an additional extra-coarse class for anti-drift nozzles (Hewitt et al., 1998). Inter-laboratory (round-robin) evaluations are often performed using the same set of reference nozzles to compare spray quality classification between methods (Fritz et al., 2012) and to account to the weak uniformity in the manufacturing of commercial nozzles (Womac, 2000). These measurements showed considerable differences between methods.

Aside agriculture, measurement of particle size and velocity is common in various domains including fire safety (Widmann, 2001; Zhou et al., 2012), pharmaceutical delivery (Liu et al., 2010), engine technology (Li et al., 2011), geomorphology (Kang et al., 2008), painting (Snyder et al., 1989) and food technology (Kwak et al., 2009). This resulted in many

measurement methods with different advantages and drawbacks. Most of the non-intrusive techniques are optic based, i.e., Phase Doppler Particle Analyser (PDPA), Laser Diffraction Spectrometry (LDS), imaging techniques (Shadowgraphy, PDIA). PDPA measures particle size and velocity from the light scattered by a particle moving through a measurement volume, which is defined by the interference of two focused laser beams. PDPA measurement requires liquid optical properties (refractive index) and is limited to spherical particles (Damaschke et al., 1998). LDS measures the diffraction pattern formed by the particles inside the probe volume. Droplet size distribution is found by using the complete Mie theory or the Fraunhofer approximation of the Mie theory on the recorded diffraction pattern (ISO 13320:2009). This method provides spatial measurement of particle size distribution without information on particle velocities. PDPA and diffraction methods require coherent light source from laser and dedicated electronics and optics, which induce a high cost.

Particle/Droplet Image Analysis (PDIA), usually performed in back-lighted arrangement is often referred as shadowgraphy. Particles that are significantly bigger than the light wavelength located in the probe volume, which is defined by the camera field of view and the depth of field, intercept the light and cast their shadows on the camera sensor. Particle size and centroid coordinates are determined by digital analysis of these shadows. Velocity measurement requires a tracking algorithm that identifies the same particle on two successive frames. This set-up provides spatial and temporal measurement of particles. This arrangement offers relatively low influence of particle shape and liquid optical properties on particle size and velocity measurement (Lecuona et al., 2000) and requires no delicate optic alignment. Accuracy of the particles size measurement is determined by the device's ability to correctly identify particle edges. In an ideal case, the contrast between particle and background is high and limits are easily established using the higher intensity gradient on image. Because of out-of-focus phenomena and motion blur, the contrast may be lower, inducing uncertainties and errors on particle size measurement. Motion blur can be avoided by adjusting exposure time or light pulse length depending on particle velocities. Out-of-focus effect is dealt using a parameter that expresses the focus degree of the particle according to two main approaches: the ratio between intensity gradient on particle boundary and the contrast between particle and background (Lecuona et al., 2000), or the area of the gray halo around particle shadow (Kashdan et al., 2003). Based on this parameter, the out-of-focus particles can be rejected by thresholding. The suited threshold level is chosen after determining size and focus level of known size particle at different positions around the object plane by calibration. The threshold level determines also the depth of field of the measurement volume, which is defined by the distance along the optical axis over which the uncertainty results in an acceptable error on

the measured diameter. Depth of field grows typically with the particle size (Kashdan et al., 2003).

The rapid development of imaging equipment during the last decade makes shadowgraphy an even easier to use and a cheaper alternative to scatter or diffraction based measurement methods for micro-metric particles. A digital Particle Image Velocimetry (PIV) camera combined with standard optics and pulsed Light Emitting Diodes (LED) arrays as light source provide a relatively low cost acquisition system. This multipurpose equipment can also be used for qualitative observations such as liquid sheet break-up (Cousin et al., 2012) or agricultural spray impact retention (Massinon et al., 2014; Massinon and Lebeau, 2012), what results in a very versatile tool for laboratories involved in spray application processes.

The aim of this paper is to gather recent developments in shadow image processing needed to develop an accurate, versatile and low-cost tool to characterize agricultural spray quality. The technique was evaluated with a high-speed PIV camera combined with a pulsed LED array back-light source. The developed tool was assessed by characterizing the droplet size distribution of the 6 spray quality boundaries defined by in ISO/DIS 25358 standard for the classification of droplet size spectra from atomizers. The results obtained with the imaging technique were compared with PDPA measurements.

3.3 Materials and methods

3.3.1 Experimental set-up

Shadowgraphy involved a back-lighted arrangement for image acquisition (Figure 3.1). A PIV camera (X-Stream™ XS-3, Integrated Design Tools, Tallahassee, FL, USA) coupled with high magnification optics provides a field of view of 10 mm x 12 mm at a working distance of 130 mm. The spatial resolution is equal to $9.7 \mu\text{m pixel}^{-1}$. With this magnification factor, droplets with a diameter ranging from 40 to 3500 μm can be measured. A custom made 72 W LED array (24 Luxeon III Star White) was placed 500 mm from the camera. A LED-controller (PP600F, Gardasoft Vision, Cambridge, UK) provided repeatable intensity control of the LED lighting. Possible shortest pulse length provided by the illumination system was 1 μs and was triggered by the image acquisition. Digital images were 1024 x 1280 matrices in which each value is the light intensity recorded by a camera pixel. In order to avoid motion blur a short exposure time was used (3 μs). Using the double exposure mode of the PIV camera, two consecutive images were acquired within a short time (38 μs) allowing the computation of the droplet displacements and subsequently the droplet velocities. The probe volume of this technique corresponds to the volume in which the droplets appear sharp

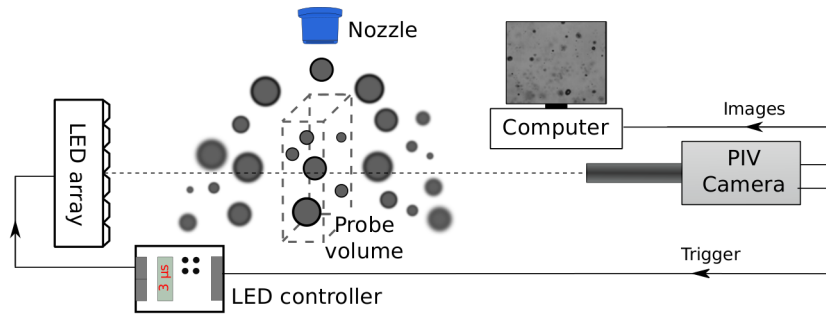


Fig. 3.1 Shadowgraphy set-up used for the image acquisitions.

enough to be measured with an acceptable error ($\leq 5\%$). A droplet has to appear in both frames of a pair of images to be taken in account. Hence the size of the probe volume is decreasing with the droplet speed. Calibrations showed that this volume is a rectangular parallelepiped with a maximum size of $10 \times 12 \times 1 \text{ mm}^3$.

3.3.2 Image processing

Figure 3.2 presents the main steps for image processing starting from the raw image. In the first step, raw image quality is improved by background subtraction (§3.3.2). As the background changes with optics alignment and camera settings, the background images have to be taken with the exact same set-up. In a second step, the image segmentation is performed in two phases. Firstly, the droplets present on the images are identified and isolated in sub-images (§3.3.2). Secondly, each droplet is individually segmented from the local background using by the Canny edge detection algorithm (Canny, 1986) (§3.3.2). Finally, the out-of-focus particles are rejected on the basis of a focus parameter in order to ensure an accurate sizing (§3.3.2).

Background subtraction

Correction for the spatial illumination heterogeneity consists of subtracting the background from each image. A composite background is then generated from the 80 percentile of each pixel intensity on a set of 50 images. Finally, after the background subtraction the image gray level is rescaled in a way that 1% of pixels are saturated (i.e. equal to 0 or 255) to maximize image contrast, independently of the acquisition conditions.

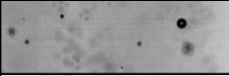
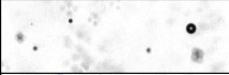
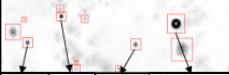
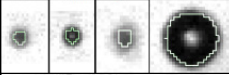

Process	Illustration
Raw image	
Background subtraction	
Droplet localization	
Droplet sizing	
Out of focus droplet rejection	

Fig. 3.2 Main steps of the droplet sizing algorithm illustrated with the example of the selection of droplets starting from a raw image.

Droplet localization

The droplet shadows present a variable gray level depending on the droplet size, degree of focus and local illumination. Consequently, there is no unique threshold adapted for an accurate segmentation of all droplets. Therefore, each droplet is analyzed individually in order to take into account the local image context. The first localization step of the droplets is achieved by computing the light intensity gradient on the whole image using Sobel's filters. The highest intensity gradients generally correspond to object boundaries. Therefore, the chosen threshold should be sufficiently low to detect all droplet boundaries, but high enough to limit the noise effect. Objects are then defined as the surface delimited by boundaries. Objects smaller than 4 pixels width and objects truncated by the edge of the image are rejected because of the weak measurement accuracy. Centroid coordinates are computed for the retained objects, which are isolated in sub-images for subsequent object sizing.

Droplet sizing

Segmentation of sub-images is realized by the Canny edge detector (Canny, 1986). This method finds object edges based on the maxima of the local gradient values. It provides a 1 pixel thin continuous response corresponding to highest values of local gradient maxima. Making the hypothesis that this response corresponds to droplet shadow boundaries, droplet size is determined by computing the inner area defined by the edge.

Out-of-focus droplet rejection

Rejection of out-of-focus particles is essential for an accurate particle sizing. Droplet degree of focus is related to the distance between the particle and the focal plane. Selection of

particles with a minimal degree of focus determines the depth of field measurement and, consequently, the sampling volume. A well-focused object exhibits a sharp transition with the background at its boundaries, while the degree of focus decreases as a droplet moves away from the focal plan and a larger gray halo appears around the object. Gradient intensity at particle boundaries increases with particle degree of focus. Based on this observation, a focus parameter adapted from the in-focus parameter of (Lecuona et al., 2000) is proposed:

$$\text{Focus parameter} = \frac{\text{grad}_{\text{bound}}}{I_{\text{object}} - I_{\text{back}}} \quad (3.1)$$

where $\text{grad}_{\text{bound}}$ is the intensity gradient value on the object boundaries, I_{object} and I_{back} are gray levels of the object and the background, respectively. To avoid effect of noise or the bright spot caused by light scattering, these last values are obtained with a rank order filter such as median value. This focus parameter is less sensitive to local illumination variations since it is based on the contrast between the object and the local background. Thresholds for focused particle selection were determined by studying the evolution of the focus parameter and the error on particle size measurement from images containing uniform droplets with a known size at various distance of the object plane. This was achieved using a custom-made droplet generator that produces a continuous stream of equally spaced and mono-sized droplets. The generator produce a round jet which is broken into droplets by stimulating the Plateau-Rayleigh instability at an optimal frequency by mechanical vibrations (Sirignano and Mehring, 2000). Five glass nozzles producing droplets of 111, 157, 208, 351 and 516 μm were used. The droplet diameters at optimal perturbation frequency were calculated by the following equation:

$$d = \sqrt[3]{\frac{6Q}{\pi f}} \quad (3.2)$$

where d is the droplet diameter [m], Q is the flow rate measured by bucket method [$\text{m}^3 \text{s}^{-1}$] and f is the perturbation frequency [Hz]. The stream of droplets was shoot with an oblique direction in respect to the focal plane. Examples of oblique droplet streams are presented in the Figure 3.3a. By recording around hundred pictures, a continuous expression of the focus parameter and the relative error on the droplet size measurements could be expressed in respect to the focal plane distance (Figures 3.3b and c). Thresholds of the focus parameter were then chosen to have both an error less than 5% on size measurement and a depth of field as large as possible. Figure 3.4 shows the relation between the depth of field and the droplet diameter. A threshold of the focus parameter equal to 0.23 was chosen giving the following linear relationship between the depth of field (DOF) and the droplet diameter (d)

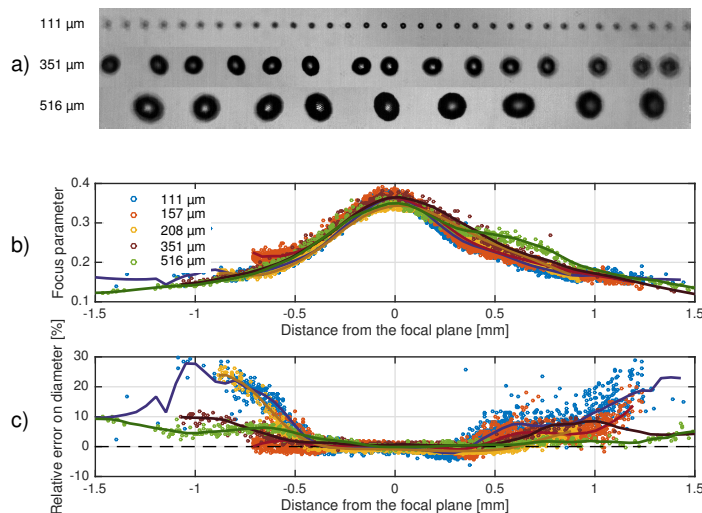


Fig. 3.3 Oblique shoot of 111, 351 and 516 μm droplet streams (a). Focus parameter (b) and relative error on the diameter measurement (c) in respect to the distance from the focal plane.

(both expressed in m):

$$DOF = 0.85d + 0.00078 \quad (3.3)$$

3.3.3 Particle tracking velocimetry (PTV)

Particles are tracked between image pairs for velocity computing. Several criteria are required to find the same droplet on two successive frames with a high level of confidence. The most evident criterion is the conservation of diameter. The second is the displacement expected between two frames. In an agricultural spray the mean droplet direction is known, providing a hypothetical localization of a droplet on the second exposure. The search area on the second frame was defined as a circular sector oriented along the mean flow direction (Figure 3.5). The opening angle θ is defined by the maximum angle between the main flow direction and a particle displacement, depending on radial dispersion intensity. Maximal displacement of a particle between two frames is determined according to the delay between the two exposures and a maximal velocity assumption for the spray:

$$D_{max} = v_{max} \Delta t \quad (3.4)$$

where D_{max} is the maximal displacement [m], v_{max} is the maximal velocity [m s^{-1}] and Δt is the time between the two exposures [s]. The values chosen for the displacement and the distance criteria define the measurement confidence. Too permissive criteria provide

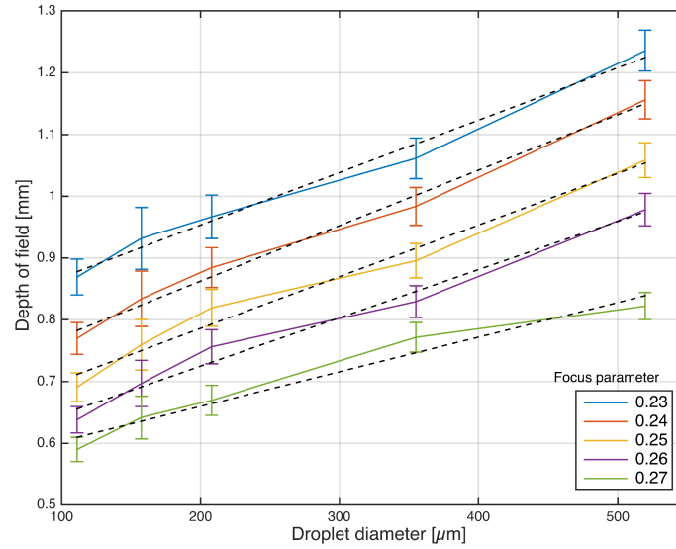


Fig. 3.4 Depth of field for the different droplet diameters according to the focus parameter. The dashed lines correspond to linear regressions.

mismatching and finally error in computed velocity. Inversely, too restrictive criteria limit the pair matching and result in a misleading velocity measurement. These errors can be removed by post processing or by adjusting the maximum displacement to the droplet diameter according to an iterative procedure thanks to the high velocity-size correlation into sprays (Lefebvre, 1988).

3.3.4 Droplet size distribution

Droplets do not have an equal probability to be measured due to the volumetric sampling method. Sampling probability is depending both on the size of the probe volume and on the residence time of the droplets into this volume, which depends on droplet velocity and size. A slow droplet remains longer in the probe volume and in turn is more likely to be recorded on the subsequent frame than a fast droplet.

Furthermore, the larger the droplet, the higher the probability to touch the image edges and to be rejected during the object localisation step. Droplet size distribution is established by weighting the volumetric contribution of the accepted droplets by a correcting factor (CF), which is defined as follows:

$$CF = \frac{v}{FOV_{cor} DOF} \quad (3.5)$$

where v is the droplet velocity [m s^{-1}], DOF is the optical set-up depth of field [m] expressed by equation 3.3 in respect to the droplet diameter and FOV_{cor} is the corrected camera field of view [m^2], which is the image area in which a droplet must occur in the first acquisition to be

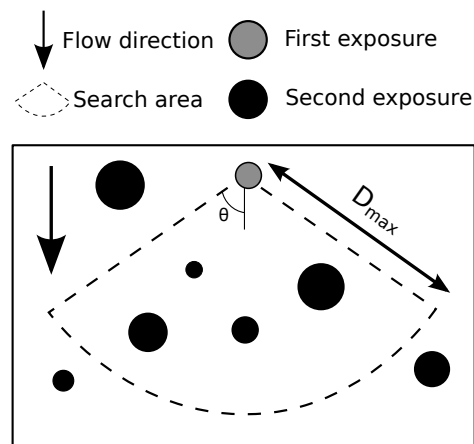


Fig. 3.5 Droplet tracking principle using a search area based on the size conservation of the droplet and a priori knowledge of the flow direction in order to retrieve the same droplet on two successive frames.

measured (Figure 3.6) and is determined as follows:

$$FOV_{cor} = [(l - d) - (v\Delta t)](L - d) \quad (3.6)$$

where L and l are the length and the width of the image respectively [m], d is the droplet diameter [m] and Δt is the time between two exposures [s]. It is assumed that the vertical component of the droplet velocity is much larger than the horizontal one, which means that the algorithm does not take into account the possible exit of a droplet from the side of the image.

3.3.5 Image processing implementation

Matlab R2013a with image processing toolbox was chosen as technical computing language to implement the above image processing and analysis. The Matlab routines are available with an example at the permanent URL: <http://hdl.handle.net/2268/150929>.

3.3.6 Reference nozzles-pressure combinations

Spray characterization was performed on a set of reference nozzles using the imaging technique and compared with the PDPA laser technique. Six stainless steel flat fan nozzles (Sprayings Systems Co., Wheaton, USA) are currently used in round-robin tests in the framework of the ISO/DIS 25358 "Crop protection equipment - Droplet-size spectra from atomizers - Measurement and classification", to define boundaries for nozzle classification: Very Fine (*VF*), Fine (*F*), Medium (*M*), Coarse (*C*), Very Coarse (*VC*), Ultra Coarse (*UC*)

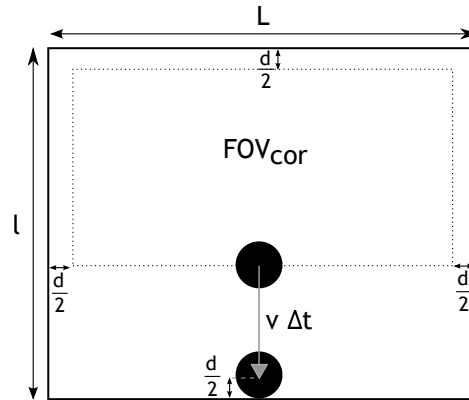


Fig. 3.6 Illustration of the corrected field of view (FOV_{cor}) in dashed line which is defined as the area on the first image wherein the droplet center must be located in order to be measured. To be measured a droplet cannot be cropped by the image edge and has to fully appear on the second image.

Table 3.2 Combination of nozzle and pressure defining the different spray class boundaries with the respective nominal flow rate.

Spray class boundary	Nozzle	Pressure [bar]	Nominal flow rate [$\ell \text{ min}^{-1}$]
<i>VF/F</i>	Teejet TP 110 01	4.5	0.48
<i>F/M</i>	Teejet TP 110 03	3	1.18
<i>M/C</i>	Teejet TP 110 06	2.5	2.16
<i>C/VC</i>	Teejet TP 80 08	2.5	2.88
<i>VC/UC</i>	Teejet TP 65 10	1.5	2.80
<i>UC/XC</i>	Teejet TP 65 15	1.5	4.18

and Extremely Coarse (*XC*). The six nozzle/pressure combinations are presented in Table 3.2. Tap water was used as liquid and the spray pressure was set with a maximum relative error of 3 %.

3.3.7 Measuring protocol

Imaging technique

For the imaging technique, the measurements were realized 0.5 m below the nozzle and covered $1/4^{th}$ of the whole spray assuming the spray to be symmetrical (Figure 3.7). The scan of the spray was realized by recordings 1500 pair of images per line on 8 lines of 0.85 m spaced by 0.001 m. During the recording of the images, the nozzle was moving at 0.0425 m s^{-1} along the spray major axis. Finally, the droplet size distribution was retrieved by gathering the data from each scanning line. For the coarser nozzle-pressure combination

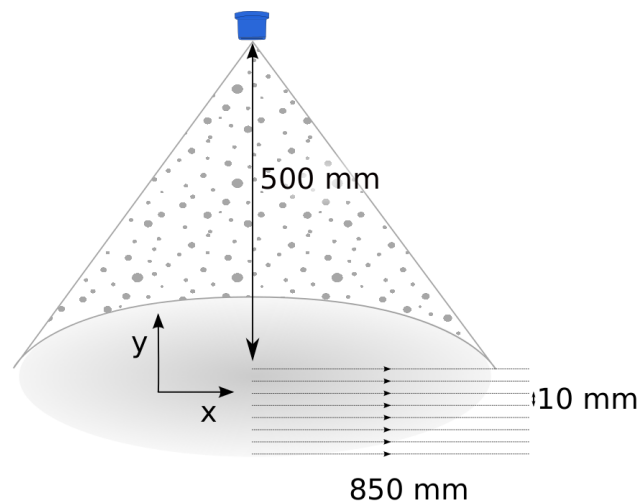


Fig. 3.7 Scanning pattern used for the characterization of the sprays.

(UC/XC), 2250 pairs of images per line have been taken in order to have sufficient amount of droplets.

PDPA

A TSI/Aerometrics PowerSight solid state laser-based PDPA system was used (Nuyttens et al., 2007a). The system comprises an Argon-Ion laser, a fiber-optic transmitter and receiver, a signal analyzer, and FlowSizer-software. By means of the fiber-optic transmitter the laser beams are focused to cross over at a distance equal to the focal length (500 mm) of the transmitter lens. The sampling area is formed by the intersecting beams and has the shape of an ellipsoid. When a droplet passes the sampling area, the laser light is scattered. The fiber-optic receiver collects the scattered laser light. The light is directed by a prism pack to three photomultiplier tubes (PMT's) which convert the light signals into electrical signals to be processed for velocity and size information by the signal analyzer. Each PMT produces a signal with a frequency proportional to the particle velocity taken perpendicularly to the sampling area. Therefore, the measured velocity corresponds to the vertical component of the droplet velocity. The phase shift between the signals from two different PMT's is proportional to the size of the spherical particles. Measurement ranges for velocity and diameter can be changed through variations in the optical equipment, laser beam separation, and lens focal lengths of the transmitting and receiving optics. Settings on the instrument were chosen to cover a size range of 3 to 1113 μm . A cross-section average sample was obtained across the spray plume at 0.5 m distances from the nozzle outlet by moving the nozzle on a scan pattern. For the PDPA measurements, the full spray pattern was sampled by scanning 9 lines. In general, a different scan trajectory was programmed depending on

Table 3.3 Number of droplets measured and rejected with both technique for each nozzle-pressure combinations.

	Number of measured droplets		Relative number of rejected droplets [%]	
	Imaging	PDPA	Imaging	PDPA
VF/F	96 918	75 205	10.2	5.1
F/M	47 322	79 191	9.1	2.9
M/C	40 720	77 909	9.2	3.8
C/VC	35 573	85 630	14.9	4.5
VC/UC	15 998	69 821	9.0	6.8
UC/XC	20 682	55 095	8.5	4.1

the type of nozzle. Scanning speed was set that each scan yielded data for at least 10 000 droplets with the PDPA.

3.4 Results and discussion

3.4.1 Droplet measurement

The post processing of the 12 000 pairs of images per nozzle-pressure combination took in average 100 minutes. Matlab R2013a was used on a desktop computer with a processor Intel i7-4930k and 16 Go of ram. The table 3.3 presents the number of droplets for each nozzle-pressure combinations. For the imaging technique, 15 000 to 95 000 droplets were recorded at the end of the whole scan. In order to have more than 15 000 droplets, extra videos have been recorded for the *UC/XC* spray. For the PDPA, from 50 000 up to 85 000 droplets were measured during the scanning process. The rejected droplets for the imaging correspond to the droplets detected on the first frame which couldn't be track on the second frame. The rejected droplets for the PDPA are due to three reasons. Firstly, there is a size-intensity validation, a certain droplet size should have a certain range of intensity of the scattered light. Secondly, extreme values are rejected by putting some ranges (this is rejecting only 1 or a few droplets per scan). Thirdly, only droplets where we have values for size and velocity are kept. PDPA presents lower amount of rejected droplets, however rejection arise from different origin so it's difficult to compare.

The spatial distribution of the accepted and the rejected droplets for the imaging technique can be displayed over the field of view. The figure 3.8 aggregated the accepted and the rejected droplets from all the nozzle-pressure combinations measurements. Each pixel of the figure corresponds to a square of $500 \mu\text{m} \times 500 \mu\text{m}$ on the field of view. The accepted droplets

are quite uniformly distributed, except on the sides of the field of view where less droplets have been measured because in this area the droplets are more prone to exit the field of view on the second frame or to be cropped by the image border. A large volume of the rejected droplets (65 %) is located in the lower 1 mm of the field of view. Since the droplets are crossing the field of view from the top to the bottom, this high rejection rate is due to the exit of the droplet from the field of view between the first and the second frame. The droplet rejected on the sides of the field of view (1 mm from the side and neglecting the lower 1 mm) represent 9.4 % of the overall rejected volume. There is a higher droplet rejection (5.4 %) on the right side of the field view than on the left side (4 %). This dissymmetry is explained by the fact that only the right half side of the spray triangle is scanned. Therefore, it corresponds to the droplet on the edge of the spray which have a higher horizontal velocity. The exit of the field of view by the droplets are mainly occurring at the bottom side as supposed by the field of view correction which has been proposed in §3.3.4. The other rejected droplets may come from droplet merging, exit of the probe volume by the third axis or fail of the image processing on the first or second frame.

3.4.2 Effect of the correcting factor

The figure 3.9a presents the relative number of measured droplet in respect to the droplet diameter with both techniques. Only the F/M case is showed since the six cases presented similar trends. The results of the imaging technique are presented before and after the correction of the sampling inhomogeneity detailed in the section §3.3.4. The correction decreases the peak located around $75 \mu\text{m}$ and increases the proportion of droplets larger than $150 \mu\text{m}$. The figure 3.9b shows the relative cumulative volume in respect to the droplet diameter. On this representation, the coarsening effect of the correction is highlighted. With the correction the imaging results are closer to the PDPA data. An example of the relative variation of each component of the correcting factor according to the droplet diameter is presented on the figure 3.10. The depth of field and the correction of the field of view have a low range of variation equal to 1.54 and 1.15 respectively whilst the velocity has a range of variation of 7. This shows the preponderance of the velocity in the value of the correction factor. Since the velocity is increasing with the diameter, the correction is increasing the relative proportion of large droplets.

3.4.3 Droplet size distribution

Figure 3.11 compares the cumulative volumetric droplet size distribution between the PDPA and the imaging technique for the 6 reference nozzle-pressure combinations. Concerning

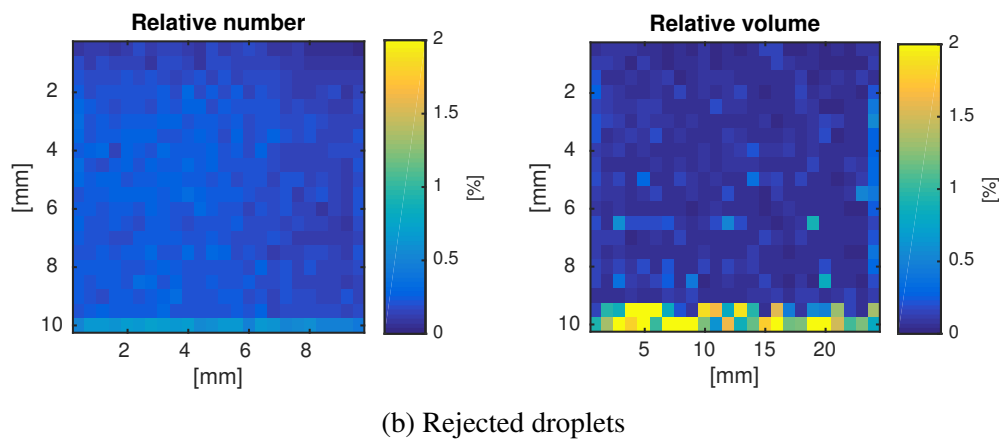
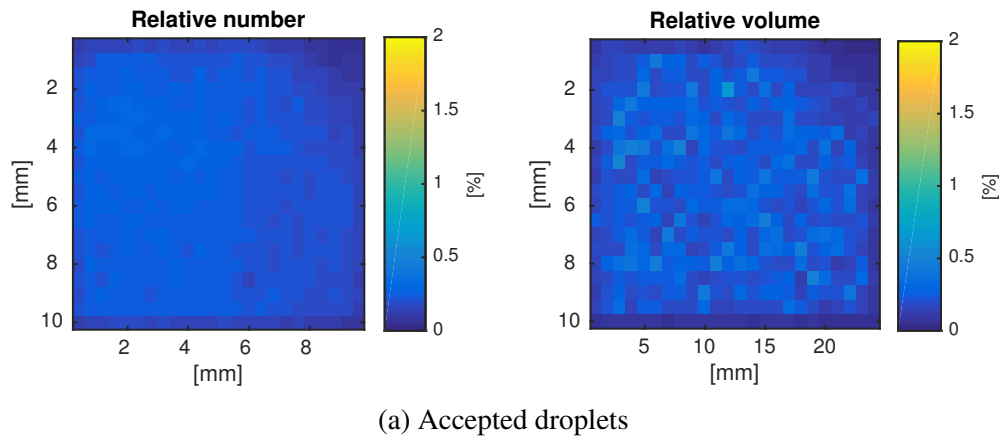


Fig. 3.8 Spatial distribution of the rejected and the accepted droplets on the field of view. The droplets from all the imaging measurements have been used to build this spatial distribution.

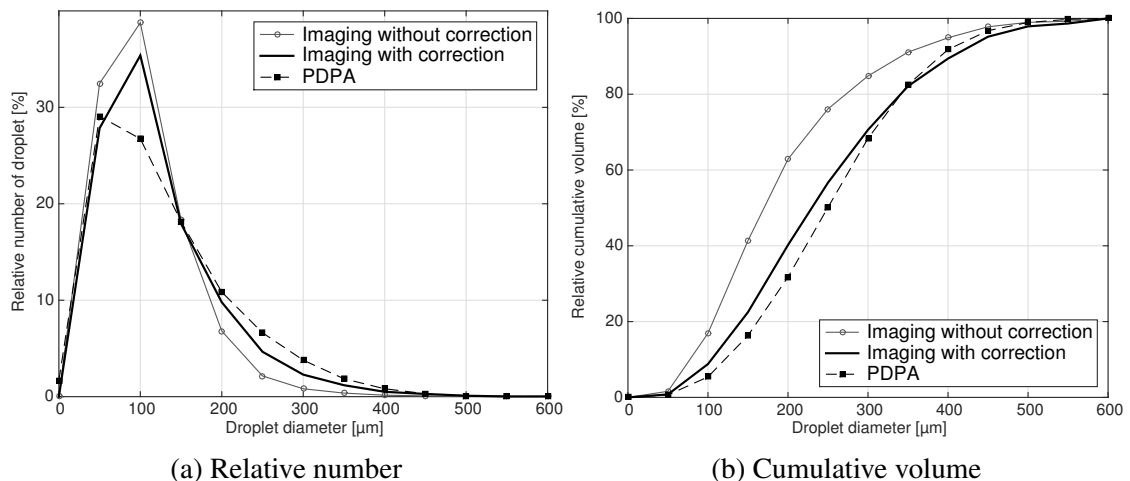


Fig. 3.9 Relative number of droplet and relative cumulative volume in respect to the droplet diameter for both techniques for the F/M case. The imaging results are given before and after the correction of the sampling inhomogeneity.

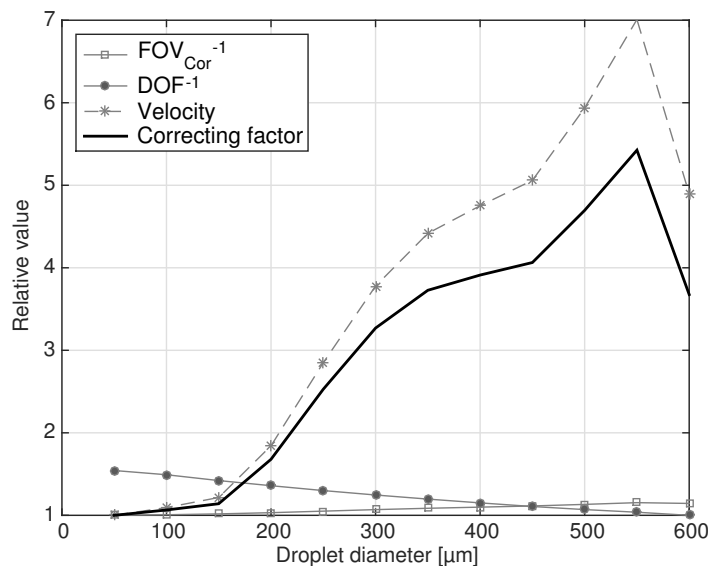


Fig. 3.10 Relative value of the different correcting factors in respect to the droplet diameter for the F/M case.

the imaging technique, the 6 droplet size distributions are well differentiated showing that the imaging technique is able to measure small and coarse droplets with the same set-up. The smallest measured droplet had a diameter of $40 \mu\text{m}$ and the largest droplet had a diameter of $1300 \mu\text{m}$. The coarser sprays present less smooth curves because of the lower number of droplets recorded. The comparison between imaging technique and PDPA measurement provides some general trends. For the finest sprays (VF/F and F/M), both techniques measured similar droplet size distributions. Whilst for the coarser sprays, there is a significant difference: for the M/C and C/VC sprays, the imaging technique measured a finer droplet size distribution and for the VC/XC and XC/UC sprays the imaging technique measured coarser droplet size distribution.

The Figure 3.12 compares the measurements of Dv_{10} , Dv_{50} and Dv_{90} obtained with both techniques. Dv_{10} , Dv_{50} and Dv_{90} are corresponding to the maximum particle diameter below which 10%, 50% and 90% of the sample volume exists, respectively. For all the sprays, the imaging technique gave a lower Dv_{10} than the PDPA. The difference between both measurements is roughly increasing with the droplet size spectrum. This observation is surprising since the imaging technique does not take into account the droplets smaller than $40 \mu\text{m}$, so it was expected to overestimate the Dv_{10} . The Dv_{50} measurements were quite similar between both techniques except for the M/C case for which the difference is significant ($62 \mu\text{m}$). The error bars show the standard error on the average. This error has been computed by considering the three scans as independent. The error is low for the most of the cases, except for the Dv_{90} measurements of the coarse nozzle with the imaging technique.

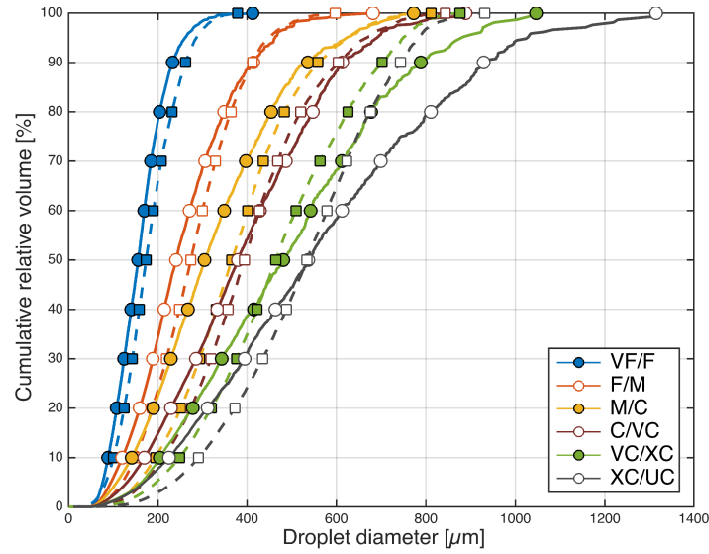


Fig. 3.11 Cumulative volumetric droplet size distribution for the 6 spray class boundaries. Imaging technique and PDPA are represented by the circle with full lines and the square with the dashed lines respectively.

Table 3.4 Average, standard deviation and coefficient of variation of the difference between following spray class boundary.

	ΔDv_{10}			ΔDv_{50}			ΔDv_{90}		
	Avg	Std	CV	Avg	Std	CV	Avg	Std	CV
	[μm]	[μm]	[%]	[μm]	[μm]	[%]	[μm]	[μm]	[%]
Imaging	27.3	6.1	22.3	76.5	18.1	23.7	139.6	43.1	30.1
PDPA	38.2	12.2	31.9	72.4	28.4	39.2	96.0	53.3	55.5

This relatively high error can be explained by the low amount of large droplet recorded because of their lower presence and their lower sampling probability with the imaging technique. The Dv_{90} comparison shows large discrepancies for the coarser sprays (VC/UC and UC/XC). In these coarse sprays, the imaging technique recorded large (≥ 1 mm) and fast (≥ 13 m s⁻¹) droplets which have a significant contribution on the final volumetric droplet size distribution. These droplets may not have been detected by the PDPA system because their diameter exceeded the maximum detectable diameter or because of their non sphericity. Table 3.4 presents the average and the standard deviation of the difference in term of Dv_{10} , Dv_{50} and Dv_{90} between two neighboring spray classes i.e. $\Delta Dv_{10i} = (Dv_{10i+1} - Dv_{10i})$. Imaging technique presents a higher spacing uniformity between each reference spray.

Table 3.5 presents for each technique the measured relative span factor (RSF) computed as: $RSF = (Dv_{90} - Dv_{10}) / Dv_{50}$. For most of the sprays, the imaging technique presents a larger value of RSF with RSF values of 1.2 to 1.3 whilst PDPA measured almost constant RSF

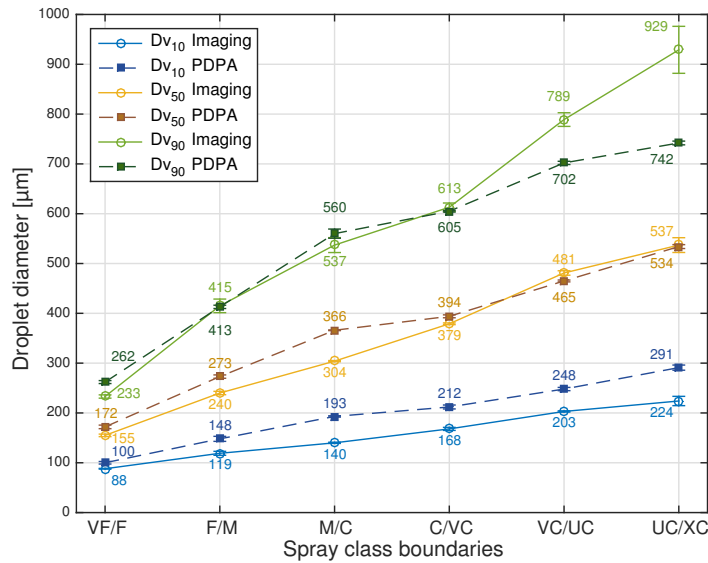


Fig. 3.12 Dv_{10} , Dv_{50} and Dv_{90} [μm] for the 6 reference sprays. Imaging technique and PDPA are represented by full lines with circles and the dashed lines with squares respectively.

Table 3.5 Relative span factor measured for each spray class boundaries for PDPA and imaging technique.

	VF/F	F/M	M/C	C/VC	VC/UC	UC/XC
Imaging	0.94	1.22	1.31	1.18	1.22	1.31
PDPA	0.94	0.97	1.00	1.00	0.98	0.85

ranging around 1. For the coarsest spray, PDPA measured a surprisingly low value of RSF which may be explained by the difficulty of the PDPA to measure coarse droplet leading to an underestimation of the Dv_{90} .

3.4.4 Droplet velocity distribution

In the present section, the comparisons are realized for the droplet vertical velocity since it's the only velocity component measured by the PDPA. The figure 3.13 shows the average velocity measured according to the droplet diameter class for both techniques. The average velocity has been computed with diameter classes of $50 \mu\text{m}$ for bins having at least 25 droplets. Discrepancies between both techniques mainly appears for larger droplets. The source of these differences may be a combination of an error on size and velocity measurement, a too small sample or a difference in the operating conditions.

The figure 3.14 shows the cumulative volumetric droplet velocity distribution for the 6 different nozzle-pressure combinations. The droplet velocity is ranging from 0 to 20 m s^{-1} . For the finer sprays, the velocity is increasing with the droplet size. The highest speeds were

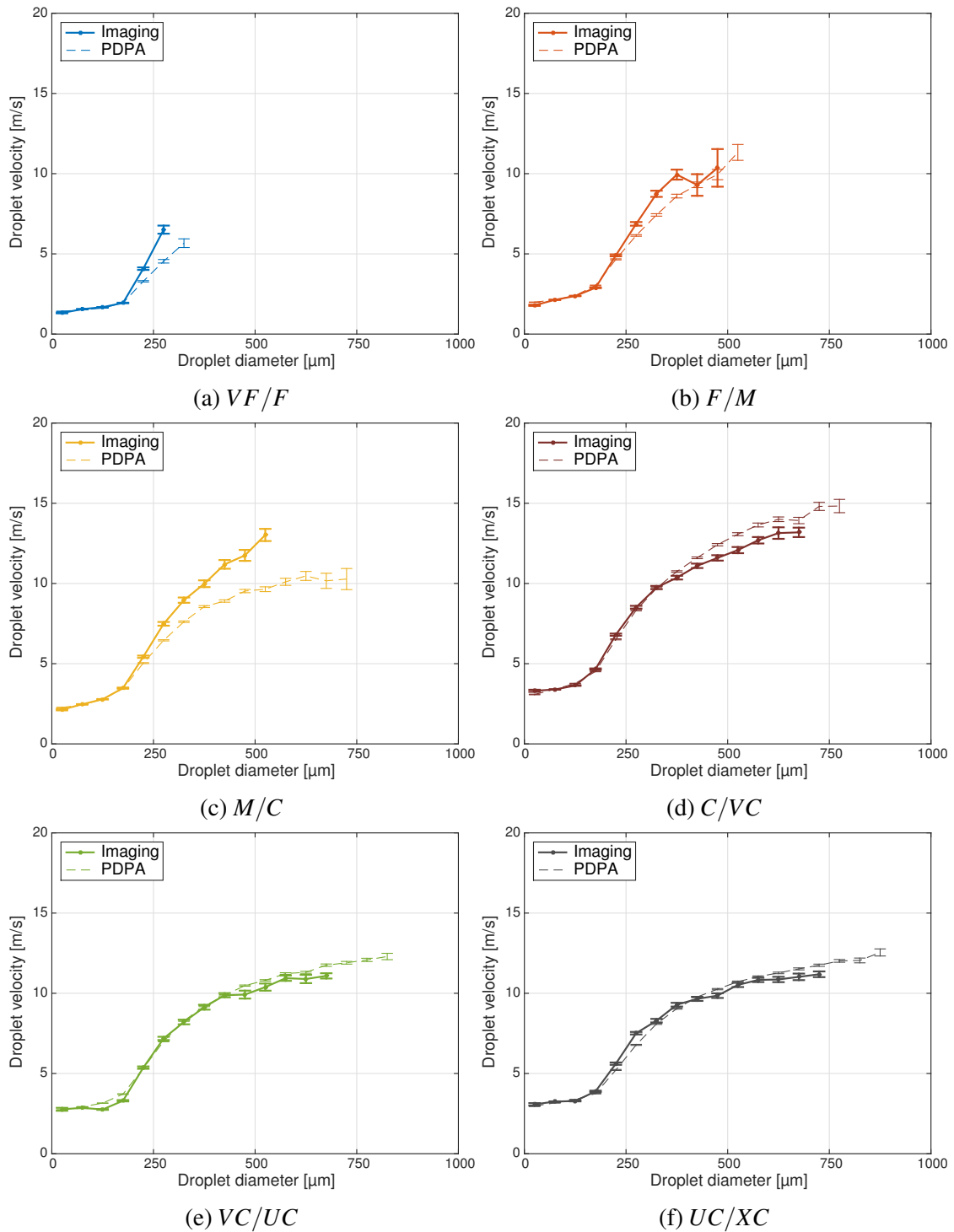


Fig. 3.13 Average velocity measured per diameter class of $50 \mu\text{m}$ with both techniques. The error bars indicate the standard error on the mean.

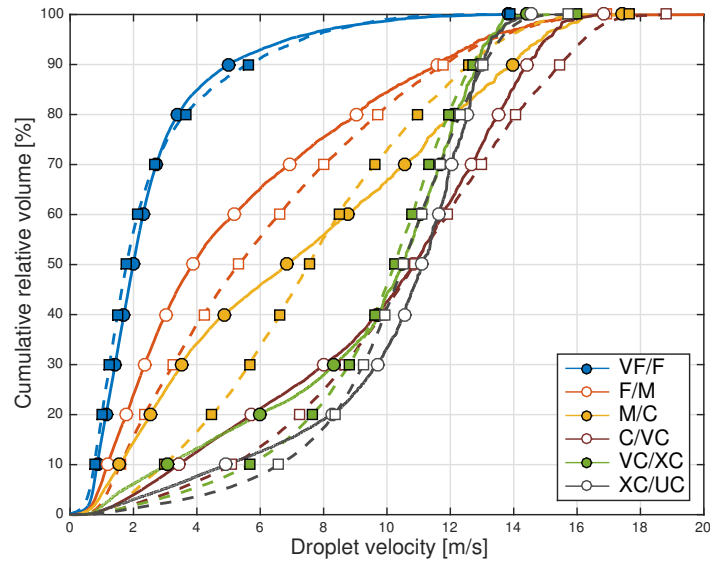


Fig. 3.14 Cumulative volumetric droplet velocity distribution for the 6 different nozzle-pressure combinations. Imaging technique and PDPA are represented by the circle with full lines and the square with the dashed lines respectively.

found for the C/VC nozzle-pressure combination. This high speed may justify the relatively higher percentage of rejected droplets observed for this nozzle-pressure combination with the imaging technique. The differences observed between both techniques mainly arise from the difference in term of droplet size measurements since the size/velocity behavior is similar with both technique.

3.5 Conclusion

A digital image acquisition technique and analysis algorithm was proposed for droplet size and velocimetry measurements. The image acquisition set-up and the image processing method has been detailed. The droplet size distributions of a set of reference sprays defined in the ISO/DIS 25358 were measured using the proposed imaging technique and a PDPA laser. Concerning the imaging technique, the 6 sprays droplet size distributions were differentiated well. The smallest droplet measured had a diameter of $40\ \mu\text{m}$ and the largest droplet measured had a diameter of $1300\ \mu\text{m}$. The comparison between imaging technique and PDPA measurement provided some global trends. For the finest spray (VF/F), both techniques measured a similar droplet size distributions. Whilst for the coarser sprays, there is a significant difference: for the F/M and M/C sprays, the imaging measured a finer droplet size distribution and for the C/VC , VC/XC and XC/UC sprays the imaging technique measured coarser droplet size distribution. PDPA measurements tend to measure an equivalent Dv_{50} , a

higher Dv_{10} and a lower Dv_{90} than the imaging technique leading therefore to a lower relative span factor. Velocity measurements showed good agreement between both techniques except for one nozzle/pressure combination. Therefore, comparison of two measurements realized with each method should be realized carefully knowing these differences. The Dv_{50} seems to be the best parameter for comparisons since both techniques provide similar value.

3.6 Acknowledgments

This work was supported by the Fonds de la Recherche Scientifique - FNRS under the FRIA grant n° 97364.

Chapter 4

Numerical modelling of the effect of a splash plate nozzle inlet shape

4.1 Preamble

The development of an analytical model of the flow on the nozzle plate has been realized using Computational Fluid Dynamics simulations using a volume of fluid model. The development of the model is presented in the next chapter. The present chapter introduces the numerical model and assess its capability to simulate the spreading of a liquid sheet on a solid surface. The following work has been presented in the ASABE meeting 2014, details can be found in the Table 4.1. The paper has been partly modified in order to improve its clarity.

Table 4.1 Summary of the appended publication.

Authors:	De Cock, Nicolas and Massinon, Mathieu and Mercatoris, Benoit and Lebeau, Frédéric
Year:	2014
Title:	Numerical modelling of mirror nozzle flow
Status:	Conference proceeding
Peer reviewed:	No
Event name:	Asabe meeting 2014
URL:	http://hdl.handle.net/2268/169750

4.2 Introduction

The use of plant protection products is required to satisfy the demand for high quality and high production of agricultural products. Typically liquid sprays are applied to the growing plants at different growth stages. These protect the crops from pest and disease damage to provide increased yield and quality. This is achieved by atomizing the agricultural spray mixture through a nozzle to generate a cloud of droplets. It has been proven that droplet size not only has a significant effect on the global deposition process efficiency (Matthews, 2008) but also, smaller droplets have a higher drift potential (Taylor et al., 2004) leading to potential product losses to the air, water and soil (Reichenberger et al., 2007). Larger droplets, with a higher kinetic energy, are more prone to shatter while which may reduce the plant retention efficiency (Massinon and Lebeau, 2012). The droplet sizes and their speeds in a spray cloud result from the interactions between the physical properties of the liquid, the nozzle operating conditions and the nozzle geometry (Miller and Butler Ellis, 2000). During the past decades, there have been multiple researches on the effect of the liquid physical properties (Butler Ellis et al., 1997, 2001; Holloway et al., 2000) as well as the nozzle type (Nuyttens et al., 2007a). However, to our knowledge, few specific works focused on the relationship between nozzle geometry parameters and the spray produced. The numerical studies realized on black liquor nozzles provided promising results for nozzle design (Fard et al., 2007). The present effort is the first step of a work which aims at optimizing the design of a splash plate nozzle producing a spray with a narrow drop size distribution, in order to increase the agricultural spray application efficiency. Splash plate nozzles, which generate sprays by the impact of a liquid jet onto a solid surface, have a low susceptibility to clogging and a high customization potential. The plate of the nozzle will end with structure splitting the liquid sheet into multiple jets. Here, emphasis is put on the liquid flow homogeneity on the plate which is a prerequisite for the production of jets with uniform properties. This chapter is divided into three parts. The first part is dedicated to the description of the numerical model used for the simulations. The second part is the assessment of the OpenFoam multiphase solver by computing the impact of a round liquid jet on a horizontal solid surface. This flow has an analytical solution proposed by Watson (1964). The third part presents a study of pipe shape and inlet flow rate effects on the flow homogeneity on the plate.

0.95	0.8	0.35	0.05	0
1	1	1	0.6	0.05
1	1	1	1	0.35
1	1	1	1	0.8

Fig. 4.1 Example of C field, the blue shape indicates the real liquid contour.

4.3 Materials and methods

4.3.1 Numerical model

The InterFoam solver from the OpenFoam C++ toolbox has been used which is a Volume Of Fluid (VOF) solver for incompressible two-phase flow. The VOF method is used to track and locate the liquid-air interface. It requires an Eulerian grid and the use of an additional variable, C . This extra variable defines the liquid fraction inside each cell; its value is equal to 1 for a cell full of water and 0 for the cell with air, and values range between 0 and 1 while the cell is located at the interface (Figure 4.1). The Figure 4.1 presents an example of distribution of C at a liquid-gas interface. Then, the interface location is retrieved based on the liquid fraction distribution. This implicit interface capturing method is less accurate than explicit method as level-set but it has the advantage to be mass conservative (Deshpande et al., 2012).

Here, all the cases are considered as in a laminar mode. Therefore, no extra turbulence model has been used. The main equations solved are detailed below, more details about this solver can be found in the paper of Deshpande et al. (2012). The mass conservation for incompressible flow is given by:

$$\nabla \cdot U = 0 \quad (4.1)$$

where U is the velocity [m s^{-1}]. The liquid fraction transport equation is:

$$\frac{\partial C}{\partial t} + \nabla \cdot (UC) = 0 \quad (4.2)$$

where C is the liquid fraction [-] and the momentum conservation equation consists of:

$$\frac{\partial \rho U}{\partial t} + \nabla \cdot (\rho U U) - \mu \Delta U - \rho g - F_{ST} + \nabla p = 0 \quad (4.3)$$

where ρ is the density [kg m^{-3}], t is the time [s], ν is the dynamic viscosity [Pa s], g is the gravity [m s^{-2}], F_{ST} is the surface tension force per unit of volume [N m^{-3}] and p is

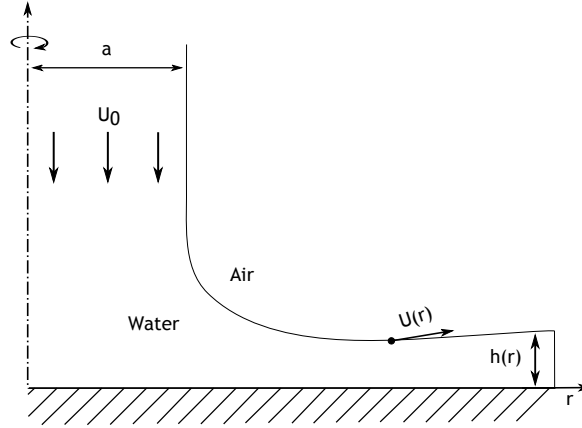


Fig. 4.2 Flow illustration, where a is the jet radius [m], U_0 is the initial velocity [m s^{-1}], h the water thickness [m], U the velocity magnitude at the water/air interface [m s^{-1}] and r the distance to the jet center [m].

the pressure [Pa]. The density and the viscosity are computed by weighting the two fluid properties by the liquid fraction as follows

$$\rho = \sum \rho_i C_i \quad (4.4)$$

$$\mu = \sum \mu_i C_i \quad (4.5)$$

4.3.2 Validation case

Flow description

The case studied is the flow created by the impact of a round water jet onto an infinite smooth solid surface (Figure 4.2). This two-phase flow is similar to the flow developing on the plate of a splash plate nozzle flow. The flow is axi-symmetric, with the liquid sheet height h and the surface velocity U are related to the initial jet characteristics and the radial distance r from the jet center. Watson (1964) used the boundary-layer theory to provide an analytical solution for the free surface height and velocity depending on the jet center distance. The equations of Watson's model are fully detailed in the next chapter. This reference case will be used to assess the capability of the solver to provide a realistic solution for this type of flow.

For the present study, the initial jet velocity U_0 and the jet radius a are fixed at 3 m s^{-1} and 0.4 mm respectively. The jet Reynolds number is computed as follows:

$$Re = \frac{Q}{\nu a} \quad (4.6)$$

where Q is the volumetric flow rate [$\text{m}^3 \text{s}^{-1}$] and ν is the kinematic viscosity [$\text{m}^2 \text{s}^{-1}$]. This number is therefore around 1200. Q can be expressed based on the jet radius and the jet velocity

$$Q = U_0 \pi d^2 \quad (4.7)$$

Numerical parameters

The flow is simulated using an axi-symmetric domain which has a wedge shape in OpenFOAM. Axi-symmetric simulation uses a 2-D mesh which allows reduction of the computational time compared to a 3-D simulations. The domain dimensions and the associated boundary conditions are detailed in Figure 4.3. A second order central difference scheme has been used.

Boundary conditions: Inlet: fixed velocity: $U = (0, -3, 0)$ and fixed liquid fraction: $C=1$. Walls: no slip condition. Outlet: fixed pressure: $p = p_{atm}$ Wedge: OpenFoam boundary conditions for the front and back plan of an axisymmetric mesh.

The mesh generated by the blockMesh utility of OpenFoam is made of hexahedral cells, apart from the cells close to the axis of symmetry which are prismatic, of uniform size. Three mesh refinements have been tested, characteristics of which are presented in Table 4.2. The grid spacing has been set finer for the y direction which presents a higher velocity gradient due to boundary layer development. The simulations have been performed on a desktop computer with a processor Intel i7-4930k and 16 Go of ram. A grid convergence study has been realized and is shown in the appendix A.

Table 4.2 Mesh characteristics for the three cases studied.

Case	Number of cells				Grid spacing	
	X	Y	Z	Total	X	Y
Coarse	100	40	1	4 000	80	40
Normal	200	80	1	16 000	40	20
Fine	400	160	1	64 000	20	10

4.3.3 Splash plate nozzle

Flow description

The splash plate nozzle geometry can be simplified as a pipe ending perpendicularly on a horizontal disk. The pipe is a circular segment with an opening of 140° or 180° for the

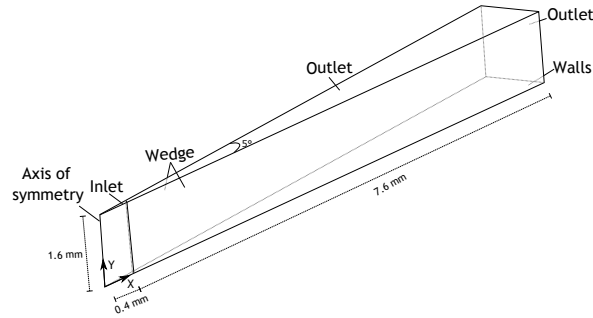


Fig. 4.3 Numerical domain of the test case with the associated boundary conditions. The domain is as a wedge shape corresponding to OpenFOAM axisymmetric case.

Table 4.3 Summary of the numerical simulations parameters.

Case	Geometry	Flow rate [$\ell \text{ min}^{-1}$]	Inlet velocity [m s^{-1}]
1	180°	0.5	1.05
2	180°	1	2.1
3	180°	2	4.2
4	140°	0.5	1.35
5	140°	1	2.7
6	140°	2	5.4

geometry 1 or 2 respectively. For both geometries, three flow rates are tested: 0.5, 1 and 2 $\ell \text{ min}^{-1}$ (Table 4.3). The flow will create a liquid sheet on the plate. The goal of the splash plate nozzle design is to obtain at the edge of the plate a homogeneous liquid sheet making an angle of $\sim 140^\circ$. Over 140° , there is a gap of 0.3 mm between the plate and the pipe. This opening guides the flow parallel to the plate. The effect of two different inlet geometries were tested on the downstream flow homogeneity at various flow rate is assessed.

Numerical simulations

The Figure 4.4 presents the numerical domain for the geometry 1 with the boundary conditions used for all the cases. 3-D meshed have been used. All the simulations were ran as unsteady with the InterFoam solver. At the beginning of the simulations, the flow presents a transient phase during which the plate is progressively wet as shown in Figure 4.5. The duration of this phase ranges from 10-40 ms according to the initial flow rate in the pipe. This phase is followed by an almost steady phase. The example presented has the time average of the numerical solution during the steady phase.

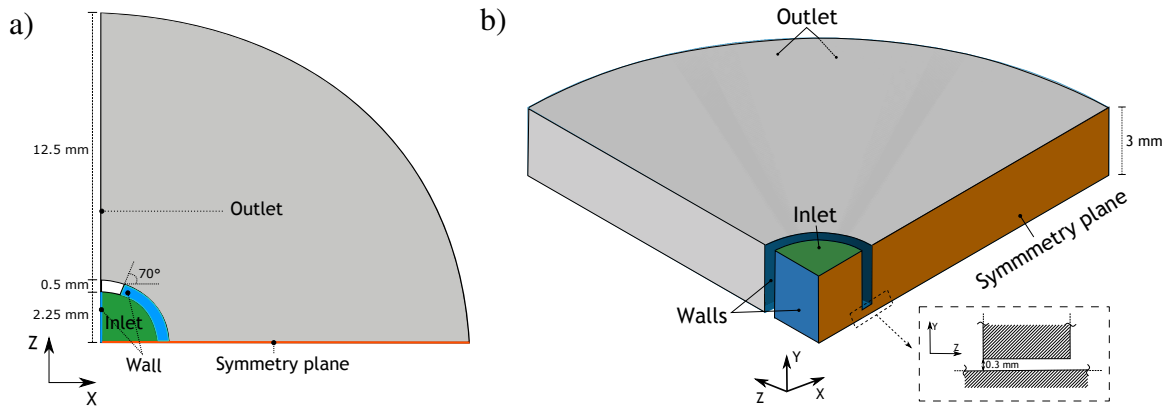


Fig. 4.4 Numerical domain of the geometry 1 with the associated boundary conditions. The top view is presented on the left and an oblique view is presented on the right. The bottom face of the domain is set as wall.

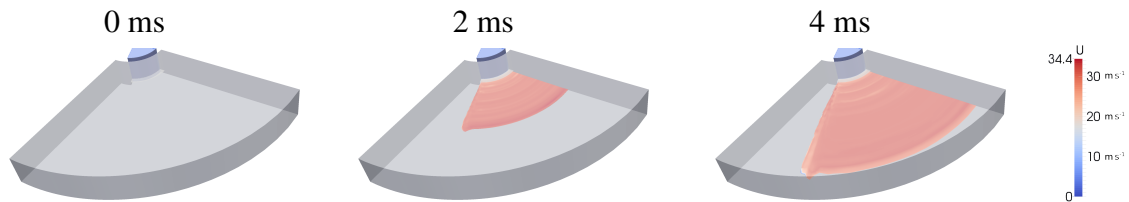


Fig. 4.5 Flow on the plate after 0, 2 and 4 ms respectively for the 140° pipe with an inlet flow of $2 \ell \text{ min}^{-1}$. The surface color indicates the surface velocity.

4.4 Results

4.4.1 Validation case

The surface velocity and liquid thickness with respect to the radial distance to the jet center are presented on the Figure 4.6. The liquid sheet thickness has been computed as the height at which the liquid fraction C is equal to 0.5. The numerical predictions are in good agreement with the analytical solution for both the height and the surface velocity away from the jet center. However, there are discrepancies between the numerical and the analytical solution for the surface speed prediction close to the jet impact area. These differences could arise from the limitation of Watson's solution close to the jet impact, where the boundary layer theory cannot be directly applied. A second explanation may be that the coarse meshes can not resolve correctly the flow in this area with these velocity gradients. However this difference does not affect the speed and height prediction away from the jet impact area for the normal and fine mesh cases. The coarse mesh case provides satisfactory results taking in account its low computational cost.

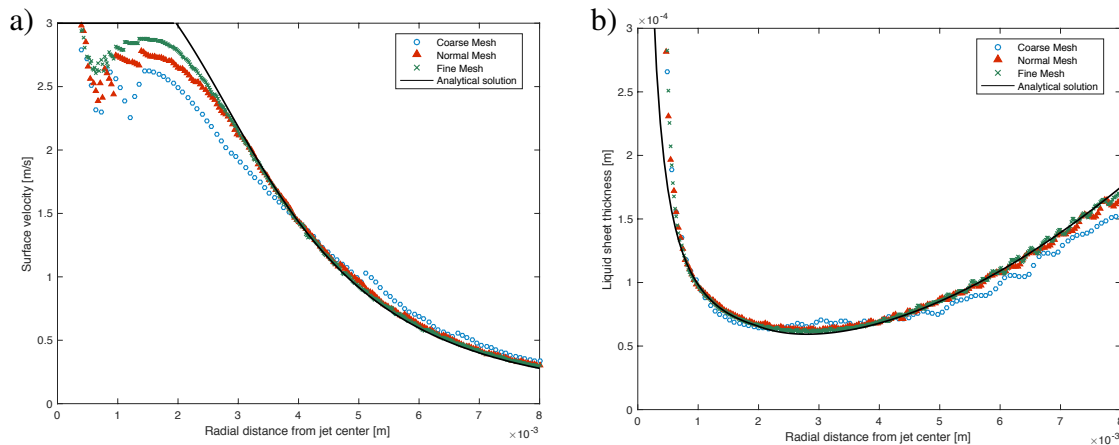


Fig. 4.6 a) Analytical and numerical solutions of the water thickness h in respect to the radial distance from the jet center r . b) Analytical and numerical solutions of the interface velocity U in respect of the radial distance from the jet center r . The numerical results with three mesh refinements are shown using different symbols.

4.4.2 Splash plate nozzle

Figure 4.7 presents the spatial distribution of the normalized water flow rate in the radial direction. The flow is normalized at each position by the inlet flow and the distance from the inlet center. Therefore, for an ideal case the flow rate would be 1 between -70 and 70° .

For all the cases, the water flows radially in respect to the inlet. The 140° geometry presents a more homogeneous flow rate distribution than the 180° geometry for the 1 and 2 $\ell \text{ min}^{-1}$ cases. The increase in flow rate produces different effects for each geometry. In the 140° case, the flow becomes more homogeneous, leading to an increase in the flow angle. In the 180° case, at 1 and 2 $\ell \text{ min}^{-1}$ the flow becomes less homogeneous causing a decrease of the flow angle.

4.5 Conclusion

The InterFoam solver assessment with an analytical solution provides satisfactory results. The predictions for both liquid sheet height and interface velocity were in good agreement with the analytical solution for the region away from the jet impact location. The discrepancies observed in the region close to the impact could arise from the limitation of the analytical solution close to the jet impact. The sensitivity study of the nozzle geometry and the inlet flow rate on the downstream flow allowed us to see a strong effect due to both parameters. The flow rate increase led to a more homogeneous flow in most of the cases. The inlet shape

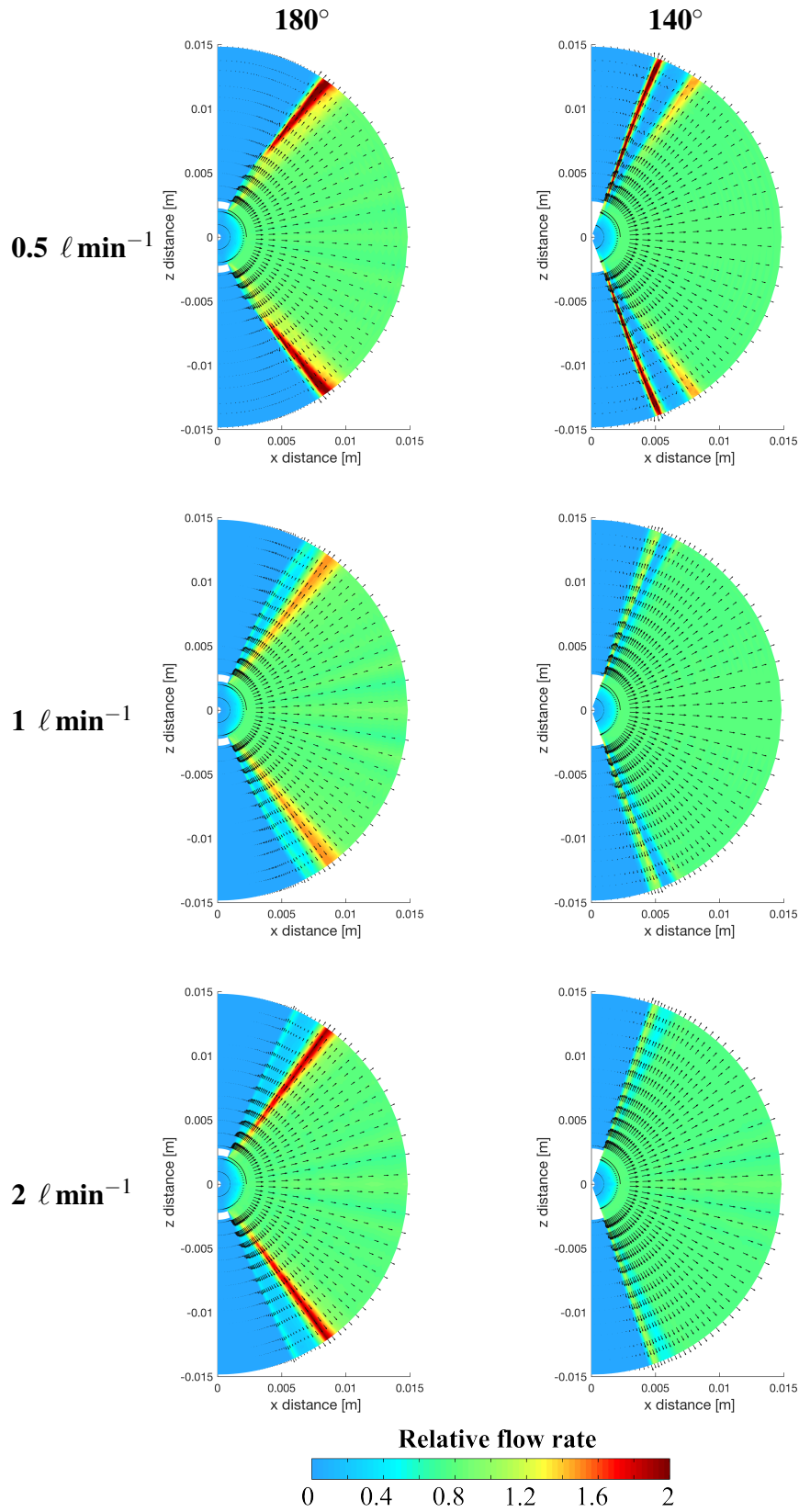


Fig. 4.7 Spatial distribution over the plate of the normalized flow rate for each case. The colors correspond to the normalized flow rate in the radial direction and the vectors to the average velocity in the liquid phase.

affects the downstream flow significantly. The 140° circular segment inlet seems suitable for our objective of generating a homogeneous flow on the nozzle plate.

Appendix A

Grid convergence

The use of three mesh refinements for the validation case study allows us to assess the discretization error. The relative error on the mean flow rate prediction away from the jet impact point (whilst $r \geq 10a$) is presented in the Figure 4.8 for each case. The predicted flow rate shows a monotonic convergence with the increase of cells. The computation of the order of the scheme leads to an order of accuracy of 1.73 which is lower than the theoretical

$$p = \frac{\log\left(\frac{\phi_{4h} - \phi_{2h}}{\phi_{2h} - \phi_h}\right)}{\log(r)} \quad (4.8)$$

where, r is the refinement factor equal to 2 in this case and are respectively for the fine, normal and coarse meshes.

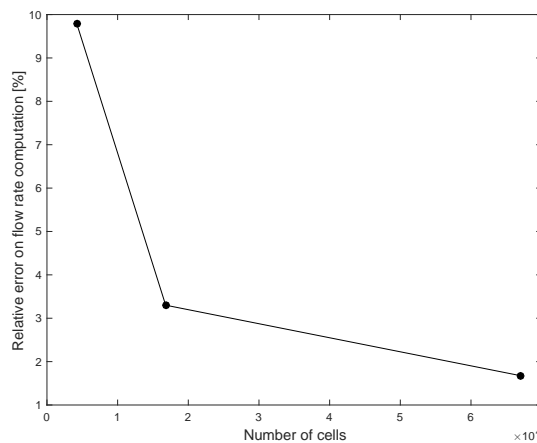


Fig. 4.8 Error on the estimation of the flow rate in respect with cell number.

Chapter 5

Dynamics of a thin radial liquid flow

5.1 Preamble

The analytical description of the flow on the nozzle plate is based on an extension of the analytical solution of the radial spread of a liquid jet over a horizontal surface. The fitting of the model parameters has been done using Computational Fluid Dynamics simulations. The present chapter has been published in a peer reviewed journal, the publication's details are shown in Table 5.1).

5.2 Introduction

The radial spread of a liquid film created by a round jet impact on a surface (figure 5.1a) occurs in numerous applications including mass and heat transfer. Surface cooling using an impinging water jet has been studied (Hosain et al., 2015; Ishigai et al., 1977; Liu et al., 1991). Spray formation by fire sprinkler (Aghajani et al., 2014; Marshall and Di Marzo,

Table 5.1 Summary of the appended publication.

Authors:	De Cock, Nicolas & Massinon, Mathieu & Ouled Taleb Salah, Sofiene & Mercatoris, Benoit & Vetrano, Maria Rosaria & Lebeau, Frédéric
Year:	2016
Title:	Dynamics of a thin radial liquid flow
Status:	Published
Peer reviewed:	Yes
Journal:	Fire safety journal
URL:	http://hdl.handle.net/2268/200526

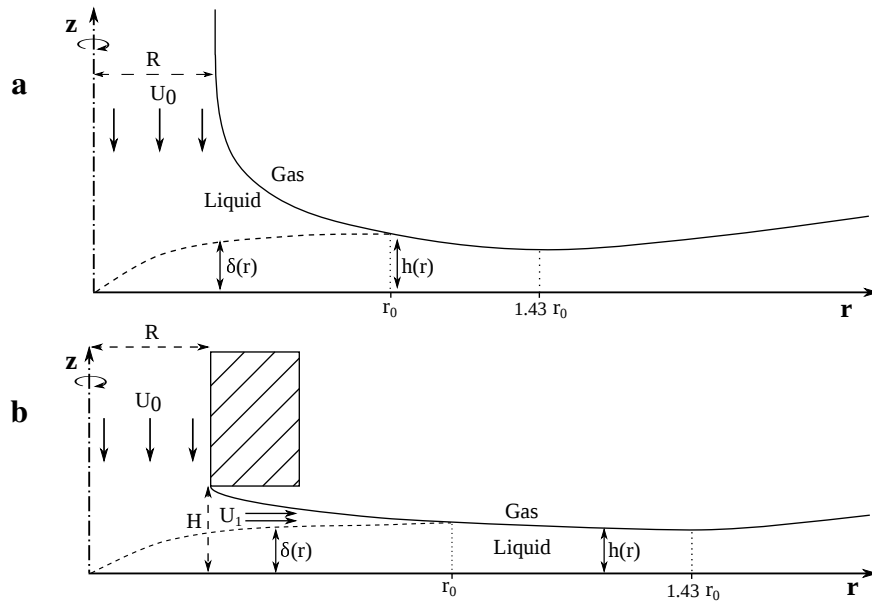


Fig. 5.1 Half radial cut of the radial flow created by a impact of a round jet on a horizontal plate (top) and thin cylindrical opening (bottom). With r the radial distance, R the jet radius, H the distance between the nozzle and the plate, U_0 jet mean velocity, U_1 the main stream velocity, $h(r)$ the liquid film thickness, $U(r)$ the interface velocity and $\delta(r)$ the boundary layer thickness.

2004; Wu et al., 2007) or plate nozzle (De Cock et al., 2014; Fard et al., 2007; Gordillo et al., 2014) involves a liquid film as the first step of a spray formation. The governing parameters of the spray formation process are the thickness and the velocity of the liquid layer. (Wu et al., 2007) proposed a sprinkler spray model which combines a film flow dynamic model based on analytical solution of (Watson, 1964) with an atomization model. Since sprinkler are usually pressure based, one way to reduce the flow rate whilst keeping the same velocity is to constraint the liquid by bringing the nozzle closer to the plate (figure 5.1b). This way of working has the advantage that it does not require the modification of the orifice size.

The hydrodynamics of the impact of an axi-symmetric liquid jet on a normal surface has been theoretically studied by Watson (Watson, 1964) who provided an analytical solution of the liquid layer thickness $h(r)$ and surface velocity $U(r)$ in respect with the radial distance from the jet center r , the liquid kinematic viscosity ν , the jet volumetric flow rate Q and the jet radius R . His solution is realized using a self similarity solution and the momentum integral solutions. He distinguished three main regions in the flow. The first one begins at stagnation point where the boundary layer starts growing and it finishes at $r = r_0$ where the whole flow is within the boundary layer. In the second region, the boundary layer is fully developed. The liquid layer thickness is controlled by both radial dispersion and viscous wall

effects. The liquid layer thickness is decreasing until $r = 1.43 r_0$ and then it increases. Measurements of the liquid layer thickness and the velocity profile realized by Azuma et al. (Azuma and Hoshino, 1984a,b,c) using needle probe and laser Doppler velocimeter show a good agreement with the solution proposed by Watson for flows with a Reynolds number ranging from $2.2 \cdot 10^4$ (Azuma and Hoshino, 1984b) to $1.7 \cdot 10^5$ (Azuma and Hoshino, 1984c). The laminar to turbulent transition defined by Azuma and Hoshino (1984a) as the presence of sandpaper-like waves in more than 50 % of the peripheral direction. This transition occurs for a Re around $5 \cdot 10^4$.

When the nozzle is close to the plate (figure 5.1b), the water is discharging through a thin cylindrical opening creating a thin liquid layer spreading radially. At the inner corner of the constriction, the flow is separating leading to an actual discharging area smaller than $2\pi RH$. Lichtarowicz and Markland (1963) performed 2D numerical computations using the free-streamline theory on right-angle elbows with geometrical ratio, upstream to downstream channel width, ranging from 0.01 to 1.2. They compute the contraction coefficient (C_c) defined as the ratio of the asymptotic stream width downstream of the corner to the upstream channel width. The C_c was decreasing with the geometrical ratio. Chu (2003) investigated the effect of the elbow angle on the contraction coefficient showing that C_c was decreasing with the elbow angle. Their computations of the C_c has been validated by Hou et al. (2014) who solved the Euler equations of the flow at a corner using a Lagrangian model based on smoothed particle hydrodynamics method.

The goal of this paper is to provide an analytical description of the thickness and the velocity of a thin liquid layer generated by radial flow generated by a thin cylindrical opening. The solution combines the analytical solution given by Watson and a correlation expression the flow acceleration due to the flow separation in respect with the geometrical ratio. The paper is structured as follows: in § 5.3.1 the theoretical development proposed by Watson for a round jet spreading radially is summarized. The full description of the theoretical developments can be found in Watson's paper (Watson, 1964); in § 5.3.2 presents the theoretical extension to a radial flow of the Watson solution; in § 5.4 presents the numerical computations used to find the relationship between the geometrical ratio and the flow acceleration; finally, in § 5.5 the validity and the quality of the proposed model is discussed.

5.3 Theoretical developments

5.3.1 Flow created by a round liquid jet impacting on a horizontal plate

Fully developed region: similarity solution

This axi-symmetric flow can be described as a thin layer by the following equations:

$$\frac{\partial(ru)}{\partial r} + \frac{\partial(rw)}{\partial z} = 0 \quad (5.1)$$

$$u \left(\frac{\partial u}{\partial r} \right) + w \left(\frac{\partial u}{\partial z} \right) = \nu \left(\frac{\partial^2 u}{\partial z^2} \right) \quad (5.2)$$

where r is the radial distance from the jet center [m], z is the distance upward from the plate [m], u and w are the corresponding velocity components [m s^{-1}], ν is the kinematic viscosity [$\text{m}^2 \text{s}^{-1}$].

The hypothesis are: a no slip condition at the plate (eq. 5.3), the shear stress at the free surface is negligible (eq. 5.4) and the flow rate along the radial axis is constant (eq. 5.5).

$$u = w = 0 \quad \text{at} \quad z = 0 \quad (5.3)$$

$$\frac{\partial u}{\partial z} = 0 \quad \text{on} \quad z = h(r) \quad (5.4)$$

$$Q = 2\pi r \int_0^{h(r)} u \, dz \quad (5.5)$$

The velocity profile in the axial direction u can be rewritten as function of the velocity at the free surface $U(r)$ and a similarity solution $f(\eta)$:

$$u = U(r)f(\eta) \quad \text{with} \quad \eta = \frac{z}{h(r)} \quad (5.6)$$

Then, the flow rate along the radial direction given by the equation 5.5 can be rewritten as:

$$Q = 2\pi r U h \int_0^1 f(\eta) \, d\eta \quad (5.7)$$

Watson used the integral method to retrieve the integral of the velocity profile over the liquid layer thickness equal to:

$$\int_0^1 f(\eta) \, d\eta = \frac{2\pi}{3\sqrt{3}c^2} \quad (5.8)$$

with c is a constant of integration equal to 1.402. Finally, the constant flow equation 5.7 can be rewritten as:

$$rUh = \frac{3\sqrt{3}c^2Q}{4\pi^2} \quad (5.9)$$

Using the equations 5.2 and 5.9, $U(r)$ and $h(r)$ can be expressed as:

$$U(r) = \frac{27c^2Q^2}{8\pi^4\nu(r^3 + l^3)} \quad (5.10)$$

$$h(r) = \frac{2\pi^2\nu(r^3 + l^3)}{3\sqrt{3}Qr} \quad (5.11)$$

where l is a constant length arising from the integration of $\frac{\partial U}{\partial r}$ in the equation 5.2. The value of l will be determined later using the boundary development region equations knowing that $h(r_0) = \delta$.

Boundary development region: general approximate solution

In the first region, the boundary layer is not fully developed thus the velocity outside the boundary layer is considered as equal to the velocity of the jet U_0 which is expressed as:

$$U_0 = \frac{Q}{\pi R^2} \quad (5.12)$$

Inside the boundary layer, the velocity profile is defined by the similarity function $f(\eta)$:

$$u = U_0 f\left(\frac{z}{\delta}\right) \quad \text{with} \quad u = U_0 \quad \text{when} \quad z \geq \delta(r) \quad (5.13)$$

The momentum integral equation is equal to:

$$\left(\frac{d}{dr} + \frac{1}{r}\right) \int_0^\delta (U_0 u - u^2) dz = \nu \left(\frac{\partial u}{\partial z}\right)_{z=0} \quad (5.14)$$

Integration and rewriting of equation 5.14 gives:

$$\delta = \sqrt{\frac{\sqrt{3}c^3\nu r}{(\pi - c\sqrt{3})U_0}} \quad (5.15)$$

The constant flow rate expression given by equation 5.5 can be rewritten as:

$$Q = 2\pi r \left(U_0 \delta \int_0^1 f(\eta) d\eta + U_0(h - \delta) \right) \quad (5.16)$$

From which h can be derived:

$$h(r) = \frac{R^2}{2r} + \left(1 - \frac{2\pi}{3\sqrt{3}c^2}\right) \delta \quad (5.17)$$

Then, the expression of h is the sum of two effects: the radial dispersion of the flow and the displacement thickness of the boundary layer. This expression is valid until the whole flow is within the boundary layer, *i.e.* when $r \leq r_0$. The r_0 value is determined by founding the location where the boundary layer volume flux is equal to the inlet volume flux:

$$r_0 U_0 \delta(r_0) = \frac{3\sqrt{3}c^2 Q}{4\pi^2} \quad (5.18)$$

Using equation 5.15, r_0 is equal to:

$$r_0 = 0.3155 \sqrt[3]{\frac{QR^2}{\nu}} \quad (5.19)$$

Since U is equal to U_0 when $r = r_0$. Therefore the value of l can be found using equations 5.9 and 5.19:

$$l = 0.5673 \sqrt[3]{\frac{QR^2}{\nu}} \quad (5.20)$$

Finally, the equations describing the liquid layer thickness are equations 5.17 when $r \leq r_0$ and 5.11 when $r > r_0$. The surface velocity is equal to the initial velocity U_0 when $r \leq r_0$ and then it is given by the equation 5.10 when $r > r_0$.

5.3.2 Radial flow of a thin liquid film

When the gap, H , between the jet nozzle and the plate is reducing the discharging area may be smaller than the inlet area leading to an increase of the main flow velocity downstream of the thin cylindrical opening (figure 5.1b). Moreover, a flow separation is occurring at the nozzle inner corner leading to the contraction of the streamline which consequently decrease the actual discharging area. The main flow velocity changes from U_0 in the inlet pipe to U_1 downstream of the jet impact region. This increase of velocity is defined here as $\frac{1}{\alpha}$. Therefore, U_1 reads as:

$$\alpha = \frac{U_0}{U_1} = \frac{2HC_C}{R} \quad (5.21)$$

$$U_1 \alpha = U_0 \quad (5.22)$$

The expression of α should lies between 0 and 1 and it should depends on $\frac{H}{R}$, defined as the opening ratio. Making the hypothesis that the downstream flow can be described by the

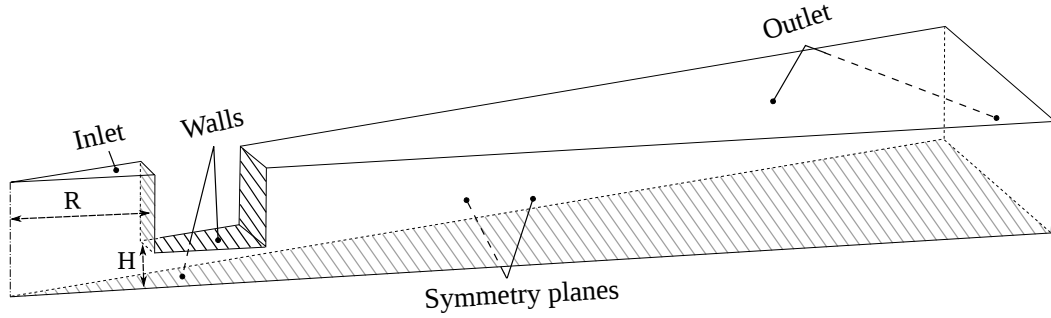


Fig. 5.2 Computational domain used to simulate the flow generated by a thin cylindrical opening with the associated boundary conditions.

Watson's model taking in account this main flow acceleration, the height and the surface velocity of the liquid layer can be rewritten adding the new variable α . When $r \leq r_0$, the equations 5.15, 5.17 and 5.20 become:

$$\delta = \sqrt{\frac{\alpha\sqrt{3}c^3vr}{(\pi - c\sqrt{3})U_0}} \quad (5.23)$$

$$h(r) = \frac{\alpha R^2}{2r} + \left(1 - \frac{2\pi}{3\sqrt{3}c^2}\right) \delta \quad (5.24)$$

$$r_0 = 0.3155 \sqrt[3]{\frac{\alpha QR^2}{\nu}} \quad (5.25)$$

When $r > r_0$, the equations 5.10, 5.11 and 5.20 become:

$$U(r) = \frac{27c^2Q^2}{8\pi^4\nu(r^3 + l^3)} \quad (5.26)$$

$$h(r) = \frac{2\pi^2\nu(r^3 + l^3)}{3\sqrt{3}Qr} \quad (5.27)$$

$$l = 0.5673 \sqrt[3]{\frac{\alpha QR^2}{\nu}} \quad (5.28)$$

In this set of equation only l is affected by the velocity increase of the main flow.

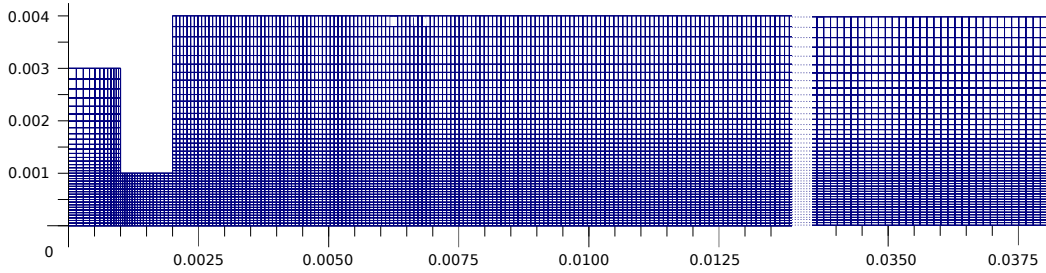


Fig. 5.3 Example of mesh for a nozzle with a radius of 1 mm and a height of 1 mm. The dimensions are given in meters.

5.4 Numerical modelling

5.4.1 Computational domain

Since the flow generated by a thin cylindrical opening is axi-symmetric, the computational domain was two-dimensional (figure 5.2). In the radial direction, the domain was starting at the middle of the inlet pipe and it was ending at $r = 3.5 r_0$. The height of the domain at the top of the plate was set at four times the inlet radius and the height of the inlet was set at three times the inlet radius.

The computational grid was a wedge (figure 5.2) with an opening angle of 5° and 1 cell thick running along the plane of symmetry. The mesh resolution was adapted to each geometry using an automatic routine. A mesh refinement region was set at the exit of the inlet. In this region, the z resolution was set as $\Delta z = \min\left(\frac{H}{25}, \frac{R}{75}\right)$ and the r resolution is set as $\Delta r = \frac{R}{15}$. The cell size was growing with the distance from the inlet center. The maximal cell aspect ratio was 5 and the cell-to-cell expansion ratio was no exceeding 1.1. The number of cells was ranging from 50 000 to 250 000 for the largest geometry. An example of mesh is illustrated by the figure 5.3.

5.4.2 Computational parameters

Numerical simulations were performed in order to retrieve the value of α . The effect of the relative gap on the flow acceleration were studied for relative opening ranging from 0.2 to 3. Two different inlet radius R were tested 1 and 2 mm. The analytical model will be used to design nozzle with a flow rate ranging from 1 to 2 $\ell \text{ min}^{-1}$ over 120° . Therefore, simulations were performed using flow rates Q : 3 and 6 $\ell \text{ min}^{-1}$ over 360° . The flow rates of 3 and 6 $\ell \text{ min}^{-1}$ over 360° . The Reynolds numbers in the inlet pipe, $Re = \frac{Q}{Rv}$, were ranging from $2.5 \cdot 10^4$ to 10^5 . The thickness of the inlet pipe wall was 1 mm defining the length of the restriction. The fluids used for the simulations were water and air at 20°C with the

following properties: $\rho_{water} = 998 \text{ kg}^1 \text{ m}^{-3}$, $\nu_{water} = 1 \cdot 10^{-6} \text{ m}^2 \text{ s}^{-1}$, $\rho_{air} = 1.2 \text{ kg}^1 \text{ m}^{-3}$ and $\nu_{air} = 15 \cdot 10^{-6} \text{ m}^2 \text{ s}^{-1}$. The surface tension effects were neglected.

5.4.3 Boundary conditions

The inlet boundary was set with an uniform velocity equal to $U_0 = \frac{Q}{\pi R^2}$, a normal gradient of pressure equal to 0 and a liquid fraction ϕ equal to 1. The wall boundaries were set as no slip, zero normal gradients for ϕ and the pressure. The outlet was set at atmospheric pressure with no liquid backflow. Axi-symmetric boundary conditions were set the for the front and back plans of the domain.

5.4.4 Numerical method

The InterFoam solver from the *OpenFOAM C++* toolbox has been used to perform numerical simulations. InterFoam is a Volume Of Fluid (VOF) solver for incompressible two-phase flow. This solver provided good results for inertia-dominated flows with large fluid density ratios ($\geq 10^3$), such as round jet impact (Deshpande et al., 2012). The governing equations are discretized and solved using the finite volume method and the PISO algorithm respectively. The diffusion terms were discretized using a second order central difference scheme. All the cases were considered in a laminar mode since the range of simulation is close or below the laminar to turbulence transition (Azuma and Hoshino, 1984b). Therefore, no extra turbulence model has been used. The computations were unsteady and the time step was controlled by the Courant number set at 0.45. Consequently, the results presented in the next section are an averaged solution of the flow over a certain time interval at the steady state.

5.4.5 Post processing

The liquid layer thickness $h(r)$ was computed by integrating the liquid fraction ϕ over the z direction: $h(r) = \int \phi(r) dz$. The surface velocity was computed at the location where $\phi = 0.5$ using a linear interpolation. In order to present results in a concise way, the radial distance, the height and the surface velocity profiles are expressed in non dimensional way has been adapted from Watson (1964): $r^* = r \sqrt{\frac{\nu}{\alpha Q R^2}}$, $h^* = h(r) \sqrt[3]{\frac{Q}{\alpha^2 \nu R^4}}$ and $U^* = 10 \left(\frac{\alpha U(r)}{U_0} \right)$.

α_{obs} was computed using the equation 5.21. U_1 was computed as the average of the main flow velocity from $r = 0$ until $r = r_0$. Moreover, three extra values of α were computed by fitting. The liquid sheet thickness equations 5.24 and 5.27 were reduced to two simpler expressions depending on the radial distance r and on four coefficients a, b, d and e . For each

case, the values of the four coefficients were retrieved by fitting the equation 5.29 on the thickness profile $h(r)$ from the numerical data.

$$h(r) = \begin{cases} \frac{a}{r} + b\sqrt{r}, & r \leq r_0 \\ \frac{d(r^3+e)}{r}, & r > r_0. \end{cases} \quad (5.29)$$

Then, from the equations 5.23, 5.24 and 5.28, three expressions of α were obtained:

$$\begin{cases} \alpha_a = \frac{2a}{R^2} \\ \alpha_b = \left(\frac{b\sqrt{U_0}}{0.9955\sqrt{v}} \right)^2 \\ \alpha_e = \frac{e v}{0.1826 Q R^2} \end{cases} \quad (5.30)$$

There is no expression for α_d since d is independent of α . Finally, some flow acceleration for similar flow available in the literature are used for comparison. Lichtarowicz and Markland (1963) and Mankbadi and Zaki (1986) computed the contraction coefficient for a 90° elbow with several ratios upstream to downstream. Azuma and Hoshino (1984a) realized measurements of the flow velocity at the exit of a circular inlet for small opening ratios.

5.4.6 Model quality

The quality of the analytical model given by the equations 5.24 and 5.27 was assessed by computing the Normalized Root Mean Square Deviation (NRMSD) using the numerical data as observed values. The NRMSD was computed as:

$$NRMSD = \frac{\sqrt{\frac{1}{n} \sum_{i=1}^n (\hat{Y}_i - Y_i)^2}}{(Y_{max} - Y_{min})} \quad (5.31)$$

where n is the number of observation, \hat{Y}_i are the values predicted by the model, Y_i are the observed values and $(Y_{max} - Y_{min})$ is the amplitude of the variation within the dataset.

5.5 Results and discussion

Comparison of the different α in respect with the relative gap is presented on the figure 5.4. α is increasing with the opening ratio until the asymptotic value of 1 is reached. For most of the cases the different values of α are close to each other. Therefore, taking in account the flow acceleration allows to extend the set of equation from the jet flow to the thin cylindrical opening flow. When the opening ratio is small, i. e. < 1.5 , there are discrepancies between

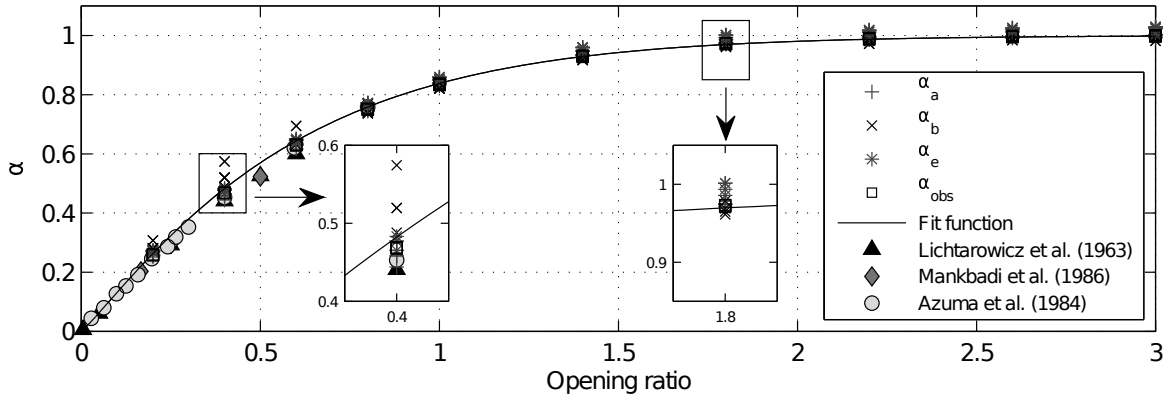


Fig. 5.4 Comparison of the value of α retrieved from the post processing or found in the literature in respect with the relative gap.

the different values of α and α_b . α_b is larger than the other values of α showing that the displacement thickness induced by the boundary layer development is larger than expected. For these cases, close to the inlet the velocity outside boundary layer is not equal to the free stream velocity everywhere. Indeed, the velocity is lower close to the liquid/air interface. Therefore, the liquid height is higher than expected to compensate this deficit of velocity. When the opening ratio is large, i.e. > 1.5 , α is close to one, therefore the flow is close to the free jet impact flow. The comparisons with the measurements of Azuma and Hoshino (1984a) show good agreement as well as the theoretical contraction coefficients computed by Lichtarowicz and Markland (1963) and Mankbadi and Zaki (1986). From these results, α can be expressed in respect with the opening ratio $\frac{H}{R}$ as:

$$\alpha = \left(1 - e^{-1.82 \left(\frac{H}{R} \right)^{1.11}} \right) \quad (5.32)$$

The figure 5.5 compares the numerical data from all the cases and the model prediction for the surface velocity and liquid thickness in respect with the radial distance. The reduction to a non dimensional expression of $U(r)$ and $h(r)$ was realized using the expression of α given by the equation 5.32. After, the reduction to the non dimensional expression all the curves are really close to each other showing that the flow equations with α are describing on the downstream flow well the effect of the gap between the inlet and the plate. When $r^* < 0.1$, the surface velocity is lower than the main stream velocity as illustrated by the inside graph. When $0.3 < r^* < 0.4$, the observed values are lower than the predicted one because the velocity profile was decreasing close to the interface liquid/air. For the liquid layer thickness $h(r)$, the prediction and the observed data are really close to each other. For

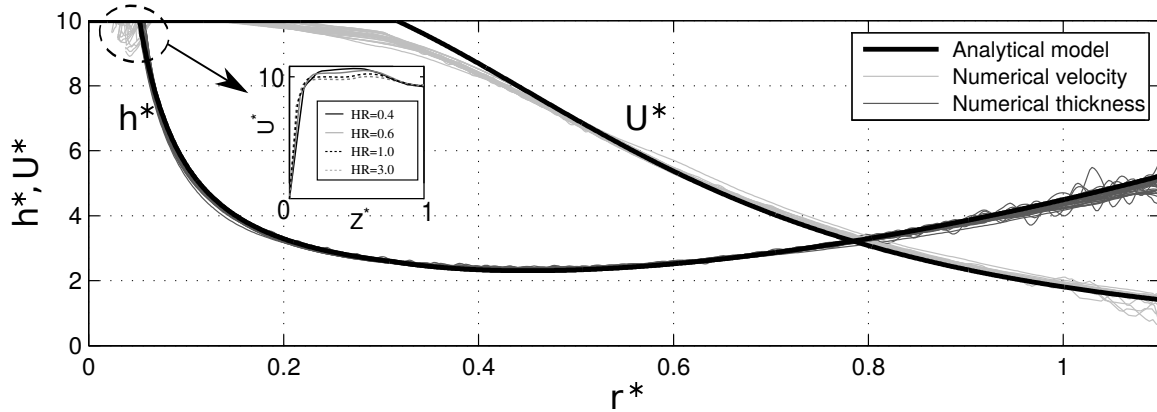


Fig. 5.5 Comparison between the numerical data from all the cases and the model prediction for the surface velocity and liquid thickness in respect with the radial distance. The inside graph gives the velocity profiles close at 1 mm from the nozzle exit for the cases with $R = 1$ mm and $H = 0.4, 0.6, 1$ and 3 mm with $z^* = \frac{z}{\delta}$.

r^* close to 1, some numerical instabilities are observed for both simulations creating wiggles in the solutions.

The NRMSD on the liquid sheet thickness and interface velocity prediction in respect with the relative opening ratio are presented on the figure 5.6. For both the surface height and the surface velocity, the NRMSD is larger when the opening ratio is smaller than 1. Then, when the opening ratio is larger than 1 the NRMSD is equal to 3 % for the surface velocity and to 2 % for the liquid layer thickness. There is no significant difference between the different cases.

5.6 Conclusion

The present work proposed an extension of the existing analytical development on the radial spread of a liquid jet over a horizontal surface to the case of a laminar thin radial flow. When the gap, H , between the jet nozzle and the plate is reduced the discharging area may be smaller than the inlet area leading to an increase of the main flow velocity downstream of the thin cylindrical opening. This increase of velocity, defined here as $\frac{1}{\alpha}$, can be related to the relative gap of the nozzle $\frac{H}{R}$. Numerical computations with a volume of fluid method were realized for $\frac{H}{R}$ ranging from 0.2 to 3 and with Q of 3 and 6 $\ell \text{ min}^{-1}$. The results of these computations allowed to express α in respect of $\frac{H}{R}$. α is increasing with the opening ratio until the asymptotic value of 1 is reached. Taking in account the flow acceleration allowed to extend the set of equation from the jet impacting flow to the thin cylindrical opening flow. The liquid layer thickness and the surface velocity differ with a maximum

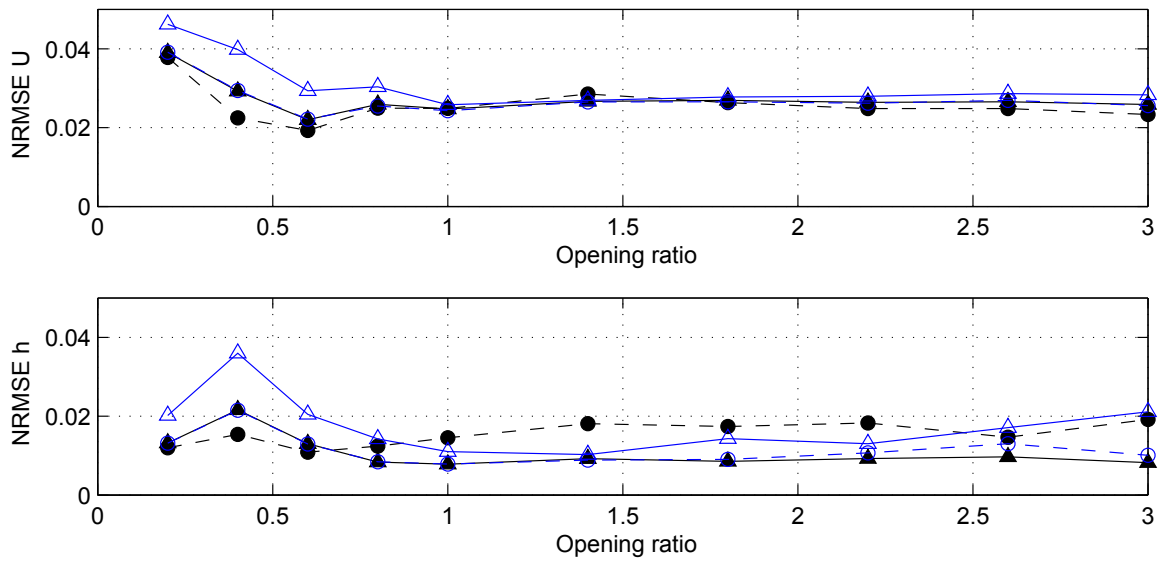


Fig. 5.6 NRMSD on the interface velocity (top) and the liquid sheet thickness (bottom) predictions in respect with the relative opening ratio. Each marker corresponds to a specific radius/flow rate combination: $-\triangle-$ is for $R = 1 \text{ mm}$ & $Q = 3 \text{ l min}^{-1}$, $-\circ-$ is for $R = 2 \text{ mm}$ & $Q = 6 \text{ l min}^{-1}$, $-\blacktriangle-$ is for is for $R = 2 \text{ mm}$ & $Q = 3 \text{ l min}^{-1}$ and $-\bullet-$ is for $R = 2 \text{ mm}$ & $Q = 6 \text{ l min}^{-1}$.

error of 4 % between the flow predicted by the model and computations. Main discrepancies appear in the region close to the nozzle where the analytical model assumption of a constant velocity outside the boundary layer is not valid. However, further downstream the model and the computations are in good agreement. The present analytical model and correlation has been done for laminar flow ($Re < 10^5$). The extension of this model to turbulent flow would required to take in account the extra mixing induced by the eddies and it may also require to adapt the velocity profile. Further work will focus on the experimental validation of the proposed analytical solution.

Chapter 6

Nozzle with narrow droplet size distribution

6.1 Introduction

In field spray application, the hydraulic nozzle are often used at a constant flow rate. The optimal droplet size distribution changes according to the target. Using the analytical model developed in the previous chapter, a design methodology is presented. The Figure 6.1 summarizes the main steps of the nozzle design. The design starts by defining the optimum in term of droplet size according the target. Then, the objective in term droplet diameter set the jet properties (size and speed) in order to be in Rayleigh-Plateau regime. Next, using the analytical model presented in the chapter 5 a nozzle geometry can be proposed. Finally, the spray produced by a nozzle prototype is assessed by using the high-speed imaging technique presented in the chapter 3.

6.2 Nozzle geometry

Figure 6.2 shows a design sketch of the nozzle. The nozzle is constituted of a inlet pipe ending on a perpendicular plate. There is a thin opening at the junction between the pipe and the plate. The inlet is characterized by 3 geometrical parameters: the thin opening height H , the inlet pipe radius R and the opening angle. The effect of H and R on the downstream flow has been investigated in the chapter 5. The edge of the plate is constituted of channels formed by structures. These channels aim to divide the liquid sheet in multiple jets.

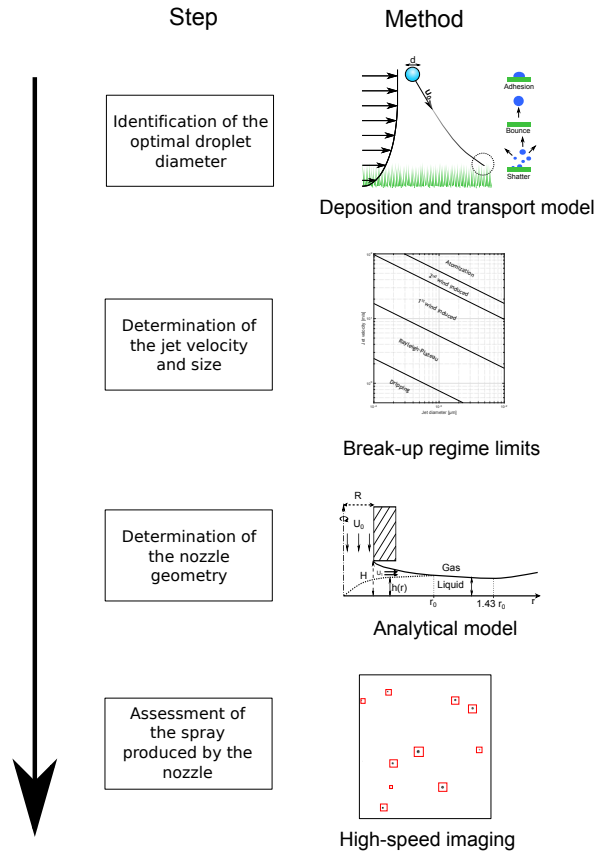


Fig. 6.1 Summary of the nozzle design procedure.

6.3 Design methodology

Making the hypothesis of uniform jets, the number of jets N_{jet} required to achieve the objective flow rate is given by the ratio of the nozzle flow rate Q_{tot} to the flow rate of a single jet Q_{jet} :

$$N_{jet} = \frac{Q_{tot}}{Q_{jet}} \quad (6.1)$$

Knowing that the overall flow rate the number of jets to achieve a specific droplet size, the flow rate of a single jet is given by:

$$Q_{jet} = \frac{\pi U_{jet} D_{jet}^2}{4} \quad (6.2)$$

The droplet diameter produced by the breakup of a jet in Rayleigh-Plateau regime produces droplet with a diameter equals to 1.89 time the jet diameter. Therefore, D_{drop} is

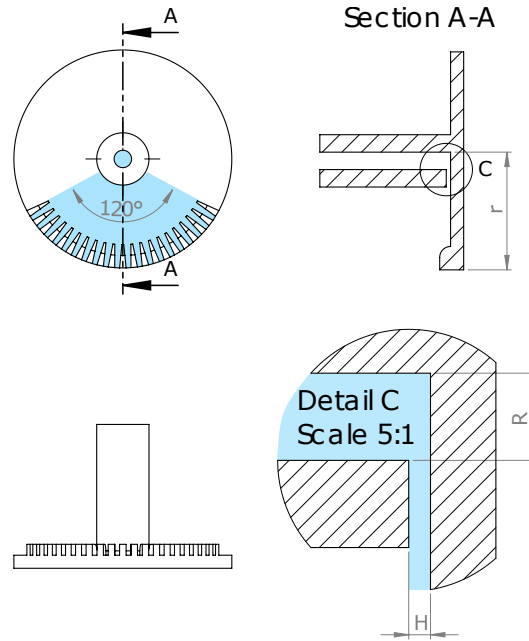


Fig. 6.2 Nozzle geometry, top and side views. H , R and r are the gap between the inlet and the plate, the inlet radius and the distance from the inlet center respectively. The blue contour in the 2D drawing indicates the surface wet by the liquid.

equal to:

$$D_{drop} = 3.78 \sqrt{\frac{Q}{\pi N_{jet} U_{jet}}} \quad (6.3)$$

The overall flow rate Q_{tot} is fixed by the design goal, for agricultural nozzle a flow rate of $1 \ell \min^{-1}$, $1.67 \cdot 10^{-5} m^3 s^{-1}$, is considered. The jet velocity U_{jet} is considered as the velocity of the liquid sheet at the exit of the plate. Neglecting the additional viscous dissipation induced by the terminal structures, the jet velocity can be approximated by the average velocity of the liquid sheet provided by the analytical model developed in the chapter 5. The equations describing the evolution h in respect to the radial distance are summarized in the section 5.3.2. The average liquid sheet velocity \bar{U} is a function of the liquid sheet height h , the radial distance r and the nozzle flow rate Q_{tot} :

$$\bar{U} = \frac{Q_{tot}}{2\pi h r} \quad (6.4)$$

The spatial evolution of \bar{U} for three nozzles configurations with various H and R is presented on Figure 6.3. The average velocity of the liquid sheet is decreasing with increasing distance from the nozzle center because of viscous dissipation. The nozzle configuration affects the initial liquid sheet velocity. r , R and H affects the average velocity.

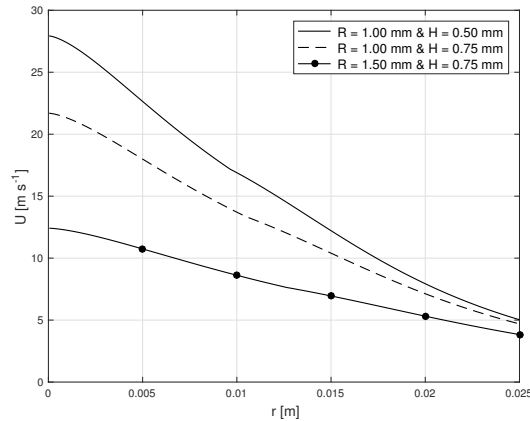


Fig. 6.3 Average liquid sheet velocity in respect to the radial distance from the nozzle center for three nozzle configurations.

6.4 Theoretical design

In the chapter 2, an optimum range of droplet with a diameter of $225 \mu\text{m}$ was found. Therefore, the jets should have a diameter of $120 \mu\text{m}$. For a jet diameter of $120 \mu\text{m}$ the upper velocity limit to remain in the Rayleigh regime is around 15 m s^{-1} (cf figure 1.4) giving $Q_{jet} = 1.58 \cdot 10^{-7} \text{ m s}^{-3}$. Thus 98 jets are required to ensure a flow rate of 1 l min^{-1} . There are two design constraints, the flow has to be fast in order to have a reduce number of jets and the plate should be large enough to support all the grooves generating the jets. The figure 6.4 shows the iso contours of the average velocity in respect to r , H and R . One configuration which would fit this requirement is a nozzle with a inlet radius R of 1 mm, a gap H of 0.3 mm and a plate with a radius of 15.25 mm. At the edge of the disk the grooves of 0.12 mm would be spread over 120° and separated of each other by 0.225 mm. A nozzle with such dimensions couldn't be properly prototyped by 3D printing, therefore the experimental assessment has been done on a larger scale model as proof of concept.

6.5 Proof of concept

A nozzle design has been prototyped by 3D printing, the dimensions are presented on the figure 6.5. The impactor ends with 30 channels over 180° , the gap between the plate and the inlet is 0.4 mm, the inlet radius is 0.225 mm and the impactor radius is 15 mm. The figure 6.6 a shows the liquid jets formed at the edge of the plate. The jets are well separated and have uniform sizes. The velocity of these jets has been measured for various flow rate and compared to the prediction of the analytical model as shown on Figure 6.6 b. The measured values are slower than the predicted ones which may be linked to the grooves. This analytical

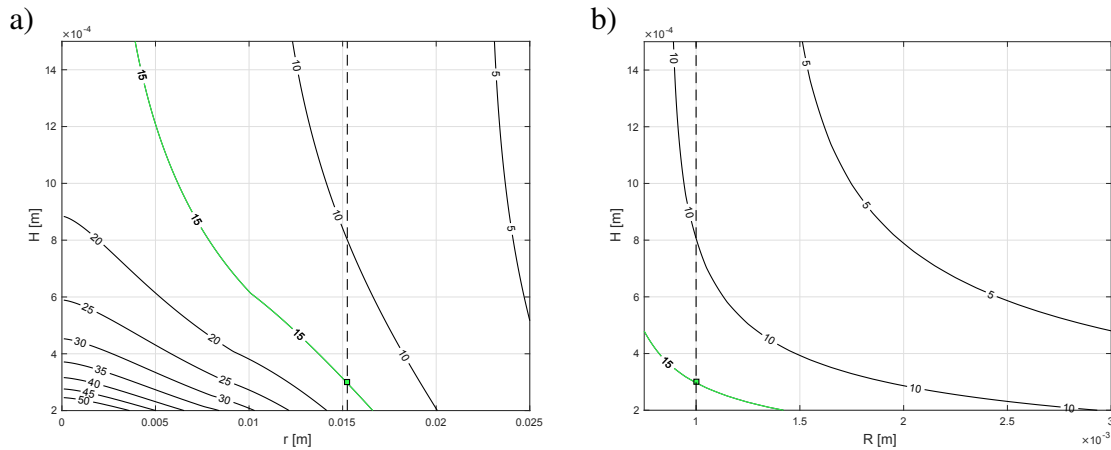


Fig. 6.4 Iso contour of the average liquid sheet velocity. a) constant $R = 1$ mm was considered. b) constant $r = 15.25$ mm was considered.

Table 6.1 Reduced parameters of the droplet size distribution measured at 50 mm downstream of the disk edge for the three flow rates.

Flow rate [$\ell \text{ min}^{-1}$]	D_{v10} [μm]	D_{v50} [μm]	D_{v90} [μm]	RSF [-]
1.13	699	892	1120	0.47
1.38	720	923	1168	0.49
1.78	704	960	1192	0.50

model predicts the velocity and the height of a liquid sheet formed at the exit of a narrow slit such as the exit of the injector. The model does not take into account the presence of channel which would slow down the liquid sheet by increasing the friction between the liquid and the solid. The velocity of the jets is increasing with the increase of the flow rate.

The jets breakup occurs after a dozen of mm downstream of the plate edge. Droplet size distribution measurements have been realized at 50 mm downstream of the disk edge. The figure 6.7 shows the cumulative droplet size distribution for three flow rates and the Table 6.1 summaries the reduced parameters of the droplet size distributions. For each case, the droplet size distribution have a RSF around 0.5. The increase of flow rate leads to an increase of the average droplet size expressed by the D_{v50} .

6.6 Conclusion

A design methodology has been presented and a theoretical design has been sized. This design couldn't be properly prototyped because its small dimensions. However, measurements on a upscale model shows good agreement with the analytical model in this regime. However,

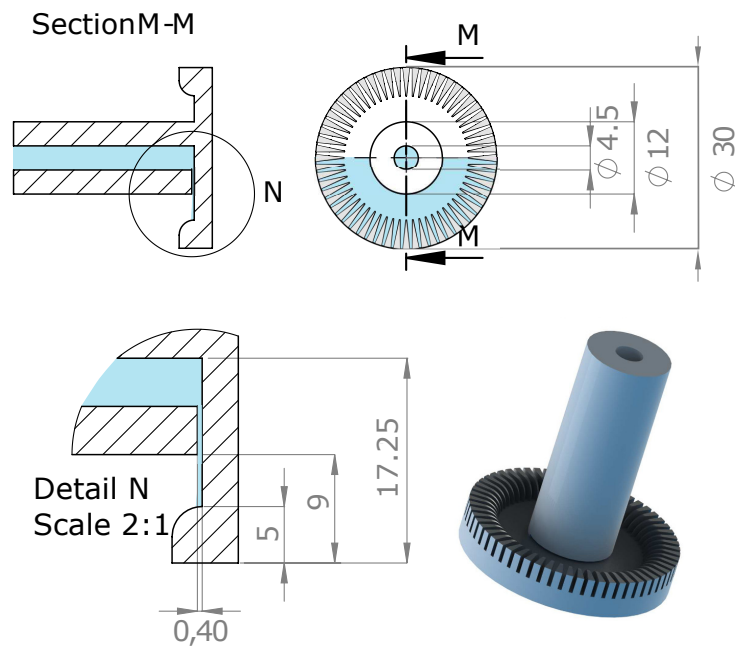


Fig. 6.5 Dimensions of the upscale nozzle model.

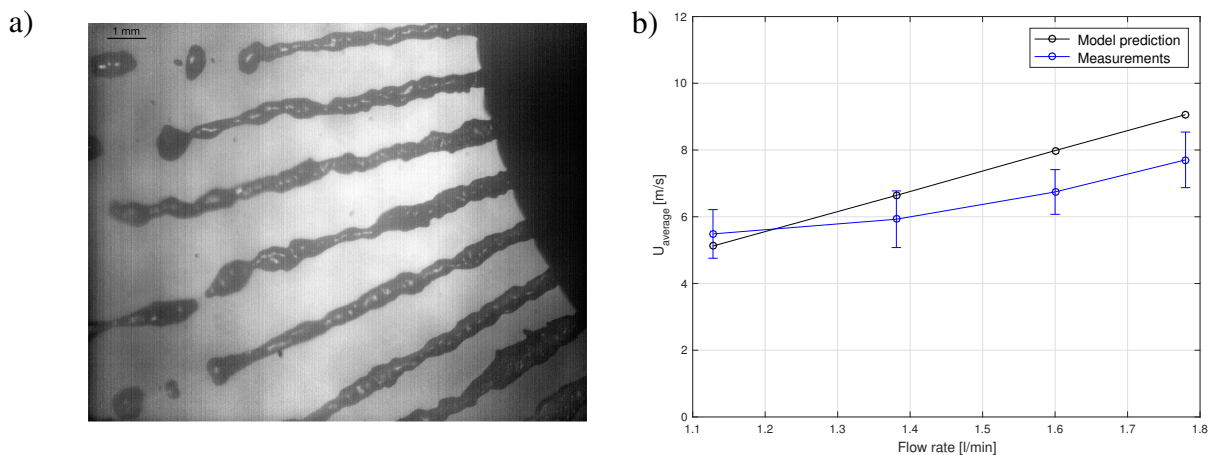


Fig. 6.6 High-speed imaging measurements at the exit of the nozzle. a) Shadowgraphy image at the edge of the nozzle plate. b) Comparison of the average jet velocity measured at the edge of the plate and the analytical model predictions. The error bars correspond to the standard error on 10 measurements.

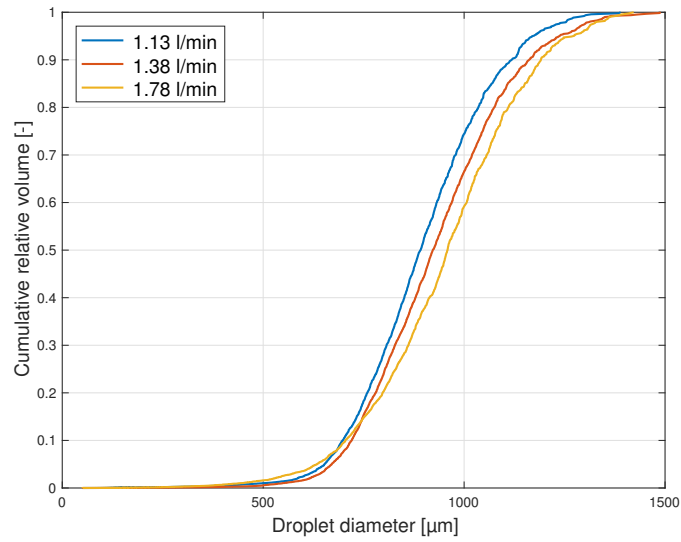


Fig. 6.7 Cumulative droplet size distribution measured at 50 mm downstream of the disk edge.

at small scale the model prediction may diverge because of change in the flow nature from laminar to turbulent. Moreover, the jets splitting may be challenging at small dimensions.

Chapter 7

Conclusions and perspectives

Strategies to control the droplet size distribution in terms of Dv_{50} and RSF may offer promising solutions for reducing adverse impacts on environment of spray applications. Indeed, numerical investigations using droplet transport and deposition numerical models showed that droplets with diameters ranging between $200\ \mu m$ and $250\ \mu m$ offered high control of deposition by combining a low drift potential and moderate kinetic energy at the top of the canopy. An optimal spray with a Dv_{50} of $225\ \mu m$ and a RSF of 0.6 has been identified for weed treatment (§ 2).

One way to produce a spray with a reduced droplet size distribution is by breaking up multiple round jets in the Rayleigh-Plateau regime. The proposed nozzle is constituted by a pipe ending perpendicularly on a disk. A liquid sheet is generated at the exit of a thin radial opening then the liquid sheet is split in multiple jets by structures located at the disk edge. The dynamics of the flow downstream of a thin radial opening has been modeled analytically. When the gap, H , between the jet nozzle and the plate is reduced the discharging area may be smaller than the inlet area leading to an increase of the main flow velocity downstream of the thin cylindrical opening. This increase of velocity can be related to the relative gap of the nozzle $\frac{H}{R}$. Numerical computations with a volume of fluid method were realized in order to retrieve an analytical model of the flow downstream of the inlet opening (§ 5).

Using the latter model, a theoretical nozzle design has been established in order to produce a spray with droplets with diameter of $225\ \mu m$ (§ 6). The prototyping of this design couldn't be achieved because of its small dimension. However, the design methodology has been validated on a upscale nozzle model. The spray generated by the upscale nozzle has been characterized using high-speed imaging showing a reduced droplet size distribution.

This last conclusion opens new perspective in term of potential nozzle design. Following the methodology proposed in the chapter 6, a reduced span spray with custom characteristics may be produced in order to fit a specific application. At large scale, 3D printing can easily

produce the prototype. Despite technical issues, the production of smaller droplets may face two main problems. The flow generated flow on the disk could be turbulent which may require adjustment of the analytical model to take into account the turbulence. Then, a large amount of jets would be necessary thus the jets would be less spaced and the design of the edge structures have to be adapted. Channels succeed to split the flow at low speed and with large spacing but it may fails when the space between them decreases. Currently, an experimental research is performed on the effect of structures type and dimension on the downstream flow at the GRASP. This fundamental research explores original ways to separate a liquid sheet into jets. For example, they observe that small pillar on the disk creates a wake. Under specific conditions, the wake turns into a dry area on the plate, splitting the liquid sheet into jets. This research, as probably others, shows that the constraint encounter with the channels may be overcome by using other structures. The work on the nozzle design has to be carry on.

References

- Aghajani, H., Dembele, S., and Wen, J. X. (2014). Analysis of a semi-empirical sprinkler spray model. *Fire Safety Journal*, 64:1–11. cited By 0.
- Al Heidary, M., Douzals, J. P., Sinfort, C., and Vallet, A. (2014). Influence of spray characteristics on potential spray drift of field crop sprayers: A literature review. *Crop Protection*, 63:120–130.
- Attané, P., Girard, F., and Morin, V. (2007). An energy balance approach of the dynamics of drop impact on a solid surface. *Physics of Fluids*, 19(1):012101.
- Azuma, T. and Hoshino, T. (1984a). The radial flow of a thin liquid film: 1st report, laminar-turbulent transition. *Bulletin of JSME*, 27(234):2739–2746.
- Azuma, T. and Hoshino, T. (1984b). The radial flow of a thin liquid film: 2nd report, liquid film thickness. *Bulletin of JSME*, 27(234):2747–2754.
- Azuma, T. and Hoshino, T. (1984c). The radial flow of a thin liquid film: 3rd report, velocity profile. *Bulletin of JSME*, 27(234):2755–2762.
- Babinsky, E. and Sojka, P. E. (2002). Modeling drop size distributions. *Progress in Energy and Combustion Science*, 28(4):303–329.
- Baetens, K., Ho, Q. T., Nuyttens, D., De Schampheleire, M., Melese Endalew, A., Hertog, M. L. A. T. M., Nicolai, B., Ramon, H., and Verboven, P. (2009). A validated 2-D diffusion–advection model for prediction of drift from ground boom sprayers. *Atmospheric Environment*, 43(9):1674–1682.
- Baetens, K., Nuyttens, D., Verboven, P., De Schampheleire, M., Nicolai, B., and Ramon, H. (2007). Predicting drift from field spraying by means of a 3D computational fluid dynamics model. *Computers and Electronics in Agriculture*, 56(2):161–173.
- Bals, E. J. (1970). The principles of and new developments in ultra low volume spraying. *The principles of and new developments in ultra low volume spraying.*, 1:189–193.
- Barati, R., Neyshabouri, S. A. A. S., and Ahmadi, G. (2014). Development of empirical models with high accuracy for estimation of drag coefficient of flow around a smooth sphere: An evolutionary approach. *Powder Technology*, 257:11–19.
- Bonhoeffer, B., Kwade, A., and Juhnke, M. (2017). Impact of formulation properties and process parameters on the dispensing and positioning of drug nanosuspensions using micro-valve technology. *Journal of pharmaceutical sciences*, 106(4):1102–1110.

- Boukhalfa, H., Massinon, M., Belhamra, M., and Lebeau, F. (2014). Contribution of spray droplet pinning fragmentation to canopy retention. *Crop Protection*, 56:91–97.
- Butler Ellis, M. C., Alanis, R., Lane, A. G., Tuck, C. R., Nuyttens, D., and van de Zande, J. C. (2017). Wind tunnel measurements and model predictions for estimating spray drift reduction under field conditions. *Biosystems Engineering*, 154:25–34.
- Butler Ellis, M. C. and Miller, P. C. H. (2010). The Silsoe Spray Drift Model: A model of spray drift for the assessment of non-target exposures to pesticides. *Biosystems Engineering*, 107(3):169–177.
- Butler Ellis, M. C., Tuck, C. R., and Miller, P. C. H. (1997). The effect of some adjuvants on sprays produced by agricultural flat fan nozzles. *Crop Protection*, 16(1):41 – 50.
- Butler Ellis, M. C., Tuck, C. R., and Miller, P. C. H. (2001). How surface tension of surfactant solutions influences the characteristics of sprays produced by hydraulic nozzles used for pesticide application. *Colloids and Surfaces A: Physicochemical and Engineering Aspects*, 180(3):267 – 276.
- Canny, J. (1986). A computational approach to edge detection. *IEEE Transactions on Pattern Analysis and Machine Intelligence*, 8(6):679–698.
- Chu, S. S. (2003). Separated flow in bends of arbitrary turning angles, using the hodograph method and kirchhoff’s free streamline theory. *Journal of Fluids Engineering*, 125(3):438–442.
- Cousin, J., Berlemont, A., Ménard, T., and Grout, S. (2012). Primary breakup simulation of a liquid jet discharged by a low-pressure compound nozzle. *Computers & Fluids*, 63:165–173.
- Damaschke, N., Gouesbet, G., Gréhan, G., Mignon, H., and Tropea, C. (1998). Response of phase Doppler anemometer systems to nonspherical droplets. *Applied Optics*, 37(10):1752–1761.
- De Cock, N., Massinon, M., Mercatoris, B. C. N., and Lebeau, F. (2014). Numerical modelling of mirror nozzle flow. In *Proceedings of American Society of Agricultural and Biological Engineers Annual International Meeting*, pages 3632–3640.
- De Cock, N., Massinon, M., Nuyttens, D., Dekeyser, D., and Lebeau, F. (2016). Measurements of reference ISO nozzles by high-speed imaging. *Crop Protection*, 89:105–115.
- de Ruyter, H., Holterman, H. J., Kempenaar, C., and van de Zande, J. (2003). Influence of adjuvants and formulations on the emission of pesticides to the atmosphere: a literature study for the dutch research programme pesticides and the environment (dwc) theme c-2. Technical report, Plant Research International.
- Deshpande, S. S., Anumolu, L., and Trujillo, M. F. (2012). Evaluating the performance of the two-phase flow solver interFoam. *Computational Science and Discovery*, 5(1).
- Dorr, G. J., Wang, S., Mayo, L. C., McCue, S. W., Forster, W. A., Hanan, J., and He, X. (2015). Impaction of spray droplets on leaves: influence of formulation and leaf character on shatter, bounce and adhesion. *Experiments in Fluids*, 56(7):143.

- Dumouchel, C. (2008). On the experimental investigation on primary atomization of liquid streams. *Experiments in Fluids*, 45(3):371–422.
- Fard, M. P., Levesque, D., Morrison, S., and Ashgriz, N. (2007). Characterization of splash-plate atomizers using numerical simulations. *Atomization and Sprays*, 17(4).
- Forster, W. A., Mercer, G. N., and Schou, W. C. (2010). Process-driven models for spray droplet shatter, adhesion or bounce. In *Proceedings of the 9th International Symposium on Adjuvants for Agrochemicals*, volume 16, page 20.
- Fritz, B. K., Hoffmann, W. C., Czaczyk, Z., Bagley, W., Kruger, G., and Henry, R. (2012). Measurement and classification methods using the ASAE S572.1 reference nozzles. *Journal of Plant Protection Research*, 52(4):447–457.
- Gilbert, A. J. and Bell, G. J. (1988). Evaluation of the drift hazards arising from pesticide spray application. *Aspects of Applied Biology*.
- Gordillo, J. M., Lhuissier, H., and Villermaux, E. (2014). On the cusps bordering liquid sheets. *Journal of Fluid Mechanics*, 754:R1.
- Guella, S., Alexandrova, S., and Saboni, A. (2008). Evaporation d'une gouttelette en chute libre dans l'air. *International Journal of Thermal Sciences*, 47(7):886–898.
- Gunn, R. and Kinzer, G. D. (1949). The terminal velocity of fall for water droplets in stagnant air. *Journal of Meteorology*, 6(4):243–248.
- Hewitt, A. (2005). International standards for drift reduction technology studies. Technical report, OECD Workshop.
- Hewitt, A. J., Valcore, D. L., Teske, M. E., and Schick, R. J. (1998). Drop size classifications for agricultural sprays. In *Proceedings of the 11th Annual conference on liquid atomization and spray systems, May 1998, Sacramento, CA, USA*.
- Hilz, E. and Vermeer, A. W. P. (2013). Spray drift review: The extent to which a formulation can contribute to spray drift reduction. *Crop Protection*, 44:75–83.
- Hobson, P., Miller, P., Walklate, P., Tuck, C., and Western, N. (1993). Spray drift from hydraulic spray nozzles: the use of a computer simulation model to examine factors influencing drift. *Journal of Agricultural Engineering Research*, 54(4):293–305.
- Holloway, P. J., Butler Ellis, M. C., Webb, D. A., Western, N. M., Tuck, C. R., Hayes, A. L., and Miller, P. C. H. (2000). Effects of some agricultural tank-mix adjuvants on the deposition efficiency of aqueous sprays on foliage. *Crop Protection*, 19(1):27 – 37.
- Holterman, H. (2003). Kinetics and evaporation of water drops in air.
- Holterman, H. J., van de Zande, J. C., Porskamp, H. A. J., and Huijsmans, J. F. M. (1997). Modelling spray drift from boom sprayers. *Computers and Electronics in Agriculture*, 19(1):1–22.
- Hosain, M. L., Fdhila, R. B., and Daneryd, A. (2015). Heat transfer by liquid jets impinging on a hot flat surface. *Applied Energy*.

- Hou, Q., Kruisbrink, A. C. H., Pearce, F. R., Tijsseling, A. S., and Yue, T. (2014). Smoothed particle hydrodynamics simulations of flow separation at bends. *Computers & Fluids*, 90:138–146.
- Ishigai, S., Nakanishi, S., Mizuno, M., and Imamura, T. (1977). Heat transfer of the impinging round water jet in the interference zone of film flow along the wall. *Bulletin of JSME*, 20(139):85–92.
- Jensen, P. K. (2012). Increasing efficacy of graminicides with a forward angled spray. *Crop Protection*, 32:17–23.
- Josserand, C. and Thoroddsen, S. T. (2016). Drop impact on a solid surface. *Annual Review of Fluid Mechanics*, 48:365–391.
- Kang, L., Guo, L., Gu, Z., and Liu, D. (2008). Wind tunnel experimental investigation of sand velocity in aeolian sand transport. *Geomorphology*, 97(3–4):438–450.
- Kashdan, J., Shrimpton, J., and Whybrew, A. (2003). Two-phase flow characterization by automated digital image analysis. part 1: Fundamental principles and calibration of the technique. *Particle & Particle Systems Characterization*, 20(6):387–397.
- Kok, J. F. and Renno, N. O. (2009). A comprehensive numerical model of steady state saltation (COMSALT). *Journal of Geophysical Research: Atmospheres*, 114(D17).
- Kwak, B.-M., Lee, J. E., Ahn, J.-H., and Jeon, T.-H. (2009). Laser diffraction particle sizing by wet dispersion method for spray-dried infant formula. *Journal of Food Engineering*, 92(3):324–330.
- Langmuir, I. and Blodgett, K. B. (1949). A mathematical investigation of water droplet trajectories. technical report no. rl225. , General Electric Schenectady, N.Y.
- Lebeau, F. (2004). Modelling the dynamic distribution of spray deposits. *Biosystems Engineering*, 89(3):255–265.
- Lebeau, F., Verstraete, A., Stainier, C., and Destain, M. F. (2011). RTDrift: A real time model for estimating spray drift from ground applications. *Computers and Electronics in Agriculture*, 77(2):161–174.
- Lecuona, A., Sosa, P. A., Rodríguez, P. A., and Zequeira, R. I. (2000). Volumetric characterization of dispersed two-phase flows by digital image analysis. *Measurement Science and Technology*, 11(8):1152–1161.
- Lefebvre, A. (1988). *Atomization and Sprays*. Taylor & Francis.
- Li, T., Nishida, K., and Hiroyasu, H. (2011). Droplet size distribution and evaporation characteristics of fuel spray by a swirl type atomizer. *Fuel*, 90(7):2367–2376.
- Lichtarowicz, A. and Markland, E. (1963). Calculation of potential flow with separation in a right-angled elbow with unequal branches. *Journal of Fluid Mechanics*, 17:596–606.
- Liu, X., Doub, W. H., and Guo, C. (2010). Evaluation of droplet velocity and size from nasal spray devices using phase Doppler anemometry (PDA). *International Journal of Pharmaceutics*, 388(1–2):82–87.

- Liu, X., Lienhard, J. H., and Lombara, J. S. (1991). Convective heat transfer by impingement of circular liquid jets. *Journal of Heat Transfer*, 113(3):571–582.
- Mankbadi, R. and Zaki, S. (1986). Computations of the contract coefficient of unsymmetrical bends. *AIAA Journal*, 24(8):1285–1289.
- Mao, T., Kuhn, D., and Tran, H. (1997). Spread and rebound of liquid droplets upon impact on flat surfaces. *AIChE Journal*, 43(9):2169–2179.
- Marshall, A. W. and Di Marzo, M. (2004). Modelling aspects of sprinkler spray dynamics in fires. *Process Safety and Environmental Protection*, 82(2):97–104.
- Massinon, M., Boukhalfa, H., and Lebeau, F. (2014). The effect of surface orientation on spray retention. *Precision Agriculture*, 15(3):241–254.
- Massinon, M., De Cock, N., Forster, W. A., Nairn, J. J., McCue, S. W., Zabkiewicz, J. A., and Lebeau, F. (2017). Spray droplet impaction outcomes for different plant species and spray formulations. *Crop Protection*, 99:65–75.
- Massinon, M., De Cock, N., Ouled Taleb Salah, S., and Lebeau, F. (2016). Reduced span spray—part 1: Retention. *Aspect of Applied Biology, International Advances in Pesticide Application*, 132:323–330.
- Massinon, M., Dumont, B., De Cock, N., Salah, S. O. T., and Lebeau, F. (2015). Study of retention variability on an early growth stage herbaceous plant using a 3D virtual spraying model. *Crop Protection*, 78:63–71.
- Massinon, M. and Lebeau, F. (2012). Experimental method for the assessment of agricultural spray retention based on high-speed imaging of drop impact on a synthetic superhydrophobic surface. *Biosystems Engineering*, 112(1):56 – 64.
- Matthews, G. (2008). *Pesticide application methods*. John Wiley & Sons.
- Miller, P. C. H. and Butler Ellis, M. C. (2000). Effects of formulation on spray nozzle performance for applications from ground-based boom sprayers. *Crop Protection*, 19(8–10):609 – 615. {XIVth} International Plant Protection Congress.
- Mokeba, M., Salt, D., Lee, B., and Ford, M. (1997). Simulating the dynamics of spray droplets in the atmosphere using ballistic and random-walk models combined. *Journal of Wind Engineering and Industrial Aerodynamics*, 67:923–933.
- Mundo, C. H. R., Sommerfeld, M., and Tropea, C. (1995). Droplet-wall collisions: experimental studies of the deformation and breakup process. *International Journal of Multiphase Flow*, 21(2):151–173.
- Nuyttens, D., Baetens, K., Schamphelre, M. D., and Sonck, B. (2007a). Effect of nozzle type, size and pressure on spray droplet characteristics. *Biosystems Engineering*, 97(3):333 – 345.
- Nuyttens, D., De Schamphelre, M., Baetens, K., and Sonck, B. (2007b). The influence of operator-controlled variables on spray drift from field crop sprayers. *Transactions of the ASABE*, 50(4):1129–1140.

- Oerke, E.-C. (2006). Crop losses to pests. *The Journal of Agricultural Science*, 144(1):31–43.
- Panofsky, H. A., Tennekes, H., Lenschow, D. b. H., and Wyngaard, J. C. (1977). The characteristics of turbulent velocity components in the surface layer under convective conditions. *Boundary-Layer Meteorology*, 11(3):355–361.
- Qi, L., Miller, P. C. H., and Fu, Z. (2008). The classification of the drift risk of sprays produced by spinning discs based on wind tunnel measurements. *Biosystems Engineering*, 100(1):38–43.
- Raupach, M. R., Briggs, P. R., Ford, P. W., Leys, J. F., Muschal, M., Cooper, B., and Edge, V. E. (2001). Endosulfan transport. *Journal of Environmental Quality*, 30(3):714–728.
- Rayleigh, L. (1878). On the instability of jets. *Proceedings of the London Mathematical Society*, 1(1):4–13.
- Reichenberger, S., Bach, M., Skitschak, A., and Frede, H.-G. (2007). Mitigation strategies to reduce pesticide inputs into ground- and surface water and their effectiveness; a review. *Science of The Total Environment*, 384(1–3):1 – 35.
- Rein, M. (1993). Phenomena of liquid drop impact on solid and liquid surfaces. *Fluid Dynamics Research*, 12(2):61–93.
- Rosin, P. and Rammler, E. (1933). The laws governing the fineness of powdered coal. *Journal of the Institute of Fuel*, 7:29–36.
- Saboni, A., Alexandrova, S., and Gourdon, C. (2004). Détermination de la traînée engendrée par une sphère fluide en translation. *Chemical Engineering Journal*, 98(1):175–182.
- Sawford, B. L. and Guest, F. M. (1991). Lagrangian statistical simulation of the turbulent motion of heavy particles. *Boundary-Layer Meteorology*, 54(1):147–166.
- Sirignano, W. A. and Mehring, C. (2000). Review of theory of distortion and disintegration of liquid streams. *Progress in Energy and Combustion Science*, 26(4):609–655.
- Snyder, H. E., Senser, D. W., Lefebvre, A. H., and Coutinho, R. S. (1989). Drop size measurements in electrostatic paint sprays. *Industry Applications, IEEE Transactions on*, 25(4):720–727.
- Southcombe, E. S. E., Miller, P. C. H., Ganzelmeier, H., van de Zande, J. C., Miralles, A., and Hewitt, A. J. (1998). The International (BCPC) spray classification system including a drift potential factor. In *Proceedings of the Brighton Crop Protection Conference-Weeds*.
- Spillman, J. J. (1984). Spray impaction, retention and adhesion: an introduction to basic characteristics. *Pest Management Science*, 15(2):97–106.
- Stainier, C., Destain, M. F., Schiffers, B., and Lebeau, F. (2006). Droplet size spectra and drift effect of two phenmedipham formulations and four adjuvants mixtures. *Crop Protection*, 25(12):1238–1243.
- Stephenson, G. R., Ferris, I. G., Holland, P. T., and Nordberg, M. (2006). Glossary of terms relating to pesticides (iupac recommendations 2006). *Pure and Applied Chemistry*, 78(11):2075–2154.

- Taylor, W. A., Womac, A. R., Miller, P. C. H., and Taylor, B. P. (2004). An attempt to relate drop size to drift risk. In *Proceedings of the International Conference on Pesticide Application for Drift Management*, pages 210–223. Citeseer.
- Teske, M. E., Bird, S. L., Esterley, D. M., Curbishley, T. B., Ray, S. L., and Perry, S. G. (2002). Agdrift : A model for estimating near-field spray drift from aerial applications. *Environmental Toxicology and Chemistry*, 21(3):659–671.
- Walklate, P. J. (1987). A random-walk model for dispersion of heavy particles in turbulent air flow. *Boundary-Layer Meteorology*, 39(1):175–190.
- Wang, Y., Miller, D. R., Anderson, D. E., and McManus, M. L. (1995). A Lagrangian stochastic model for aerial spray transport above an oak forest. *Agricultural and Forest Meteorology*, 76(3–4):277–291.
- Watson, E. J. (1964). The radial spread of a liquid jet over a horizontal plane. *Journal of Fluid Mechanics*, 20:481–499.
- Weiner, K. L. and Parkin, C. S. (1993). The use of computational fluid dynamic code for modelling spray from a mistblower. *Journal of Agricultural Engineering Research*, 55(4):313–324.
- Widmann, J. F. (2001). Phase Doppler interferometry measurements in water sprays produced by residential fire sprinklers. *Fire Safety Journal*, 36(6):545–567.
- Wilson, J. D. and Sawford, B. L. (1996). Review of Lagrangian stochastic models for trajectories in the turbulent atmosphere. *Boundary-Layer Meteorology*, 78(1):191–210.
- Womac, A. R. (2000). Quality control of standardized reference spray nozzles. *Transactions of the ASAE*, 43(1):47–56.
- Wu, D., Guillemain, D., and Marshall, A. W. (2007). A modeling basis for predicting the initial sprinkler spray. *Fire Safety journal*, 42(4):283–294.
- Yarin, A. L. (2006). Drop impact dynamics: splashing, spreading, receding, bouncing. . . . *Annual Review of Fluid Mechanics*, 38:159–192.
- Zabkiewicz, J. A. (2007). Spray formulation efficacy - holistic and futuristic perspectives. *Crop Protection*, 26(3):312–319.
- Zhou, X., D’Aniello, S. P., and Yu, H.-Z. (2012). Spray characterization measurements of a pendent fire sprinkler. *Fire Safety Journal*, 54:36–48.

